UNIVERSITY OF COPENHAGEN

Master's thesis

by Henriette Wase Hansen

Crystal growth of $La_{2-x}Sr_xCuO_4$ and spin fluctuations in superoxygenated $La_2CuO_{4+\delta}$

X-ray and Neutron Science, Niels Bohr Institute, University of Copenhagen

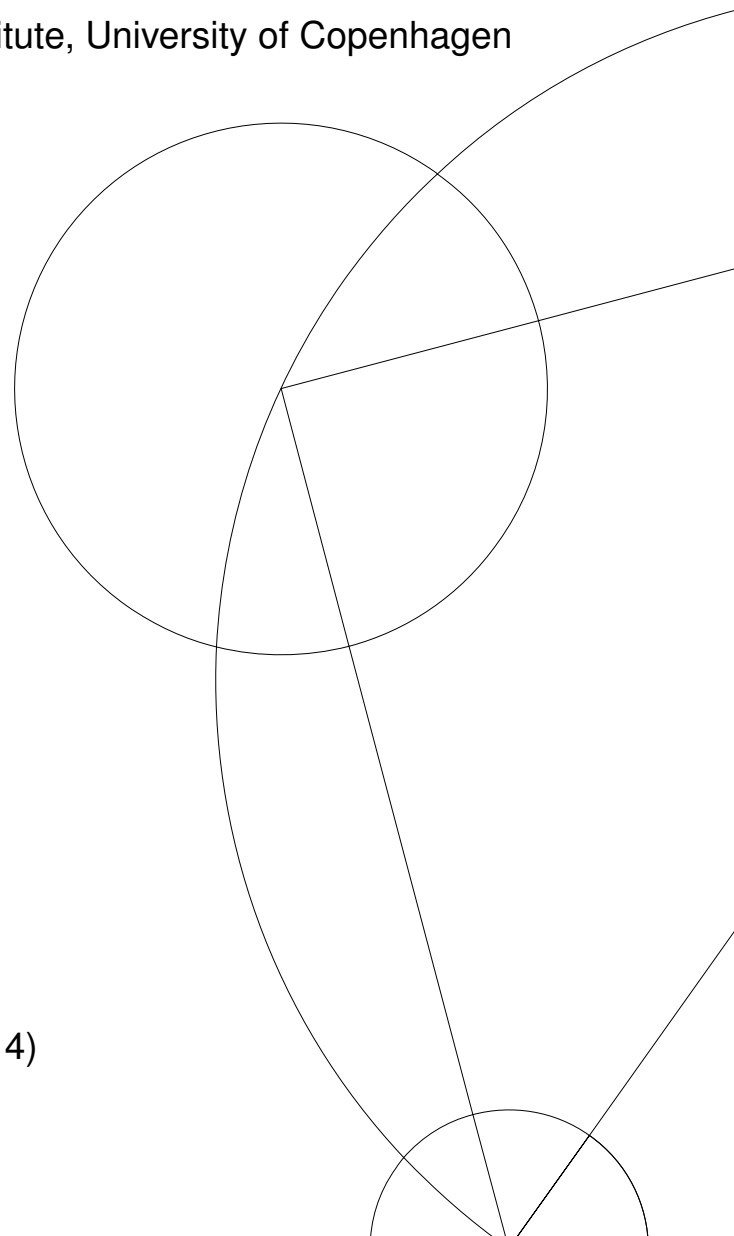

Supervisors: Kim Lefmann and Linda Udby

Submitted 1 June 2014 (Revised 8 July 2014)

Abstract

Crystals of $La_{2-x}Sr_xCuO_4$ were grown for $x = 0.04, 0.05, 0.06, 0.07$, which by preliminary studying with x-ray Laue back-scattering look to be single crystals. Low energy spin fluctuations in a single crystal, superoxygenated $La_2CuO_{4+\delta}$ sample were studied with neutron scattering in the normal and superconducting state. There was not observed an actual spin gap in $La_2CuO_{4+\delta}$ in the superconducting phase as that observed for optimally doped $La_{2-x}Sr_xCuO_4$, $x \approx 0.16$. Instead an anisotropy gap was observed similar to that found in the antiferromagnetic insulator, La_2CuO_4, and in the superconducting $La_{2-x}Sr_xCuO_4$, $x = 0.12$, with a strong magnetic phase.

Preface

The experiment that was originally intended as part of this thesis was the study of in-field low energy spin fluctuation of $La_2CuO_{4+\delta}$. As will be described in Section 3.4, the field-induced effects and the closing of the spin gap in $La_{2-x}Sr_xCuO_4$ (Sec. 3.5) are very interesting areas that could very well prove to be interesting for $La_2CuO_{4+\delta}$ as well. This experiment should have been conducted at FLEXX at Helmholz-Zentrum Berlin in November 2013. Unfortunately, this experiment was postponed at first to January-February 2014, and then again in January 2014, where the experiment was postponed for an unknown amount of time. This did not allow me to participate in actual neutron scattering measurements. However, as part of the preparations for the experiment in November and again in January, I was involved in alignment and co-alignment of the crystals using Laue back-scattering and neutrons and sample holder design. However, only the information relevant for the experiments on low energy spin fluctuations in $La_2CuO_{4+\delta}$ performed at ILL in May and July 2013 is included in this thesis. My role has been to analyze the data from those two experiments.

Acknowledgements

I thank my supervisor Kim Lefmann for teaching me about neutron scattering and helping me find my way through the LSCO jungle, and Linda Udby for teaching me about the oxygen-doped materials. I thank Jean-Claude Grievel for help and guidance on LSCO crystal growth at DTU Risø. I thank Pia Jensen and Henrik Jacobsen for letting me in on the LSCO growing project and sharing experiences from and at DTU Risø. I thank Henrik Jacobsen, Pia Jensen, Kim Lefmann and Linda Udby for letting me inherit their data from ILL. I thank Henrik Jacobsen for helping me with data analysis.

Henriette Wase Hansen, 1 June 2014

Contents

Chapter 1

Introduction

The discovery of high-temperature superconductivity almost thirty years ago was immediately considered a promised land. The idea of a room temperature superconductor had great appeal to scientists and the industry, considering the increasing demand for environmentally friendly energy transported to densely populated areas. However, to this date, no one has succeeded in developing such superconductor, and the understanding of the mechanisms of high-temperature superconductivity seems still more complicated.

This thesis will focus on one of the most studied high-temperature superconductors, which is based on the antiferromagnetic insulator La_2CuO_4 (LCO) hole-doped with either strontium, oxygen, or both. Due to the relatively simple lattice structure of these compounds, they are excellent to study in order to come a step closer to understanding the underlying mechanisms responsible for superconductivity in high-temperature superconductors.

Previous studies using neutron scattering have shown that magnetic order and fluctuations exist within the superconducting phase of the strontium doped compound $La_{2-x}Sr_xCuO_4$ (LSCO). The opening of a spin gap in LSCO at the superconducting transition temperature indicates that the magnetic order is connected to superconductivity. Crystal growth of LSCO has been a large part of this thesis in order to prepare for further studies of spin fluctuations in the underdoped region in field and in the co-doped compound $La_{2-x}Sr_xCuO_{4+\delta}$ (LSCO+O). A second part of this thesis, has been the study of spin fluctuations in the oxygen-doped, superoxygenated, compound $La_2CuO_{4+\delta}$ (LCO+O) based on neutron scattering experiments performed at the Intitut Laue-Langevin in Grenoble, France.

But firstly, the work in this thesis will describe superconductivity in general, and properties of LSCO and LCO+O in particular, before moving on to an introduction of the applied experimental techniques. Thereafter, a presentation of the work related to crystal growth of LSCO and the study of low energy spin fluctuations in LCO+O will follow.

Chapter 2

Superconductivity

The term superconductivity was first coined in 1911 by the Dutch physicist H. Kamerlingh Onnes [36]. He won the Nobel prize in 1913 for his low temperature studies which among other things led to the discovery of liquid helium, with which he cooled metals such as mercury, lead, and tin. He found that at a finite critical temperature, T_c, the resistivity dropped to zero creating a state of superconductivity. The field of superconductors has been studied with great interest ever since, leading to the discovery of a range of high-T_c superconductors with T_c up to around 130 K. However, the field of high-temperature superconductors is still one of great mystery and the underlying mechanisms of the superconducting state are not yet fully understood. This chapter is an introduction to superconductivity and a short introduction to the theory behind low-temperature superconductors, the BCS theory.

2.1 Meissner-Oschenfeld effect

Because the resistance vanishes in superconductors below the critical temperature, T_c, the superconductors are perfect conductors with infinite conductivity. This means that the current flow can be finite only for $\mathbf{E} = 0$. However, according to the Maxwell-Faraday equation, then the magnetic field cannot vary with time inside a sample: $\nabla \times \mathbf{E} = -\frac{\partial \mathbf{B}}{\partial t}$.

W. Meissner and R. Ochsenfeld [49] observed in 1933 that when a perfect superconductor is placed in a magnetic field, the field cannot penetrate the sample. This is because the magnetic induction inside a superconductor is zero even in weak applied magnetic fields; this is known as the Meissner-Ochsenfeld effect (Fig. 2.1). Thus, a magnetic field will be expelled from a sample, as the sample is cooled below its critical temperature, T_c, at which the sample transitions from its normal state to the superconducting state.

In the superconducting state, the surface currents induce a field that will exactly cancel the applied field, maintaining a state of zero magnetic field inside the sample; $\mathbf{B} = \mu_0(\mathbf{H} + \mathbf{M}) = 0$, and therefore the magnetization, $\mathbf{M} = -\mathbf{H}$. The magnetic susceptibility of a superconductor is therefore equal to that of a perfect diamagnet, $\chi_m = -1$.

For most superconductors, the Meissner-Ochsenfeld effect is only observed in relatively weak fields, the critical field strength can for some materials be as low as $H_c \approx 10 - 100$ mT [49]. An applied field stronger than the critical field strength, H_c, will destroy the superconducting phase, and the sample will return to its normal, metallic state.

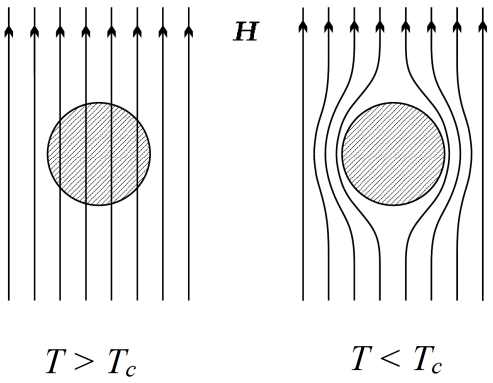

Figure 2.1: Magnetic field lines in a sample in the normal state (left) and the superconducting state (right). Adapted from [49].

2.2 Type-I and type-II superconductors

The transition from superconducting state to normal state when a magnetic field is applied can happen in two ways, leading to two classes of superconductors: type-I and type-II.

In type-1 superconductors, the transition from superconducting state to normal state is dependent on a temperature-dependent critical value of the applied field, $H_c(T)$, i.e., $\mathbf{B}$ is zero inside the sample until $H_c(T)$ is reached at which the entire sample transitions to the normal state and the conductivity is thus finite again.

In type-II superconductors, the magnetic field is not completely expelled at one value of $H_c(T)$; instead there is a lower and an upper critical value of the applied magnetic field. At the lower critical field, $H_{c1}(T)$, the applied magnetic field will start to gradually penetrate the sample, until it is completely penetrated at the upper critical value, $H_{c2}(T)$. Thus, the sample only exhibits the complete Meissner-Oschenfeld effect below $H_{c1}(T)$. When the applied field is in between the upper and lower boundary of the critical field, the sample becomes inhomogeneous and is referred to as being in a mixed state. In the mixed state, flux lines are allowed to pass through the sample in tube-like regions where superconductivity is suppressed, creating alternating regions of superconducting and normal states along the applied magnetic field. The current around the tubes screens the flux and the region in between the tubes of normal state is superconducting. These tubes are called vortices and the total magnetic flux in each vortex is exactly one flux quantum, $\Phi_0 = h/2e$ [21]. The mixed state is therefore also referred to as the vortex state. Type-II superconductors is thought to be more important to technology as H_{c2} can hold values up to an order of 10 T [49].

2.2.1 Penetration depth and coherence length

The brothers Fritz and Heinz London suggested in 1935 that there were other charge carriers responsible for superconductivity besides electrons. They introduced charge, e^*, mass, m_e^*, and electron density, n_s^* for the charge carries in their description of superconductivity. They described a characteristic depth, called the London penetration depth, λ_L, which determines how deep a magnetic field can penetrate into a superconducting sample before it shows the characteristic superconducting behaviour with $\mathbf{H} = 0$. The London penetration depth is

temperature dependent:

$$\lambda_L^2 = \frac{m^*}{n_s^*(e^*)^2\mu_0}, \tag{2.1}$$

where n_s^*, the density of superconducting charge carriers, is the term responsible for the temperature dependence. Beyond this depth, the material behaves as a perfect superconductor and the magnetic field can no longer penetrate the sample. Another characteristic length scale is the coherence length, ξ, which is a measure of the distance from the surface of a superconductor to the bulk superconductor.

In 1950, before the development of a microscopic theory of superconductivity (Sec 2.4), V.L. Ginzburg and L.D. Landau phenomenologically derived a theory based on the fact that the free energy is the most important feature of a system. This theory can be used to describe the macroscopic properties and vortices that are present in type-II superconductors in the mixed state between the normal and superconducting state.

The ratio between the penetration depth and the coherence length is called the Ginzburg-Landau parameter, $\kappa = \frac{\lambda}{\xi}$. The classification into type-I and type-II superconductors originates from κ:

A superconductor with $\kappa < \frac{1}{\sqrt{2}}$ ($\lambda \ll \xi$) is a type-I superconductor, and a superconductor with $\kappa > \frac{1}{\sqrt{2}}$ ($\xi \ll \lambda$) is a type-II superconductor.

2.3 High-temperature superconductors

One extreme group of type-II superconductors for which $\kappa \gg 1$, and which is of particular interest to this study, is the high-temperature superconductors. They were discovered by J.G. Bednorz and K.A. Müller, who were awarded the Nobel prize for their findings in 1987 [32]. They studied the mother compound La_2CuO_4 (LCO), which they doped with barium, substituting trivalent La^{3+} ions with divalent Ba^{2+} ions, producing $La_{2-x}Ba_xCuO_4$ (LBCO) with a critical temperature around 30 K. Measurements indicated strong diamagnetism in the electron-deficient samples, where hole doping dominates. In 1987, they substituted La^{3+} with Sr^{2+}, obtaining $La_{2-x}Sr_xCuO_4$ (LSCO). For LSCO with doping concentration $x = 0.15$, they found the critical temperature to be 37.5 K [32].

This discovery led to the search for superconductors with an even higher critical temperature. Another high-temperature superconductor based on copper oxides, cuprates, was developed by introducing the much smaller Y^{3+} ion and modifying the structure: $YBa_2Cu_3O_{7-\delta}$ (YBCO) and it was found to have a critical temperature of 92 K [58]. This was groundbreaking as the critical temperature was now higher than the boiling point of liquid nitrogen, 77 K, and it was now possible to think of industrial applications of superconductors. The current record for highest critical temperature of a superconducting compound is from 1993 for $HgBa_2Ca_2Cu_3O_{8+\delta}$ with $T_c = 133$ K in ambient pressure and with $T_c = 157$ K under a pressure of 30 GPa [44]. The idea of a room temperature superconductor without the need of cooling seems still more attractive with regard to modern technology. But in order to ever arrive there, there is a need for understanding the underlying mechanisms behind high-temperature superconductors.

LSCO does not have a very high critical temperature, and in that respect is not a real high-temperature superconductor, however, the physics of LSCO classifies as that of a high-temperature superconductor. It is very similar to that of other cuprates that all have a layered structure with copper oxide planes, and the relatively simple lattice structure of LSCO compared with other cuprates, makes LSCO easier to study. By studying LSCO, the

hope is to find a quantum mechanical mechanism behind superconductivity which is relevant for all high-temperature superconductors.

The structure of LSCO is represented in Figure 2.2. In the structure of both the mother compound LCO and LSCO, the oxygen is coordinated octahedrally around the copper ion, making up CuO_2 planes which are thought to be responsible for superconductivity. The La^{3+} ions, and Sr^{2+} when doped LSCO, are situated in planes between the CuO_2 planes. In LSCO, the Sr ions serve as a reservoir of carriers. Because of this layered structure of LSCO and other high-T_c superconductors, the penetration depth and coherence length exhibit strong anisotropy. This will be discussed further in Chapter 3.

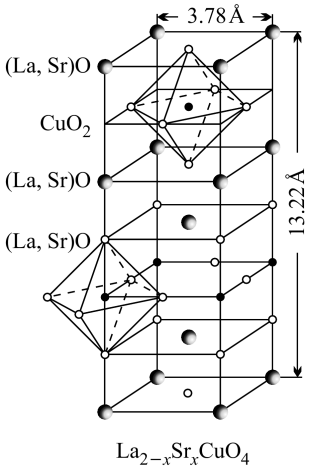

Figure 2.2: A unit cell of the cuprate $La_{2-x}Sr_xCuO_4$. From [49].

2.4 Cooper pairs

In 1957, J. Bardeen, L.N. Cooper, and J.R. Schrieffer published the BCS theory, which was the first microscopic description of superconductivity. Essential for this theory is the formation of singlet Cooper pairs with no external momentum, as first described by L. Cooper in 1956. The Cooper pairs are pairs of electrons with opposite spin and momentum formed by an attractive force caused by phonons in the crystal lattice (Fig. 2.3); these pairs are the charge carriers. Cooper pairs have spin zero and therefore have many of the same characteristics as bosons. At temperatures below T_c, the Cooper pairs are formed and condense into the same quantum state thereby lowering the total energy of the system, and they are free to move around without loosing energy. Knowing that the Cooper pairs are the charge carriers in superconductors, the starred parameters in Section 2.2.1 become $e^* = 2e$, $m^* = 2m_e$, and $n_s^* = n_s/2$; and the penetration depth is then given by $\lambda_L^2 = m_e/(n_s e^2 \mu_0)$ [50].

The BCS theory is a mean-field theory that works well for type-I superconductors because of the large coherence length, in contrast to type-II superconductors. In type-I superconductors, the coherence length can be up to 10^{-6} m at 0 K, which is large compared with atomic distances [50]. The BCS theory predicts the existence of an energy gap in superconductors, defining a forbidden region in the excitation spectrum of the electrons, which is closely related to the energy it takes to break a Cooper pair. In contrast, electrons in the

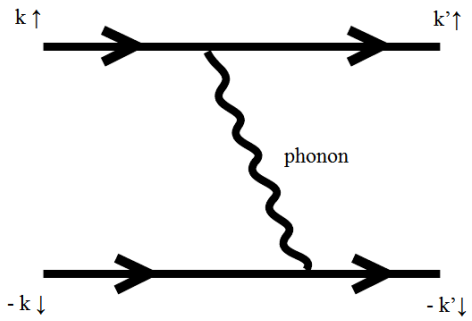

Figure 2.3: Second order Feynman diagram of the formation of a Cooper pair. Time propagates from left to right.

normal state on the Fermi surface can be excited by an arbitrarily small amount of energy. The superconducting energy gap, Δ, disappears at a critical temperature defining the phase transition from superconducting to normal state. The coherence length according to BCS theory is defined as, $\xi^2 = 2\hbar v_f/(\pi\Delta)$, where v_f is the Fermi velocity.

The BCS theory dictates an upper limit in critical temperature of about 30 K [8] where the phonons should no longer be able to create Cooper pairs. The theory is therefore not able to describe the high-temperature superconductors with critical temperatures well above 30 K. There is to this date still not one theory which is able to thoroughly describe high-temperature superconductors and the unusual magnetic properties they exhibit, but it is thought that some other mechanism than the electron-phonon-mediated coupling is responsible.

Chapter 3

LSCO

The high-temperature superconductor (HTSC) $La_{2-x}Sr_xCuO_4$ (LSCO) is, as mentioned in the previous chapter, with its relatively simple crystal lattice structure a good starting point for trying to understand the complex mechanisms behind superconductivity in HTSCs. This chapter contains some of the knowledge on LSCO that has already been established: First about the crystal structure and the phase diagram, then about magnetic order, stripes, and field-induced effects, and finally, about the observation of spin gap.

3.1 Crystal structure

The perovskite crystal structure of the insulating mother compound, the antiferromagnet La_2CuO_4 (LCO), is depicted in Figure 3.1 (left), showing one unit cell in the orthorhombic lattice structure. The unit cell consists of two CuO_2 planes, where the oxygen is coordinated octahedrally around the copper atoms. Planes of lanthanum and oxygen are located in between the copper-oxide planes. The copper-oxide planes and the lanthanum-oxide planes are shifted relative to themselves along the c-axis of the unit cell (Fig. 2.2). Throughout this thesis, the c-axis is defined as the long axis perpendicular to the copper-oxide planes, and the a- and b-axis are defined as the axes in the CuO_2 plane (Fig 3.1, left).

The lattice structure of undoped LCO is orthorhombic at room temperature, but tetragonal at high temperatures. The phase transition from the high-temperature tetragonal (HTT) phase to the low-temperature orthorhombic (LTO) phase for undoped LCO is around a temperature of 530 K. In undoped LCO, the length of the orthorhombic lattice vectors a, b, and c at 10 K is 5.34 Å, 5.42 Å, and 13.10 Å, respectively [37]. In the HTT phase $a = b$. The angle between the lattice vectors is 90° in the orthorhombic phase as well as in the tetragonal phase. The phase transition from the tetragonal to the orthorhombic phase is due to a tilt in the CuO_6 octahedron around the [010] or [100] axis as illustrated in Figure 3.1 (left). The tilt in the CuO_6 octahedron takes place upon cooling due to the difference in thermal expansion of the La-O and the Cu-O bonds [6]. Strontium doping will stabilize the tetragonal phase and decrease the orthorhombic distortion, which will result in a lower transition temperature. Thus, the phase transition temperature changes with doping concentration as illustrated in Figure 3.1 (right). The LCO system is also very sensitive to hole doping with excess oxygen, and the phase diagram therefore looks different for the superoxygenated compounds (Chap. 4).

There are other structural phases for high-temperature superconducting cuprates, but only the HTT and LTO relevant for LSCO are treated in this thesis. The HTT phase is in

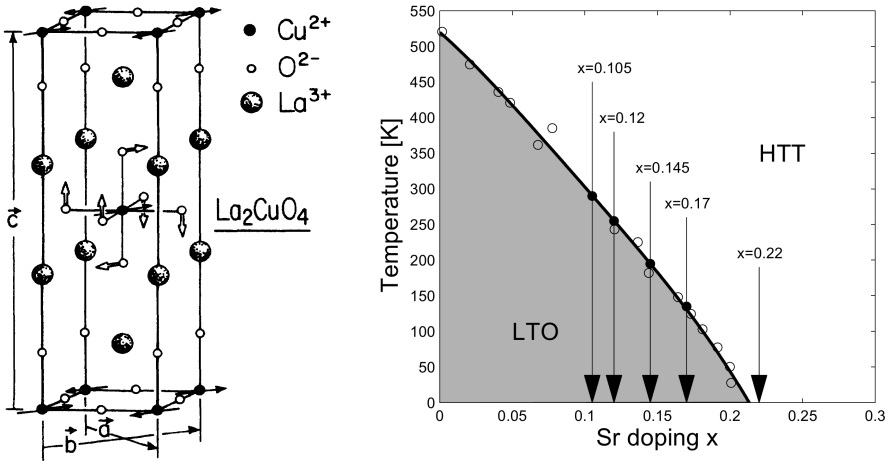

Figure 3.1: Left: LCO lattice structure adapted from Peters et al. [37]. The arrows on the oxygen ions indicate the tilt of the octahedron responsible for the phase transition. Arrows on the copper ions illustrate the antiferromagnetic spin. Right: LSCO phase diagram of the transition temperature between the high-temperature tetragonal (HTT) phase and the low-temperature orthorhombic (LTO) phase for different values of Sr-doping, x. From [9].

space group $I4/mmm$ ($a = b < c$) and the LTO phase is in space group $Bmab$ ($a < b < c$). In the HTT phase, the allowed reflections for h, k, l, are all even or all odd in the orthorhombic notation $Fmmm$. Additionally, for the LTO phase, reflections for h, l even and k odd; or h, l odd and k even are allowed. The space groups are used in fitting powder diffraction data to reflections in Section 6.4.

3.1.1 Twinning

Crystal twinning is a well known phenomena in crystallography and can make analysis of structural signals from single crystal samples studied by neutron or x-ray scattering difficult. Twinning is a slight misorientation or distortion in a crystal lattice which can result in multiple structural signals in scattering experiments. An example of twinning is given in Figure 3.2.

For LSCO, twinning is especially of interest when a single crystal is cooled through the tetragonal phase to the orthorhombic phase, which is often the case when LSCO is either studied or grown. Twinning in LSCO occurs in the (a, b)-plane where the axial oxygen atoms are distorted so that they are either above or below the actual copper-oxide plane. At the phase transition from HTT to LTO, two different tilt axes for the CuO_6 octahedron can occur, resulting in a twin boundary formed at the (110) or (1-10) plane [6]. The orthorhombic distortion causes a rotation around either the [010] axis so that $a > b$ or around the [100] axis so that $b > a$ (Fig. 3.2).

Each twin boundary can distort the CuO_2 plane either way, resulting in a total of four different twin orientations (Fig. 3.2), i.e. in the LTO phase up to four reflections can be seen around the allowed reflections, causing multi-peak or peak-splitting in Bragg reflections, or peak broadening if the instrument resolution does not allow to see full peak splitting.

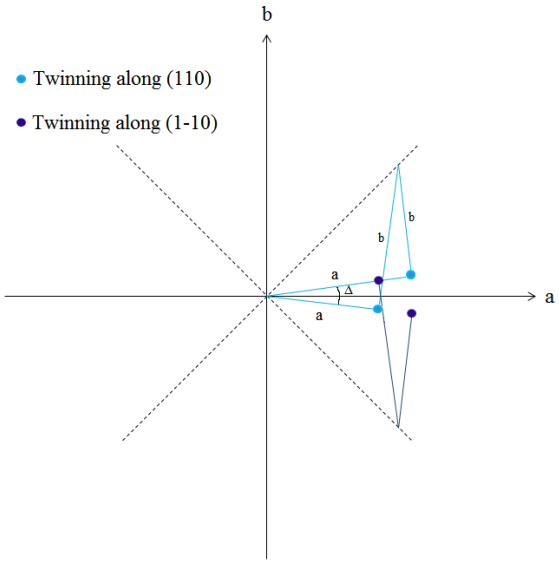

Figure 3.2: A schematic drawing of the four possible twinning peaks surrounding the position of a peak in the tetragonal lattice structure of LSCO.

The tilting angle is given by [6]:

$$\Delta = 90^\circ - 2\arctan\left(\frac{b}{a}\right). \tag{3.1}$$

Twin domains can be seen in neutron scattering experiments as a superposition of intensity of Bragg reflections if the instrument resolution allows for it. Strain in the crystal lattice can affect the size of signals from twinning.

3.2 Phase diagram

Lanthanum and oxygen in LSCO are in oxidation state $+3$ and -2, respectively, and copper must therefore be in its Cu^{2+} state. In the ground state, copper has electronic configuration $[Ar]3d^{10}4s^1$ and thus, by removing two electrons, Cu^{2+} has electron configuration: $[Ar]3d^9$ with an almost full d-shell. The electronic configuration of copper is due to orbital quenching so that $L = 0$, instead of obeying Hund's second rule with $L = 2$ [5]. The copper ion therefore has spin $\frac{1}{2}$, which should make LCO a conductor with one hole in the d-band per Cu atom. However, it requires a lot of energy to add an extra electron to the copper atom due to the repulsion from the other electrons in the valence shell. This results in one loosely bound electron on practically every Cu site, making the crystal a poor conductor. This is also known as a Mott insulator.

The spins in the CuO_2 planes in LCO are antiferromagnetically ordered below the Néel temperature, $T_N \approx 300$ K, over distances greater than 200 Å. Hence, the undoped LCO is both a Mott insulator as well as an antiferromagnet [8, 38]. The spins are aligned in the (a, b)-plane as illustrated in Figure 3.1(left). The spins are slightly canted out of the (a, b)-plane by an angle of $\sim 0.17^\circ$ [37].

A generic phase diagram representative for all cuprate high-temperature superconductors is presented in Figure 3.3 and shows how the different phases depend on doping concentration. When LCO is doped with strontium, more holes are created in the lattice as Sr^{2+} ions substitute La^{3+}, creating Cu^{3+} ions. The antiferromagnetic order breaks down at a doping value about $x = 0.02$. The holes on the strontium sites will attract the loosely bound electrons from copper sites, and those copper sites will then be able to transport electrons, turning the compound into a conductor, and in a specific range of x, a superconductor. The Jahn-Teller distortion of the octahedron around the copper ions means that the holes in the d-shell will be in the hole state with the lowest energy, the $3d_{x^2-y^2}$ state.

Hole doping the mother compound LCO with excess oxygen will have a similar effect on the copper ions as doping with strontium, but the phase diagram looks quite differently. This is discussed in Chapter 4.

When the doping concentration reaches a certain level, LSCO becomes superconducting in a specific temperature range (Fig. 3.3), as doping gradually destroys the long-range antiferromagnetic order. LSCO is superconducting in the range from $0.06 \leq x \leq 0.28$ [18], where superconductivity breaks down, and the system becomes a Fermi liquid. LSCO is optimally doped for $x = 0.15$, where it reaches a maximum critical temperature, $T_c = 37.5$ K [32].

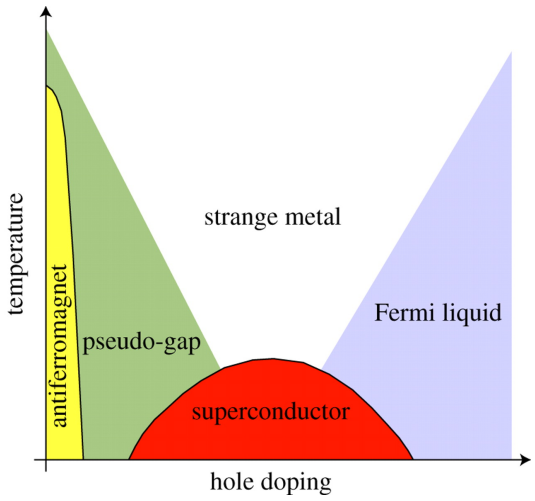

Figure 3.3: A generic, heuristic phase diagram showing phase transition temperatures as a function of hole doping, x, in cuprate high-temperature superconductors. From Philips [38].

The strange metal region in the phase diagram (Fig. 3.3) refers to a phase in which the resistivity scales linearly with temperature, unlike the quadratic dependence in normal Fermi liquids [38].

Below the critical temperature in conventional superconductors, the energy required to break up a Cooper pair creates an energy gap in the electron density of states, which vanishes above the critical temperature. In unconventional superconductors such as the cuprates, in a certain doping and temperature range, the size of the energy gap depends on the orientation of the crystal lattice and it does not disappear when a sample is heated above the critical temperature [38]. This is referred to as the pseudo-gap region in the phase diagram (Fig. 3.3). Different suggested reasons for this phenomenon include phase coherence, a quantum critical point, spin fluctuations, and stripes where the antiferromagnetic and superconducting phase seem to coexist [8].

3.3 Magnetic order and stripes

The magnetic properties have proven to be a very complex area in cuprates. Antiferromagnetic order from a tetragonal lattice structure is characterized by the wave vector $(\frac{1}{2}, \frac{1}{2})$ in tetragonal notation using reciprocal lattice units $\frac{2\pi}{a}$, where a is a lattice constant of the structural unit cell. In orthorhombic notation in two dimensions, this signal is at $(h, k) = (1, 0)$ in reciprocal lattice units, where a is now the orthorhombic lattice constant. Structural peaks from LCO in orthorhombic notation appear at e.g. $(\pm 2, 0)$ and $(0, \pm 2)$.

In LSCO, antiferromagnetic order breaks down when the doping concentration is above $x = 0.02$ and reaches the superconducting state at $x \approx 0.06$. It has been proven that a magnetic short-ranged spin-glass phase in the region $0.02 < x < 0.05$ continues into the superconducting region and thus, coexists with superconductivity in the underdoped region [18], i.e. up until $x = 0.15$ as can be seen in Figure 3.4. In this figure, the data points represent the temperature of magnetic spin freezing, T_g. At $x = 0.12$, superconductivity seems to compete with magnetic order: an increase in the magnetic freezing temperature, T_g, and a small decrease in the critical temperature, T_c. This is known as the $\frac{1}{8}$ anomaly. The magnetic transition temperature, T_g, was obtained with muon spin rotation (μSR) and nuclear magnetic resonance (NMR) [18].

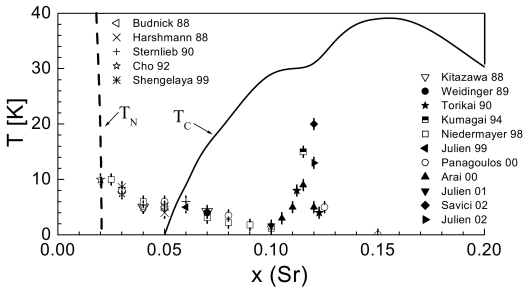

Figure 3.4: Magnetic phase diagram of LSCO from Julien [18]. The temperature of magnetic freezing, T_g, is shown as data points along with the phase transition temperatures, T_c, and the Néel temperature, T_N. The data was obtained with μSR and NMR.

This new type of order is called incommensurate antiferromagnetic (IC AFM) order because the characteristic wave vector of these signals differ from that of the commensurate order and cannot be characterized by integer values of h and k.

The IC AFM order in two dimensions in orthorhombic notation are found at positions $(\pm 1 \pm \delta, \pm \delta)$ and $(\pm \delta, \pm 1 \pm \delta)$, where δ is the offset of the signal compared to the commensurate AFM signal. For doping concentrations $0.06 \leq x \leq 0.12$ in the superconducting region, $\delta \approx x$ and seems to saturate at $\delta \approx \frac{1}{8}$ for $x > 0.12$ [59], this is known as the Yamada relation. Another curious aspect is that below the superconducting region, $x < 0.055$, where $\delta \approx x$ has also proved to hold, the shift in IC magnetic peak positions is diagonal in tetragonal notation, whereas a parallel shift compared to the commensurate AFM peak position becomes dominating as superconductivity sets in [15]. IC magnetic signals have been observed by neutron scattering experiments.

Stripes have been suggested as an explanation of the IC magnetic signals. Stripes are correlations between spin and holes in the copper atoms in the CuO_2 planes. For LSCO this means that the spin of the copper atoms are correlated antiferromagnetically over large distances in the (a, b)-plane with charge carrier holes placed at every fourth copper site (Fig. 3.5). This kind of magnetic phase order creates rivers of charge flow along the stripes,

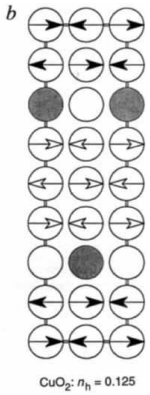

Figure 3.5: Hypothesized stripe model for the CuO_2-planes in LSCO, $x = 0.125$ from [54]. Oxygen atoms are omitted in this figure. Arrows indicate spin on copper atoms. The filled and unfilled circles represent holes.

where the charge flow rivers are domain walls acting as antiphase boundaries for the spins. The periodicity of magnetic stripes is therefore eight times that of the structural unit cell and would give rise to a signal at $\delta \approx \frac{1}{8}$. The stripe model also suggests charged stripes with a periodicity four times that of the structural unit cell, which should give a signal at $\varepsilon \approx 2\delta$.

Magnetic stripes were first observed by Tranquada et al. [54] for $La_{2-x}Ba_xCuO_4$ (LBCO) and $La_{1.6-x}Nd_{0.4}Sr_xCuO_4$ (LNSCO) with $x = 0.12$. They found that in the spin correlated system, the characteristic wave vectors for LNSCO were $(\frac{1}{2} \pm \delta, \frac{1}{2} \pm \delta)$, and $(-\frac{1}{2} \pm \delta, \frac{1}{2} \pm \delta)$, where $\delta = \frac{1}{8}$ as expected for a system with magnetic order with periodicity eight as suggested in Figure 3.5.

Zimmermann et al. [61] confirmed charged stripes for LNSCO, $x = 0.12$, by observing static incommensurate charge order with hard x-rays. The suppression of critical temperature in LNSCO and LBCO is also much more severe than in LSCO. This difference is believed to be due to the low temperature tetragonal phase that both LBCO and LNSCO are in, as opposed to the low temperature orthorhombic phase of LSCO. As this phase does not exist for pure LSCO, but does exist for LBCO and LNSCO, this offers an explanation as to why charged stripes have not been directly observed in LSCO.

In a recently submitted article from spring 2014, Christensen et al. [12] prove the existence of bulk charge stripe order in LSCO below $T = 85$ K around twin boundaries, where twinning causes local low temperature tetragonal structure, also studied with high-energy x-rays. The IC AFM order and reason findings of charge stripe order for twinned LSCO, suggest that the magnetic structure of LSCO is similar to that of LBCO and LNSCO.

3.4 Field-induced effects

Lake et al. [24, 26] have proven that by applying a magnetic field in neutron scattering experiments to a high-temperature superconductor, the antiferromagnetic order is induced for LSCO. Application of a field allows for studying the mixed vortex state in which the superconducting state is present along with vortices of normal state. Lake et al. [25] showed that the signal is short-ranged three-dimensional (Fig. 3.6).

The magnetic signal from neutron scattering is enhanced by an external magnetic field when it is applied along the c-axis of a single crystal. When no field is applied, entropy

and defects in the copper-oxide planes favour random stacking as shown in Figure 3.6(a), whereas in Figure 3.6(b), the field-induced effect can be seen. By applying a magnetic field along the c-axis, a superconducting Cooper pair of electrons is allowed to tunnel between two superconducting surfaces through an insulating layer, which in this case is the distance between the copper-oxide sheets. This is known as the Josephson coupling [21]. The coherence length in the (a, b)-plane in LSCO is $\xi_{ab}(0) = 31 - 33$ Å and is more or less independent of x, whereas the coherence length along the c-axis changes with x: $\xi_c(0) = 0.055 - 3$ Å in the range from $x = 0.08 - 0.3$ [51], although some uncertainty is related to these numbers. Independent of doping concentration, ξ_c is much less than the inter-planar distance, $d \approx \frac{13}{2}$ Å, between the superconducting planes. The short-ranged coupling between the sheets will stack the vortices when a field is applied and thereby lower the magnetic energy by producing antiferromagnetically correlated spins across copper-oxide planes.

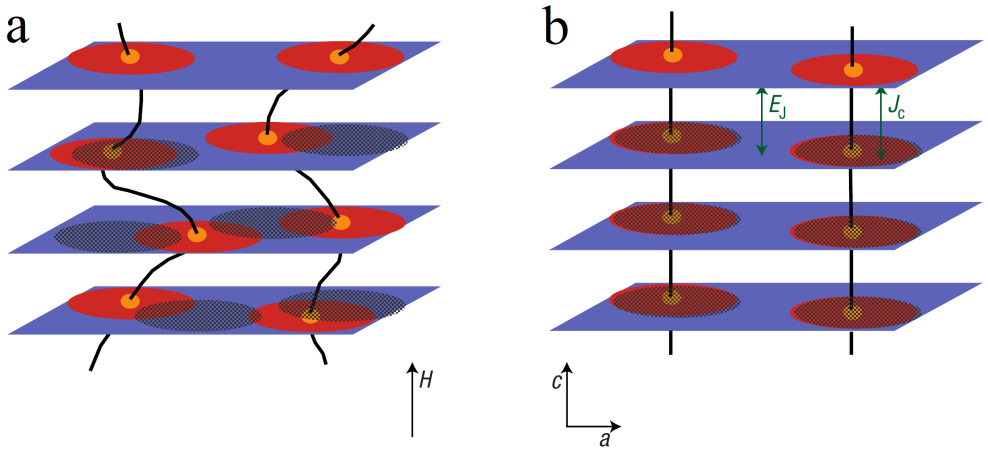

Figure 3.6: Figure from Lake et al. [25]. The sheets represent the CuO_2 sheets in real space, the red circles represent the magnetic vortices and the shaded areas represent the degree of which the vortices are stacked along the c-axis. (a) Zero field, (b) in-field.

An external applied field induces the magnetic signal in vortices in LSCO and therefore also the antiferromagnetic order; it is therefore an excellent method of studying spin phenomena in the vortex state.

3.5 Spin gap

Spin gaps and the suppression of spin fluctuations in the superconducting state at low energies has been studied widely, e.g. [1, 10, 22, 24, 42], as this is believed to play an important role in understanding the underlying mechanisms of high-temperature superconductivity because the spin gaps for LSCO are opened at the transition temperature from superconducting to normal state.

Aeppli et al. [1] reported in 1997 that, as expected in the normal state, no spin gap or pseudo-gap was observed in the normal state above the critical temperature, T_c, of a $x = 0.14$ sample, and that the magnetic response increased with decreasing temperature towards T_c. In 2001, Lake et al. [24] studied an optimally doped sample, $x = 0.163$, and reported a spin gap in the superconducting state at 6 meV, which closes in the normal state

(Fig. 3.7). They applied a 7.5 T field perpendicular to the CuO_2 planes, at a value close to the transition between a true superconducting state with zero resistivity and a mixed state. In the superconducting state, they found that the signal was suppressed at the value of the spin gap in zero field, but increased for lower energies (Fig. 3.7). Lake et al. suggested that this indicated that superconductivity is related to the superconducting phase coherence throughout the sample rather than local pairing.

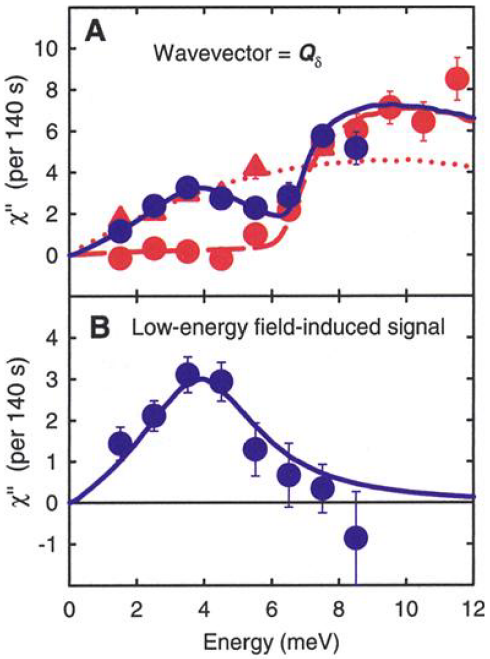

Figure 3.7: Magnetic response as a function of energy transfer for LSCO, $x = 0.163$ from Lake et al. [24]. (A) In the normal state (red triangles), in the superconducting state (red circles), and in superconducting state with applied field (blue circles). (B) The difference between the signal in zero field and applied field is printed in blue.

In 2009, Chang et al. [10] studied a $x = 0.145$ sample. They reported a spin gap of 4 meV in the superconducting state in zero field. They found that by application of a 7 T field perpendicular to the CuO_2 planes, the spin gap collapsed and instead a long-range IC AFM order set in.

Also in 2009, Kofu et al. [22] studied several samples with $x = 0.125, 0.13, 0.135, 0.14$. They found a spin gap for $x = 0.135$ and $x = 0.14$ at 3 meV. For $x = 0.13$ and $x = 0.125$ they did not find an actual gap, but instead a dip in magnetic response around 4 meV. They believed that this observation close to the $\frac{1}{8}$ anomaly was due to a static stripe order causing spin fluctuations below 4 meV. They suggested two distinct magnetic phases; a non-superconducting region with static spin stripes and a superconducting region with a spin gap at 4 meV.

However, a study from 2013 by Rømer et al. [42] suggested that there was only one phase and no energy gap for an $x = 0.12$ sample. Instead they suggested an anisotropy gap, which was in line with observations from canted spins in the AFM, undoped mother compound LCO [37]. This means that there is not an actual spin gap, but instead an anisotropy that partially suppresses the magnetic response until an energy transfer of 1 meV. This is

illustrated in Figure 3.8.

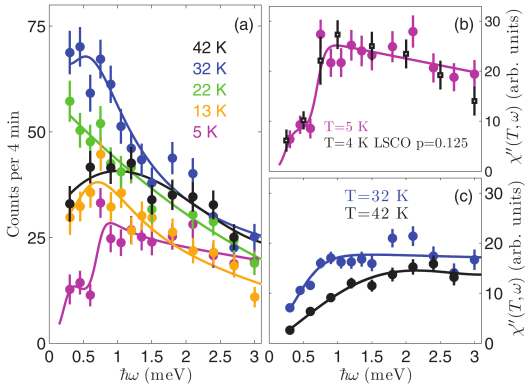

Figure 3.8: Inelastic response and magnetic response as a function of energy transfer for LSCO, $x = 0.12$ from Rømer et al. [42]. (a) Inelastic response at different temperatures. (b) Magnetic response at $T = 5$ K (purple) compared with data from Kofu et al. [22] for their sample of $x = 0.125$ at 4 K (black). (c) Magnetic response for $T = 32$ K and $T = 42$ K. All lines are guides to the eye.

Chapter 4

Superoxygenated LCO+O

In Chapter 3, the effect of doping the mother compound La_2CuO_4 (LCO) with holes by substituting Sr^{2+} ions for La^{3+} ions was investigated and it was seen that in a certain doping range, the new compound LSCO became superconducting below a critical temperature dependent on the doping concentration.

It is possible to obtain the same effect by hole doping with oxygen, not by substitution as for LSCO, but by intercalation of excess oxygen into the La_2CuO_4 lattice structure, and $La_2CuO_{4+\delta}$ (LCO+O) is then obtained. δ is the additional oxygen content also sometimes referred to as y or γ. This means that oxygen atoms occupy interstitial sites in the crystal lattice structure. These structures are said to be superoxygenated. Oxygen atoms will intercalate between two neighbouring layers of La-O in the LCO lattice as illustrated in Figure 4.1. Because of the very high electronegativity of oxygen, oxygen is able to oxidize copper in the same way as strontium, creating Cu^{3+} ions in the crystal lattice as electrons are transferred from the copper ion to the oxygen, forming reduced oxygen ions, and the new compound will, just as in the case of LSCO become superconducting. The critical temperature for LCO+O is $T_c \approx 40$ K.

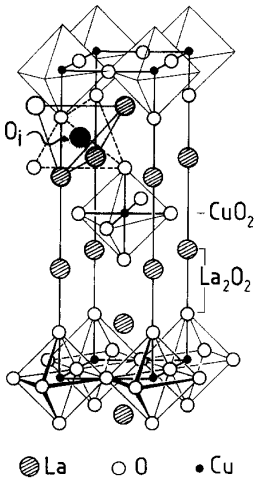

Figure 4.1: The large black dot represents interstitial oxygen entering an idealized tetragonal lattice structure of $La_2CuO_{4+\delta}$. From Grenier et al. [16]

4.1 Electrochemical oxidation of LCO

The actual superoxygenation, or oxygen doping, was initially done by annealing the LCO or LSCO samples at high temperatures (above 500°C) under a few kbar oxygen pressure [39, 45, 46]. A more recent method involves electrochemical oxidation. Example of this method are given in references [11] and [39]. The idea is to intercalate oxygen into a single crystal LCO through slow electrochemical oxidation in aqueous base, where the LCO single crystal is the positive working electrode, and the negative counter electrode is a platinum wire because of its extreme inertness. The platinum wire is wrapped around the crystal. To secure flow of charge, the electrolysis takes place in an aqueous alkaline solution (e.g. 1 M NaOH (aq)). A constant anodic current of 10 μA for several months, up to a year depending on the size of the sample, is required in order to achieve bulk superconductivity in the sample, keeping an electrical potential below 0.6 V to prevent electrolysis of water.

4.2 Determination of oxygen concentration

It is very difficult to control how much oxygen will enter a sample during superoxygenation, but in order to understand the role of oxygen in the superconducting phase and in the electronic structure as such, it is important to determine the accurate stoichiometry of $La_2CuO_{4+\delta}$. There are several ways of determining the oxygen concentration. Unfortunately, most methods require destruction of a part of a sample and it is therefore often not done before very late in the process of studying a single crystal.

Two ways of determining the content of interstitial oxygen are thermogravimetric analysis (TGA) and iodometric titration. Using thermogravimetric analysis, a superoxygenated sample is finely powderized and then slowly heated at for example five degrees per minute in hydrogen reduction atmosphere, allowing the interstitial oxygen to evaporate from the sample and give end products La_2O_3, SrO and copper metal. The interstitial oxygen will start to evaporate at around 180°C. The loss of mass of the sample is recorded as a function of time, thus, it is possible to determine the concentration of excess oxygen, δ. Large uncertainties are associated with TGA as it is difficult to reproduce results.

Using iodometric titration, a sample is dissolved in a liquid and titration or back titration, if the sample is dissolved in acid first, is used to determine the total oxygen concentration in a sample by measuring the oxidation state of copper. A detailed description of iodometric titration of LSCO can be found in Appelman et al. [3]. One of the problems of this method is that oxygen ions can occur in different ionization states with the same charge [45]: O^{2-} and $(O_2)^{2-}$; O^- and $(O_2)^-$. Thus, the yielded oxygen concentration, δ, will depend on what oxidation state of oxygen is assumed to be in the sample and can as a result give a rather large uncertainty on δ.

For a reasonably good estimate of δ, both TGA analysis, which gives an estimate of the excess amount of oxygen atoms, and iodometric titration, which gives an estimate of the number of holes introduced to the crystal lattice, are therefore needed.

4.3 Phase diagram

A phase diagram for LCO+O has been developed by Wells et al. [57], similar to that of LSCO (Fig. 3.3), and is represented in Figure 4.2. A big difference between LSCO and LCO+O is that the oxygen atoms are free to move down to a temperature of around 200 K, whereas strontium ions are immobile. This temperature is much lower than the antiferromagnetic exchange coupling between nearest neighbour Cu spins ($J \approx 1500$ K) and the electronic

bandwidth ($W \approx 2J$) [57]. This means that the excess oxygen in LCO+O, to the extend the system allows, will arrange in a way as to minimize the free energy. The mobility of oxygen gives rise to some very different regions in the phase diagram compared to that of LSCO.

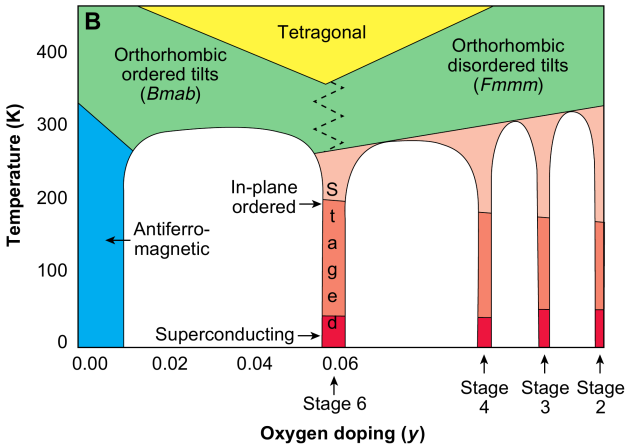

Figure 4.2: Proposed phase diagram for $La_2CuO_{4+\delta}$ by Wells et al. [57]. The different phases are explained in the text.

LCO+O is in the antiferromagnetic region for $\delta \leq 0.01$ with a Néel temperature of $\sim$ 250 K at $\delta = 0.01$ [16] and in the same space group as orthorhombic LSCO, *Bmab*, until the onset of superconductivity. LCO+O is superconducting for $\delta \approx 0.055$ with a critical temperature, $T_c \approx 32$ K, and again around $\delta \approx 0.1$ with $T_c > 40$ K [11, 16, 31, 39], which is higher than the optimally doped LSCO with a maximum $T_c = 37.5$ K. Between the antiferromagnetic and the superconducting phase, $0.01 < \delta < 0.055$, there exists a miscibility gap in which, the oxygen ions phase-separate into oxygen-rich and oxygen-poor regions below $T_{PS} = 290$ K [57]. In the first superconducting region, $\delta \approx 0.06$, staging of the oxygen atoms is believed to take place and a change in the orthorhombic phase [57]. Staging is used to describe the modulation along the *c*-axis caused by intercalated oxygen ions (Fig. 4.3). The intercalated ions will create antiphase domain boundaries between the CuO_2 planes, which causes a change in the direction of the CuO_6 octahedral tilt in a copper oxide plane. This causes a change in space group from orthorhombic *Bmab* to orthorhombic *Fmmm*. The stage number refers to the periodicity of the oxygen-rich layers responsible for the tilt in the CuO_6 octahedron.

Incommensurate antiferromagnetic fluctuations in the range 2-4 meV have been measured in LCO+O by inelastic neutron scattering for $\delta \approx 0.055$ by Wells et al. [57], although they did not measure an actual spin gap.

4.4 LSCO+O

In the co-doped material $La_{2-x}Sr_xCuO_{4+\delta}$ (LSCO+O), the excess oxygen content, δ, raises the superconducting onset temperature to around 40 K as was seen for LCO+O. This effect seems to be irrespective of the strontium content [31]. As for LSCO and LCO+O, magnetic and superconducting phases exist in LSCO+O. Experiments show that the magnetic and the superconducting phases will separate into two distinct phases in LSCO+O, and they

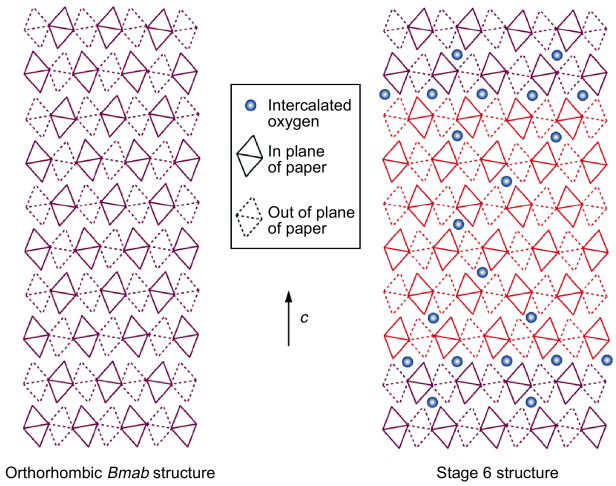

Figure 4.3: Illustration of staging in LCO+O from [57]. Left: Illustration of the tilt in the CuO_6 octahedron for undoped LCO. Right: Schematic of the stage 6 tilt structure in the CuO_6 octahedron in LCO+O, where the difference in shading represents different antiphase tilt domains.

seem to be the only stable phases (Fig. 4.4). This creates a miscibility gap in LSCO+O which is similar to that for LCO+O.

In Figure 4.4, a three-dimensional temperature phase diagram for LCO+O, LSCO and LSCO+O from Mohottala et al. [31] is represented, showing the dependence on the number of holes, n_h, from either Sr (one hole per atom) or O (assumed two holes per atom) and some of the similarities between the compounds. The red regions represent the magnetic ordered states for $n_h = \frac{1}{8}$: the antiferromagnetic region and the $\frac{1}{8}$ anomaly. The superconducting regions are represented with blue, including the optimally doped region, $n_h \approx 0.16$. The dashed regions in the phase diagram represent the miscibility gap in LCO+O and LSCO+O.

The study was carried out using different LSCO crystals and powders with different strontium doping, which were then superoxygenated by electrolysis. An indication of the oxygen content was found by studying the stage of the sample. Some of the samples used: a LCO+O sample in stage 4, a LSCO+O sample with $x = 0.04$ in stage 6, and LSCO+O samples with $x = 0.09$ with no real signs of staging.

Udby et al. [55] showed, using μSR and neutron scattering, that the magnetic stripe order phase will emerge in superoxygenated LSCO+O and phase separate from the superconducting region. The magnetically ordered phase in LSCO+O and LCO+O has the same high T_c above that of optimally doped LSCO and is therefore not suppressed at the $\frac{1}{8}$ anomaly as for LBCO, LNSCO, and to some extend for LSCO. This suggests phase separation rather than phase competition in LSCO+O.

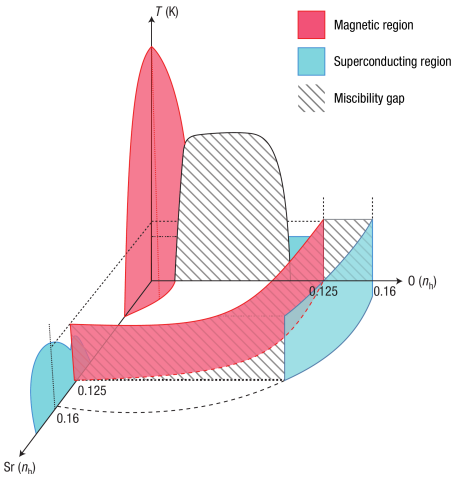

Figure 4.4: Three-dimensional temperature phase diagram of $La_{2-x}Sr_xCuO_{4+y}$ as a function of hole doping with strontium, $Sr(n_h)$, and oxygen, $O(n_h)$. From Mohottala et al. [31].

Chapter 5

Scattering methods

In the work related to this thesis, scattering techniques are important tools for checking sample quality, aligning samples as well as for actually studying samples using structural nuclear or magnetic signals. X-ray scattering has been used in the process of growing LSCO crystals (Chap. 6) in order to check powder sample quality and in order to check that the crystals grown are indeed single crystals, while neutron scattering has been used for studying low energy spin fluctuation in a superoxygenated $La_2CuO_{4+\delta}$ sample (Chap. 7) and for the final co-alignment of four sample pieces. This section will give a brief introduction to x-ray and neutron scattering techniques.

Elastic scattering events are in real space governed by Bragg's law, $\lambda = 2d\sin\theta$, and in reciprocal space by the Laue condition, $\mathbf{Q} = \mathbf{G}_{hkl}$. In Bragg's law, λ is the wavelength of the incoming wave, d is the spacing between planes of atoms, and θ is the scattering angle. The reciprocal lattice vector, $\mathbf{G}_{hkl}$, denoted by the Miller indices (h,k,l), is perpendicular to the plane spanned by (h,k,l) and corresponds to some plane in the unit cell. $\mathbf{G}_{hkl}$ has a magnitude of $2\pi/d_{hkl}$, where d_{hkl} is the lattice spacing of the (h,k,l) planes. The equivalence between these two laws is illustrated in Figure 5.1. From Fourier transform it is given that objects that are extended in real space are confined in reciprocal space. Reciprocal space is therefore an excellent way of describing scattering events.

5.1 X-ray scattering

X-rays are electromagnetic waves with wavelengths in the region of one Ångström, 1 Å= 10^{-10} m, without mass and magnetic moment. According to Maxwell's equations, the direction of propagation of an x-ray beam is that perpendicular to the electric and the magnetic field. X-rays can be produced by acceleration of electrons across a high potential through a vacuum tube hitting a target material. The potential must be high enough to excite the electrons in the target material. Energy is then released in a continuous spectrum with characteristic, discrete peaks for the particular target material, corresponding to transitions between the electron shells [2]:

$$\lambda[\mathring{\mathrm{A}}] = \frac{hc}{E} = \frac{12.398}{E[keV]}. \tag{5.1}$$

A monochromator is used in the case of powder diffraction. A transition from the L to the K shell produces K_α emission, while a transition from the M to the K shell produces K_β

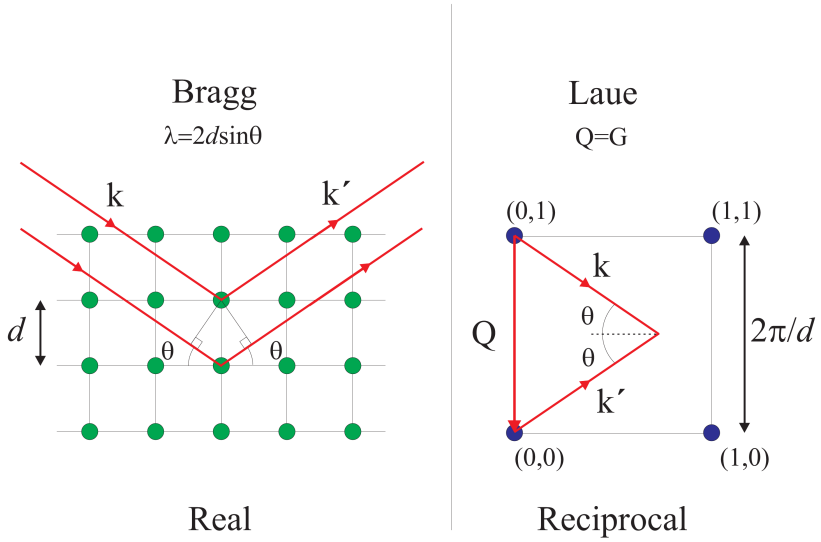

Figure 5.1: Left: Bragg reflection from planes separated by spacing d in a two-dimensional square lattice. Right: The same scattering event presented in reciprocal space. The lattice spacing in reciprocal space is $2\pi/d$. $Q = \frac{2\pi}{d}(0,1)$. From [2].

emission and so forth. Because there are sublevels in the electronic configuration, there will be a $K_{\alpha 1}$ and a $K_{\alpha 2}$ emission from the two allowed electron transitions in the $2p$ orbital.

X-rays interact with electrons of an atom and will be scattered or absorbed, and therefore have poor penetrating abilities as compared to neutrons. However, x-rays are useful for studying powder diffraction data and looking at the surface of a sample as seen below.

5.1.1 Powder diffraction

For powder diffraction a monochromatic x-ray beam is needed in order to be able to characterize a sample from the powder diffraction data. The monochromatic x-ray beam makes it possible to keep the incident wavevector constant for a scan over the measured angle, 2θ, where θ is the scattering angle in Figure 5.1.

Performing powder diffraction, a sample is crushed into a very fine powder, ensuring a uniform sample with an isotropic distribution of the orientation of crystal grains. In such an ideal powder sample, the direction of a particular reciprocal lattice vector, $\mathbf{G}_{hkl}$, will be distributed isotropically over a sphere. The grains which are positioned correctly for a fixed incident wavevector, $\mathbf{k}$, will Bragg reflect in a circle on the sphere. The scattered wavevectors, $\mathbf{k}'$, span a Debye-Scherrer cone [2] (Fig. 5.2, left). An example of powder diffraction data is given in Figure 5.2(right) as a function of 2θ and is thus a one-dimensional projection of the scattered wavevectors $\mathbf{k}'$.

The data analysis program FullProf used for analysing powder diffraction data in Section 6.4 is based on the Rietveld method [2, 53]. The basic principle of data interpretation using this method is first to identify the size and symmetry of the unit cell of the compounds present in a sample so that the lines in the powder diffraction data can be identified using the correct values of (h, k, l). Secondly, the intensity profile of the measured data is converted into structure factors which are then converted into a structure model. Finally, the structure model is refined using the entire diffraction profile. For information on how the measured

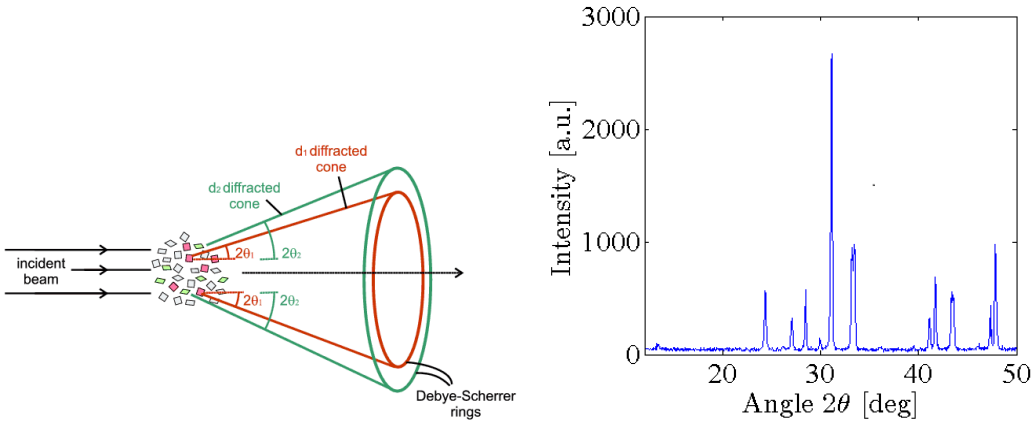

Figure 5.2: Left: An illustration of the Debye-Scherrer cone spanned by two different scattering angles measured in 2θ. From [4]. Right: An example of powder diffraction data after having scanned a sample through $2\theta = 0 - 50°$.

intensity is related to the structure factor, see for example Chapter 5.6.1 in Als-Nielsen and McMorrow (2011) [2].

In Section 6.4, examples of analysis of powder diffraction data and the subsequent refinement are given.

5.1.2 Laue back-scattering technique

Laue back-scattering with white x-rays can be used to finding the orientation of a single crystal or in the case of single crystal growth, performing preliminary checking that the sample is indeed a single crystal (Chap. 6). This is done by placing an image plate between the white x-ray source and a sample. The part of the incident beam that hits the sample at an angle 2θ to the crystal planes, such that it fulfills Bragg's law, is diffracted in the backwards direction from the sample onto the image plate (Fig. 5.3) and is recorded as Laue spots. The Laue spots symbolize the crystal lattice and its orientation. If for example a LSCO single crystal sample in the orthorhombic phase is positioned such that one of the axes of the crystal is at a normal to the plane spanned by the image plate, the Laue spots will lie in a straight line vertical in the Laue picture. If the axis is skewed to either side of the direction of the beam, the line of Laue spots will be a hyperbola.

From Laue back-scattering, it is therefore possible to find the orientation of a known crystal structure and to check that the pattern represents the wanted structure of a lattice. Examples of the use of the Laue back-scattering technique can be found in Section 6.6 and 7.2.

5.2 Neutron scattering

This section is unless otherwise stated based on Shirane, Shapiro, and Tranquada's book on neutron scattering from a triple-axis spectrometer [48].

Neutron scattering is an effective means for studying nuclear and magnetic structure and dynamics on atomic and nanometer scale in many different science disciplines such as solid state physics, molecular biology and polymer chemistry. The neutrons used in scattering

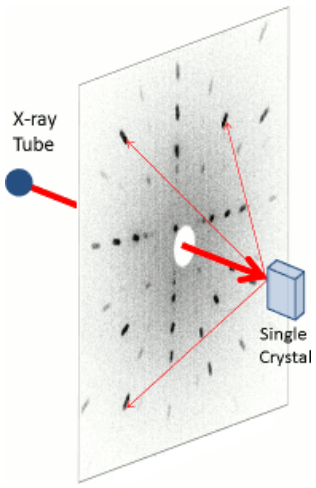

Figure 5.3: A schematic of the Laue back-scattering technique. White x-rays hit a sample and is back-scattered onto an image plate recording the Laue reflections. The position of the Laue spots will depend on the scattering angle. From [33].

Property	Magnitude
Charge	0
Spin	$\frac{1}{2}$
Rest mass, m_n	$1.675{\cdot}10^{-27}$ kg
Magnetic moment, μ_n	1.913 μ_N
Nuclear magneton, μ_N	$\frac{e\hbar}{2m_p} = 5.051 \cdot 10^{-27}$ J/T

Table 5.1: Some properties of neutrons [48].

experiments are created in a nuclear reactor by spontaneous fission of ^{235}U or in a spallation source by bombarding heavy elements with high-energy protons. The neutron source at Institut Laue-Langevin (ILL), where the experiments in Chapter 7 took place, is a reactor source. The neutrons used for the experiment were in the thermal region, which is defined as the range $1-100$ meV (approximately $9-0.9$ Å) [48]. The neutrons are moderated from the MeV-regime to the meV-regime using for example H_2O or liquid H_2. Some properties of neutrons are listen in Table 5.1.

The nature of neutron scattering from a nucleus is considered isotropic because the neutrons are scattered by the strong force in the nucleus, which is in the range of femtometers. This range is much smaller than that of neutron wavelengths in the range of Å. Therefore, neutrons cannot probe the internal structure of a nucleus. The scattering from a nucleus is characterized by the scattering length, b, which is isotope dependent. Because neutrons are made up of quarks, they possess a magnetic moment (Tab. 5.1), which makes it possible to study magnetic properties in solids by interaction between neutrons and unpaired electron spins in magnetic atoms.

As a consequence of quantum mechanics and the wave-particle duality, neutrons can be described as particles as is the case in the process of neutron creation as described above, and in the case of neutron detection, but as interfering waves in scattering processes. The de-Broglie wavelength is the wavelength which can be assigned a particle of mass, m, moving at constant velocity, v [29]:

$$\lambda = \frac{2\pi\hbar}{mv}, \tag{5.2}$$

where the velocity of neutrons are distributed according to a Maxwell-Boltzmann distribution.

The wave number, $k = \frac{2\pi}{\lambda}$, or the wave vector, $\mathbf{k} = \frac{m_n \mathbf{v}}{\hbar}$, are usually used in neutron scattering for the wave nature of the neutrons. The kinetic energy of the non-relativistic neutrons is given by $E = \frac{\hbar^2 k^2}{2m_n}$.

Neutron scattering processes are governed by the following laws of momentum and energy conservation:

- Momentum conservation for the scattering vector: $\mathbf{Q} = \mathbf{k}_f - \mathbf{k}_i$
- $Q^2 = k_i^2 + k_f^2 - 2k_i k_f \cos 2\theta$
- Energy conservation for inelastic scattering: $\hbar\omega = E_i - E_f$

Elastic scattering

For elastic scattering there is no momentum transfer, i.e. $|\mathbf{k}_i| = |\mathbf{k}_f|$. In case of elastic Bragg scattering (Fig. 5.1), the Laue condition must be fulfilled, i.e. the scattering vector, $\mathbf{Q}$, must be equal to the reciprocal lattice vector, $\mathbf{G}$:

$$\mathbf{Q} = \mathbf{G} = \mathbf{k}_f - \mathbf{k}_i \tag{5.3}$$

Using Bragg's law, $\lambda = 2d\sin\theta$ and that $d = \frac{2\pi}{|\mathbf{G}|}$ this can be written as

$$|\mathbf{G}| = \frac{4\pi}{\lambda}\sin\theta. \tag{5.4}$$

Elastic scattering is used for probing the atomic or static magnetic structure of a sample.

Inelastic scattering

For inelastic scattering, there is transfer of energy, i.e. $|\mathbf{k}_i| \neq |\mathbf{k}_f|$. The momentum transfer is described by:

$$\mathbf{Q} = \mathbf{G} + \mathbf{q}, \tag{5.5}$$

where the energy transferred to the sample is given by $\hbar\omega = E_i - E_f = \frac{\hbar^2}{2m_n}(k_i^2 - k_f^2)$. Inelastic neutron scattering is used to probe for example excitations of a crystal lattice, phonons, or excitations of the electron spin in a crystal lattice, magnons; $\mathbf{q}$ is then the wave vector of the excitation and $\hbar\omega$ its energy.

5.2.1 Differential cross section for nuclear scattering

The partial differential cross section of neutron scattering is the number of neutrons scattered into a solid angle, $\mathrm{d}\Omega$, with final energy in an interval E_f to $E_f + \mathrm{d}E_f$. The partial differential cross section consists of a coherent and an incoherent part. The coherent part provides information about elastic Bragg scattering and inelastic scattering from phonons. The incoherent part stems from the fact that not all equivalent nuclei have the same scattering length, b, which is dependent on the nucleus of an atom and therefore isotope dependent, or from disordering in the lattice. Incoherent scattering also originates from variations in spin

inside the nucleus. The spins point in different directions except at extremely low temperatures and in very high fields. Incoherent scattering is therefore isotropic, whereas coherent scattering is dependent on $\mathbf{Q}$. Only cross sections for coherent scattering are treated in this thesis.

The partial differential cross section is given by:

$$\frac{d^2\sigma}{d\Omega_f dE_f} = \frac{k_f}{k_i}\left(\frac{m_n}{2\pi\hbar^2}\right)^2 |\langle \mathbf{k}_f\lambda_f|\mathbf{V}(\mathbf{Q})|\mathbf{k}_i\lambda_i\rangle|^2\delta(\hbar\omega + E_i - E_f) \tag{5.6}$$

where λ_i and λ_f is the initial and final state of the sample, and because of the weak, short-ranged interaction, the interaction, $V(\mathbf{Q})$, can be approximated to $V(\mathbf{Q}) = \frac{2\pi\hbar^2}{m_n}b$. Using the Born approximation that incoming and outgoing waves can be treated as plane waves, a system with N nuclei can be rewritten as:

$$\frac{\mathrm{d}^2\sigma}{\mathrm{d}\Omega_f \mathrm{d}E_f} = Nb^2\frac{k_f}{k_i}S(\mathbf{Q},\omega) \tag{5.7}$$

where $S(\mathbf{Q},\omega)$ is the scattering function that gives the probability that some scattering event changes the energy of a system by $\hbar\omega$ and its momentum by $\hbar\mathbf{Q}$ given by:

$$S(\mathbf{Q},\omega) = \frac{1}{2\pi\hbar N}\sum_{ll'}\int_{-\infty}^{\infty} dt\, e^{-i\omega t}\left\langle e^{-i\mathbf{Q}\cdot\mathbf{r}_{l'}(0)}e^{-i\mathbf{Q}\cdot\mathbf{r}_l(t)}\right\rangle \tag{5.8}$$

where t is time, and $\langle ...\rangle$ is the average over initial states in the sample. From $S(\mathbf{Q},\omega)$, it is possible to determine microscopic properties related to the crystal lattice and its vibrations in a sample, and it is therefore the goal for most neutron scattering experiments to determine $S(\mathbf{Q},\omega)$.

5.2.2 Differential cross sections for magnetic scattering

If the signal is magnetic, the cross section and scattering function will look slightly different. Using elastic magnetic scattering it is possible to determine the magnetic structure of a sample, and using inelastic scattering scattering it is possible to probe for magnetic excitations. Neutrons scatter from the magnetic moment of a magnetic nucleus in an atom via the dipole-dipole interaction.

The magnetic inelastic differential cross section of an atom with one type of magnetic atoms is given by:

$$\frac{d^2\sigma}{d\Omega_f dE_f} = \frac{N}{\hbar}\frac{k_f}{k_i}\left(\frac{\gamma r_0}{2}\right)^2 g^2F(\mathbf{Q})^2e^{-2W}\sum_{\alpha\beta}(\delta_{\alpha\beta} - \hat{Q}_\alpha\hat{Q}_\beta)S^{\alpha\beta}(\mathbf{Q},\omega), \tag{5.9}$$

where

$$S^{\alpha\beta}(\mathbf{Q},\omega) = \frac{1}{2\pi}\int_{-\infty}^{\infty} dt\, e^{-i\omega t}\sum_l e^{i\mathbf{Q}\cdot\mathbf{r}_l}\left\langle S_0^\alpha(0)S_l^\beta(t)\right\rangle. \tag{5.10}$$

In Equation 5.9, $\gamma = 1.913$ and is the gyromagnetic ratio, which relates the magnetic moment and the angular moment of an atom; α and β are cartesian coordinates that can take any value of x, y, z; r_0 is the electron radius, $r_0 = e^2/(m_e c^2)$; g is the Landé splitting factor; the temperature-dependent Debye-Waller factor, e^{-2W}, takes into account the thermal vibrations of atoms away from their equilibrium positions; $F(\mathbf{Q})$ is the normalized

Fourier transform of the unpaired spin density, $\rho_s(\mathbf{r})$, on an atom, and depends on the spatial distribution of the spin and on the scattering vector:

$$F(\mathbf{Q}) = \int \rho_s(\mathbf{r}) e^{i\mathbf{Q}\cdot\mathbf{r}} d^3r. \tag{5.11}$$

$F(0) = 1$ for $Q = 0$, and falls off smoothly to zero for large scattering vectors, $\mathbf{Q}$.

Only the component of $\mathbf{S}$ perpendicular to $\mathbf{Q}$ will give a contribution to the scattering amplitude:

$$|\mathbf{S}\perp|^2 = |\hat{\mathbf{Q}} \times (\mathbf{S} \times \hat{\mathbf{Q}})|^2 = |\mathbf{S} - \hat{\mathbf{Q}}(\hat{\mathbf{Q}} \cdot \mathbf{S})|^2 = \sum_{\alpha\beta} (\delta_{\alpha\beta} - \hat{Q}_\alpha \hat{Q}_\beta) S^*_\alpha S_\beta. \tag{5.12}$$

In Equation 5.10, $\langle ... \rangle$ is the thermal average over correlations between two spins separated by time, t, and distance, l, Fourier transformed in space and time.

5.2.3 Fluctuation-dissipation theorem

The scattering function is related to the imaginary part of the dynamic susceptibility of a magnetic system. The relation is given by the fluctuation-dissipation theorem:

$$S(\mathbf{Q}, \omega) = \frac{\chi''(\mathbf{Q}, \omega)}{1 - e^{\hbar\omega/(k_B T)}} \tag{5.13}$$

So if $S(\mathbf{Q}, \omega)$ is retrieved from experimental data, this provides a direct relation between theory and experiment.

5.2.4 Elastic nuclear and magnetic scattering

Elastic nuclear scattering stems from ordered structures in a crystal lattice. The cross section for coherent elastic scattering, when the Laue condition for scattering is fulfilled, is given by [29]:

$$\left.\frac{d\sigma}{d\Omega}\right|^{el}_{coh} = e^{-2W} |\sum_j b_j e^{i\mathbf{Q}\cdot\mathbf{r}_j}|^2 = N \frac{(2\pi)^3}{V_0} e^{-2W} |F_N(\mathbf{Q})|^2 \sum_{\mathbf{G}} \delta(\mathbf{Q} - \mathbf{G}), \tag{5.14}$$

where the first sum is the lattice sum over lattice vectors $\mathbf{r}_j$. N is the number of lattice sites, V_0 is the unit cell volume, and $\mathbf{G}$ is a reciprocal lattice vector satisfying $e^{i\mathbf{r}\cdot\mathbf{G}} = 1$, where $\mathbf{r}$ is any lattice vector. The nuclear structure factor is a sum over all lattice vectors in a unit cell:

$$F_N(\mathbf{Q}) = \sum_j \bar{b}_j e^{i\mathbf{Q}\cdot\mathbf{d}_j}, \tag{5.15}$$

where $\mathbf{d}_j$ is the atomic position within a unit cell.

Coherent elastic scattering from magnetic structures in a sample gives rise to magnetic Bragg peaks from reciprocal lattice vectors matching the magnetic structure. The differential cross section is given by [29]:

$$\left.\frac{d\sigma}{d\Omega}\right|^{magn.el}_{coh} = \frac{N(2\pi)^3}{V_0} \left(\frac{g}{2}\right)^2 (\gamma r_0)^2 e^{-2W} |F(\mathbf{Q})|^2 |F_M(\mathbf{Q})|^2 \sum_{\mathbf{G}_M} \delta(\mathbf{Q} - \mathbf{G}_M) \tag{5.16}$$

where $\mathbf{G}_M$ is the magnetic ordering vector. The magnetic structure factor is given by:

$$F_M(\mathbf{Q}) = \sum_{\mathbf{d}} e^{-i\mathbf{Q}\cdot\mathbf{d}} < \mathbf{s}\perp(\mathbf{d}) > \tag{5.17}$$

and sums over the lattice vectors, $\mathbf{d}$, in a magnetic unit cell. $\langle \mathbf{s}\perp(\mathbf{d}) \rangle$ is the thermal average of the spins perpendicular to the scattering vector, $\mathbf{Q}$.

5.2.5 Triple-axis spectrometer

The experiments in Chapter 7 was conducted at ILL using the cold neutron triple-axis spectrometer (TAS), IN12. An illustration of the instrument is given in Figure 5.4. For a more accurate description of IN12 and the settings used for the experiments, see Chapter 7.

An advantage of triple-axis spectrometry is that it is possible to select E_i, E_f and $\mathbf{Q}$ freely within the limits of the instrument. As the neutrons arrive from the source and moderator to the instrument, they are distributed according to a Maxwell-Boltzmann distribution. They are led through a neutron guide to a velocity selector, where the desired range of the initial energy of the neutrons is chosen. The neutrons are then led through a neutron guide to the monochromator, where k_i and k_f are chosen by a monochromator and an analyzer, respectively. The sample is placed between the monochromator and the analyzer and a monitor is placed between the monochromator and the sample.

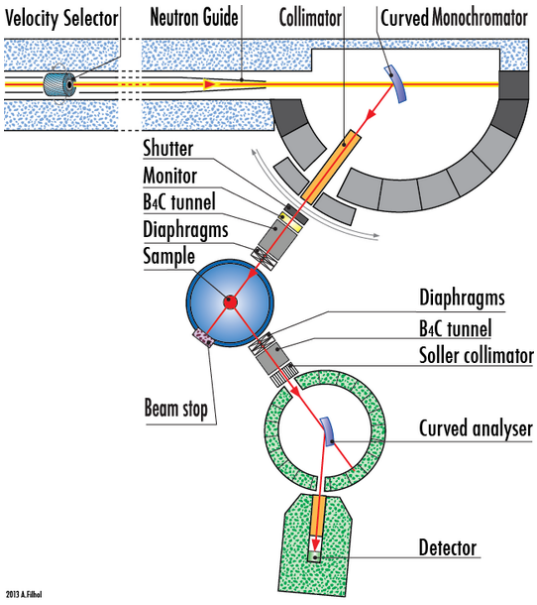

Figure 5.4: Illustration of IN12 setup from [17].

The angle between $\mathbf{k}_i$ and $\mathbf{k}_f$ is labelled 2θ and the orientation of the sample is labelled Ω. The magnitude of the scattering vector, $\mathbf{Q}$, is controlled by adjusting the angle 2θ, and the orientation of $\mathbf{Q}$ within the sample is controlled by rotating the sample, Ω. This means that any point in reciprocal space can be reached by changing either one of the angles or both of them. By rotating both 2θ and Ω, it is possible to make scans which are straight lines in reciprocal space. This has the advantage of being able to scan over for example the incommensurate peaks in steps of units of h, k, and l (Chap. 7).

5.2.6 Resolution

The divergence of a neutron beam can to some extend be limited by inserting collimators, which are parallel neutron absorbing plates with some width and height separated by some distance, which determines the collimation of the beam. Closely spaced collimator plates will result in a high collimation of the beam. But although collimators ensure a higher resolution of the neutron scattering data, it is at the expense of flux reaching the sample. It is therefore always a give and take situation, determining the settings of a neutron scattering experiment.

The observed intensity is related to the scattering function by the convolution integral [56]:

$$I_s(\mathbf{Q},\omega) = \int\int R(\mathbf{q}-\mathbf{Q},\omega'-\omega)S(\mathbf{q},\omega')d\mathbf{q}d\omega'. \tag{5.18}$$

where $R(\mathbf{q}-\mathbf{Q},\omega'-\omega)$ is the instrumental resolution function, which defines the probability as a function of $\Delta\mathbf{Q} = (\mathbf{q}-\mathbf{Q})$ and $\Delta\omega = \omega'-\omega$ of detecting a neutron when the instrument is set to measure a scattering process at $(\mathbf{Q},\omega)$. The resolution function is given by [48]:

$$R(\mathbf{Q},\omega) = \left(\frac{\hbar^2}{m_n}\right)\int d\mathbf{k}_i d\mathbf{k}_f P_i(\mathbf{k}_i)P_f(\mathbf{k}_f)\delta(\mathbf{Q}-\mathbf{k}_f+\mathbf{k}_i)\times\delta\left[\omega-\left(\frac{\hbar}{2m_n}\right)(k_i^2-k_f^2)\right] \tag{5.19}$$

The resolution is described by distributions around averaged wave vectors, $\mathbf{k}_i$ and $\mathbf{k}_f$. Because real crystals are often imperfect, the intensity of the reflection will have a distribution, a rocking curve, around some average value. This distribution is often considered a Gaussian. The mosaicity is given by the FWHM of a Gaussian fitted to a Bragg peak of a sample. The distributions $P_i(\mathbf{k}_i)$ and $P_f(\mathbf{k}_f)$ are determined by the mosaicity of the monochromator and the collimation of the beam.

Calculation of the resolution in regard to a specific experiment can be done in the program ResLib [60], which is an analytic MatLab code that implements Eq. 5.18 and 5.19. ResLib is used in order to account for the fact that the resolution function is dependent on values of $\mathbf{k}_f$, $\mathbf{k}_i$, energy transfer, $\hbar\omega$, and position in reciprocal space (h,k,l).

Chapter 6

Crystal growth of LSCO

The ceramic nature of $La_{2-x}Sr_xCuO_4$ (LSCO) crystals makes them very fragile and difficult to grow. Furthermore, quite large single crystal samples are needed in order to study them using neutron scattering. The basic principle of LSCO crystal growth is to create a feed rod and a seed rod of carefully prepared LSCO powder and a solvent pill with a lower melting point and use the traveling solvent float zone (TSFZ) method, used by Kimura and Shindo in 1977 [20], to grow a large single crystal. Learning to grow LSCO single crystals with the TSFZ method is a long process of trial and error and hands-on experience even if a manual is available.

The goal of the LSCO growing project was to create single crystal LSCO in the region x =0.02-0.07 in steps of $x = 0.01$. The idea is to study their low energy spin fluctuations and magnetic order in a strong applied field at low temperatures. Next, the crystals should be superoxygenated in order to perform further studies on the phase-separation of the magnetic ordered phase and the superconducting region in LSCO+O as described in Chapter 4. This chapter contains information on how to grow the crystals as well as to characterize them.

6.1 Preparing feed and seed rod

Powders of lanthanum (III) oxide (La_2O_3), copper (II) oxide (CuO) and strontium carbonate ($SrCO_3$) of high purity (>99.99%) are carefully weighted out in the desired stoichiometric concentrations for obtaining $La_{2-x}Sr_xCuO_4$. An example for $x = 0.05$ is given in Table 6.1. The concentration of strontium carbonate and lanthanum (III) oxide are adjusted according to the required doping level. All three powders are fine powders, which should not be inhaled or ingested. Strontium carbonate and lanthanum (III) oxide are fine, white powders, and CuO is a black, even finer powder which sticks to everything. All three powders are kept in a glovebox in argon atmosphere with a 10 mbar argon overpressure. This is especially important for La_2O_3, which will react with water in air and form a hydroxide, $La(OH)_3$. To avoid reactions with atmospheric air, all three powders are therefore measured out and put in a polyethylene bottle in the glovebox. The bottle with the powders are then carefully mixed for two days in a powder shaker.

After mixing, the powders are calcined at 950°C for two days in a container of aluminium oxide ceramic. The powder is then taken out, grinded using mortar and pestle, and the process is repeated so that the powders are calcined minimum two times. Calcination takes place below the melting point of any of the substances, but the temperature is sufficiently high for them to react and form $La_{2-x}Sr_xCuO_4$ and carbon dioxide originating from stron-

	$SrCO_3$	La_2O_3	CuO
Molar mass [g mol^{-1}]	147.63	325.809	79.545
Amount of substance [mol]	0.05	0.975	1.00
Mass [g]	1.824	78.515	19.661

Table 6.1: An example of a 100 g powder batch, $La_{2-x}Sr_xCuO_4$, $x = 0.05$.

Figure 6.1: To the left, a pressed rod as it looks once removed from the silicone tube before sintering. The three powders to the right show the progression from right to left from initial mixing to after the second calcination.

tium carbonate is driven out. During the calcination processes, the powder should go from a light grey, inhomogeneous powder to an all black, homogenous powder (Fig. 6.1).

The next step is to press the feed and the seed rod. In this project, these rods are essentially the same, only the length and the position in which they are placed in the mirror furnace differ. A single crystal can also be used as a seed rod. Pressing is done in a silicone tube with brass stoppers and should give a rod of 6 mm in diameter and approximately 10 cm in length for the feed rod and around 2 cm for the seed rod. Of course, these sizes can be changed, but this was the sizes that worked best in this project. The silicone tube is pressed in a condom for vacuum at a hydrostatic pressure of approximately 100 kp cm^{-2} ($\approx$ 100 bar) for about five minutes (Fig. 6.2). To ensure a good quality single crystal and to ease the process in the mirror furnace, it is extremely important that the pressed rods are as straight as possible. After being pressed, the rod is carefully cut out of the silicone tube with a scalpel. The rod is extremely fragile at this point and must be put in the vertical oven for sintering within a short amount of time not to fall apart. A 1 mm hole is drilled through one end of the rod, and the rod is hung in a platinum wire in a vertical oven where it is left for approximately 48 h at 1100°C. Sintering a powder is a way of creating a solid without reaching the melting point of the compound. During the sintering the rod is rotated and moved up and down to obtain a uniform thermal treatment of the rod. A sintered rod of approximately 10 cm and 6 mm in diameter has a mass of approximately 20 g.

6.2 Solvent

The melting point of LSCO is 1320°C, but it can be lowered if excess CuO is added according to the phase diagram derived by Oka and Unoki [35] (Fig. 6.3). This is exploited in the solvent pill which is made in basically the same way as the feed and seed rod, but with a 80 mol% CuO content. An example of masses needed for a batch of solvent powder, $x = 0.05$, is given in Table 6.2. As for the rods, the powder is calcined at least twice, before it is pressed. The solvent pills are pressed in the same way as the feed and the seed rod,

	$SrCO_3$	La_2O_3	CuO
Molar mass [g mol^{-1}]	147.63	325.809	79.545
Amount of substance [mol]	0.0098	0.1902	0.800
Mass [g]	1.134	48.783	50.084

Table 6.2: An example of a 100 g 80 mol% CuO solvent powder batch for LSCO with doping concentration $x = 0.05$.

but with a smaller diameter of the silicone tube. This is done so that the pill will not fall off when placed upon the seed rod in the mirror furnace (Fig. 6.2). The solvent pill should be roughly 0.5 cm high and have a mass of ~ 0.5 g.

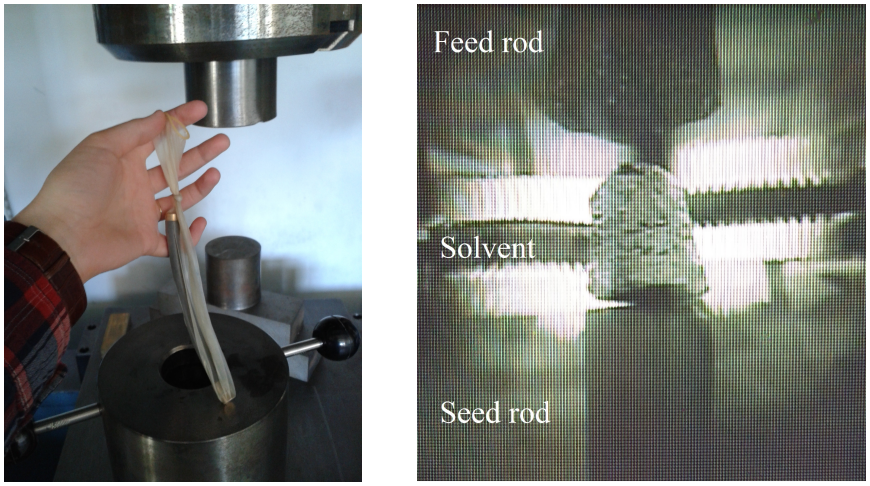

Figure 6.2: Left: A silicone tube with LSCO powder ready to be hydrostatically pressed into a rod. Right: The setup in the mirror furnace before the melting process begins.

The role of the solvent pills is to utilize the high content of CuO, 80 mol%, to create a molten zone in the TSFZ method (Sec. 6.3). From literature [35, 52], it has been established that the solvents must contain at least 80 mol% CuO in order to create single crystal LSCO, otherwise $La(OH)_3$ may form and the crystal will disintegrate as shown in Figure 6.5. This will be discussed further in the following sections.

6.3 Traveling solvent float zone method

The traveling solvent float zone (TSFZ) method was used by Kimura and Shindo in 1977 [20] to grow large single crystals of yttrium iron garnet. In 1989, Tanaki, Yamane and Kojima [52] reported that they had managed to grow single crystal LSCO with the TSFZ method and it has since been the preferred method for growing high quality single crystal LSCO.

The basic principle is to use a mirror furnace in which the seed and feed rod are placed in a vertical position above each other in a quartz tube, as seen in Figure 6.4. Halogen lamps and mirrors allow for very precise heat focus onto a specific place on the rods. A molten zone between the feed rod and the seed rod is then created, initially started by a solvent pill. This zone is carefully and with a very slow growth rate of 1 mm/h moved up along the feed rod while the two rods are counter-rotating with 25 rpm in order to ensure an even

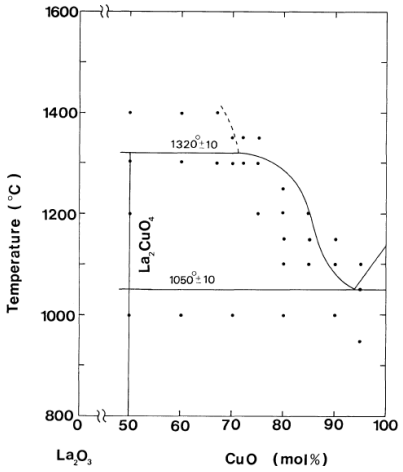

Figure 6.3: Phase diagram of the La_2O_3-CuO system in air from Oka and Unoki [35]. The dots indicate where quenching and x-ray analysis were done. The upper solid line represents the melting temperature of the La_2O_3-CuO system: At 50 mol% CuO, La_2CuO_4 is formed and its melting point is at 1320°C. By addition of excess CuO, the melting point is lowered in the range from 71 mol% all the way down to 1050°C at 94 mol% CuO.

distribution of heat. The growth rate and rotation rate are not definite values, but were found to work well. The TSFZ method was performed under atmospheric pressure and air.

Before the process begins, the feed rod is hung from a hook in a platinum wire. It is very important to secure that the rotation is centered precisely around a vertical axis, hence the straight rods, to secure a uniform growth zone. The solvent pill is placed upon the seed rod, the quartz tube is inserted, and the mirror furnace can then slowly be heated. The upper part of the solvent pill is slowly heated. Once it starts to melt, the feed rod is lowered onto the solvent pill which is then lifted up, now attached to the feed rod. The lower part of the solvent pill is then slowly melted and lowered onto the seed rod and fastened again. The heat is then slowly increased until a proper molten zone has been reached and the growth process can begin. The heat is further increased during the next couple of hours as the feed rod is entering the molten zone until an equilibrium is reached; since the CuO content, ∼50 mol%, is much lower in the feed rod than in the 80 mol% solvent pill, the melting point of the feed rod will be higher as illustrated in Figure 6.3, and more heat is therefore required.

Once the growth process has begun, it is extremely important to ensure a constant growth rate as CuO will melt with loss of oxygen from the feed rod; this is also why it is important to have a large content of CuO in the solvent pill in the beginning of the process. If too much CuO is lost from the sample, remnants of unreacted La_2O_3 will be present in the final crystal, and single crystal LSCO is not obtained. Thus, the best way to test whether single crystal LSCO is obtained is to leave it in air for a couple of days once the crystal is taken out of the mirror furnace. If unreacted lanthanum oxide is present in the sample or if it is not a single crystal, the crystal will simply disintegrate and fall apart. This is shown in Figure 6.5 for an attempt to grow an $x = 0.03$ single crystal. Disintegrated samples are also reported in Tanaka et al. [52]; they found by x-ray diffraction that excess La_2O_3 had reacted with water in air to form $La(OH)_3$, a white powder. This was also found to be the case for the crystal in Figure 6.5 (Fig. 6.9).

Examples of LSCO crystals, $x = 0.05$, $x = 0.06$, and $x = 0.07$ as they look when they

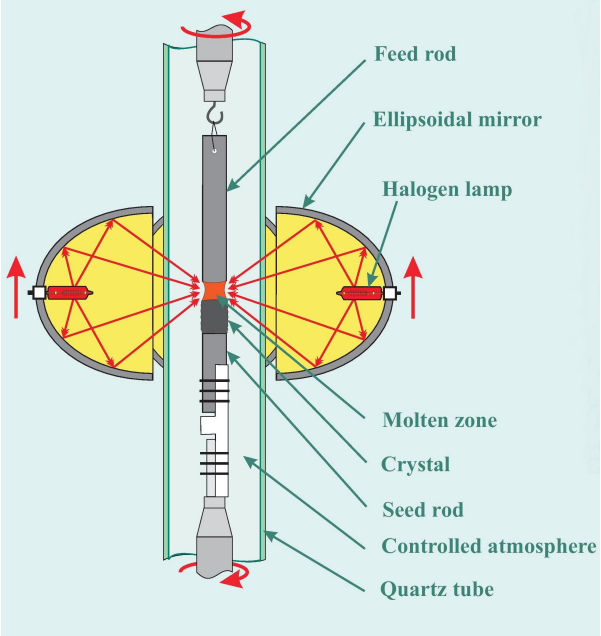

Figure 6.4: Experimental setup for using the traveling solvent float zone method from [13].

Figure 6.5: An example of a crystal sample as-grown (left) and after a few days left in air (right) kept in the same open container in air. Some white powder is visible after a few days, clearly indicating the presence of $La(OH)_3$.

are removed from the mirror furnace, are shown in Figure 6.6. For $x = 0.05$, the seed rod can be seen to the left (0-2 cm), the start-up zone where the system stabilizes (2-4 cm) and the actual single crystal (4-9 cm) and what is left of the seed rod. For $x = 0.06$, the seed rod can be seen to the right (9.5-11.5 cm), the start-up (8-9.5 cm) and the actual single crystal (4-8 cm) and what is left of the seed rod (0-2 cm). For $x = 0.07$, the seed rod can be seen to the left (0-3 cm), the start-up zone (3-4.5 cm) and the actual single crystal (4.5-9.5 cm).

Example of a LSCO crystal, $x = 0.04$, as it looks after it was left in air for a week (Fig. 6.7). The single crystal (0-5 cm), the start-up zone (5-8.5 cm) and the seed rod (8.5-10.5 cm) regions can be seen in the figure. It is clear that the start-up zone is not a single crystal, as it is has disintegrated. The areas of the single crystal for all doping concentrations show the characteristic features of the ceramic LSCO single crystal; a homogenous, black and shiny surface. Further characterization of the crystals can be found in Section 6.6.

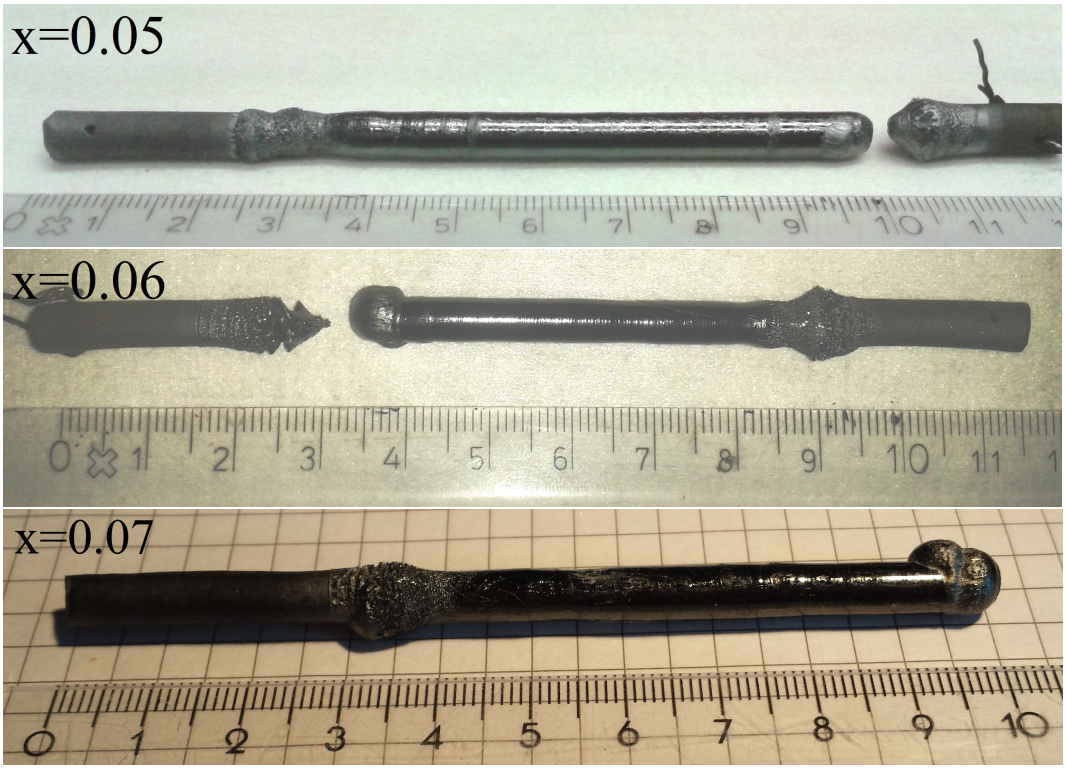

Figure 6.6: Examples of as-grown single LSCO crystals with $x = 0.05$, $x = 0.06$, and $x = 0.07$ once removed from the mirror furnace.

6.4 Characterization using powder diffraction

Powder diffraction has been used in the process of growing LSCO crystals to ensure the quality of the powders and that the right products were obtained. Examples of LSCO x-ray diffraction patterns for different values of $x \leq 0.125$ are given by Napoletano et al. [34] and for $0.11 \leq x \leq 0.16$ by Shen et al. [47]. As mentioned in Chapter 3, the bond lengths and therefore also the lattice parameters a, b and c in LSCO will change with doping concentration, which will of course affect the lattice structure. Napoletano et al. showed

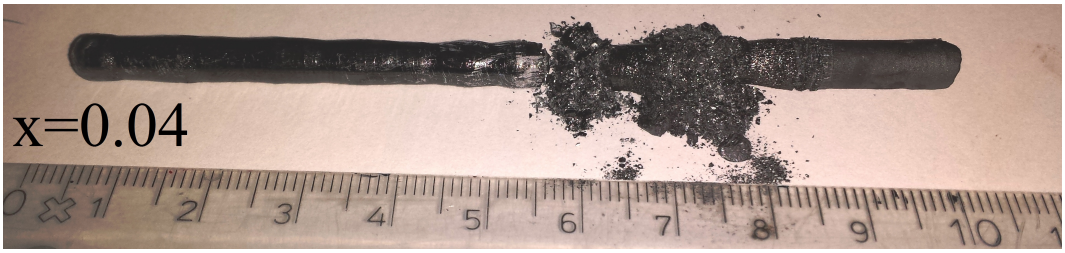

Figure 6.7: Example of single crystal LSCO, $x = 0.04$, left in air for a week.

with x-ray powder diffraction the phase transition at room temperature with increasing doping level from the orthorhombic phase to the tetragonal phase with a phase separation at $x < 0.1$ [34]. This was also shown in Figure 3.1. Hence, for the crystals grown in relation to this thesis, $x = 0.02 - 0.07$, the relevant structure to compare the powder diffraction data to is the orthorhombic phase.

Powder diffraction data in this thesis has been collected at DTU Risø and at HCØ, UCPH, using K_α transitions from copper and cobalt, respectively. With weighted average wavelengths Cu-$K_{\alpha,ave}$: 1.5418 Å, and Co-$K_{\alpha,ave}$: 1.7903 Å. The data was collected by scanning the sample in different intervals of the angle 2θ in steps of 0.01° or 0.04°.

In order to interpret the powder diffraction data, the program FullProf has been used. This program enables a Rietveld analysis of the powder diffraction data based on peer-reviewed data entries obtained from the Inorganic Crystal Structure Database [19]. From these data files, FullProf can construct a pcr-file containing information about the size and the symmetry of the compound in the data file, i.e. approximate cell parameters and atomic positions and occupancy. FullProf allows for a multi-phase analysis of powder diffraction data, in this way matching more than one compound to a set of powder diffraction data. This is exactly what is required for the kind of powder quality checking needed for this project.

The pseudo-Voigt function [53] is used in the refinement of these data. This function is an approximation of the Voigt profile which is a convolution of a Gaussian and a Lorentzian profile. The pseudo-Voigt profile is able to take into account instrumental resolution and intrinsic broadening from the Voigt profile, but can still be computed fairly easily. The pseudo-Voigt profile in Fullprof also takes into account the axial divergence symmetry, i.e. it corrects for the angular dependence of the peak shape [41].

Based on the pcr-file constructed for each compound, one multi-phase pcr-file is written containing information on the diffraction conditions and the crystallographic information needed for the refinement. FullProf will then, based on the input multi-phase pcr-file and the data file containing the measured profile intensity of the powder diffraction data, identify peaks using h, k, l in the diffraction data. The refinement can then begin; the data is fitted to the parameters phase scale factor, zero, background, lattice parameters, atomic positions, FWHM parameters of the pseudo-Voigt profile etc., until a satisfying result is reached.

After the refinement, FullProf allows for a quantitative phase analysis; from a multi-phase refinement the weight fraction, W_j, of each refined phase is written in an output file based on input and refined parameters. For N phases, the weight fraction of phase j is [41]:

$$W_j = \frac{S_j Z_j M_j V_j / t_j}{\sum_i (S_i Z_i M_i V_i / t_i)} \tag{6.1}$$

Where S_j is the scale factor retrieved from the refined parameters of phase j, Z_j is the

number of formula units per unit cell for phase j, M_j is the molecular mass, V_j is the unit cell volume, and t_j is the Brindley particle absorption factor for phase j and is defined as:

$$t_j = \left(\frac{1}{A_j}\right) \int e^{-(\mu_j - \bar{\mu})x} \mathrm{d}A_j \tag{6.2}$$

Where μ_j is the particle linear absorption coefficient for phase j, $\bar{\mu}$ is the mean linear absorption coefficient of the powder, x is the path of the radiation in a particle of phase j, and A_j is the particle volume. The parameter t_j takes into account that different compounds in a particle have different absorption coefficients and it therefore acts as to correct for this effect. The particle sizes in powder diffraction are to a good approximation spherical. Brindley [7] tabulated values of t_j for spherical particles of radius R_j versus $(\mu_j - \bar{\mu})R_j$; these values can be given as input in FullProf. As the radius of the particles is the unknown parameter, careful preparation of the sample before doing x-ray powder diffraction is therefore important to ensure a uniform radius. The Brindley particle absorption factor is mainly important if the scattering vector is close to the sample plane. As this is not the case in this study, the Brindley particle absorbtion factor is ignored.

From the weight percentage output from FullProf it is straightforward to convert it to mole percentage. Quantitative phase analysis using Rietveld refinement has proven to be an important and useful tool in checking the different powders used for solvent pills and feed and seed rods. Powder diffraction data was fitted to the following phases: CuO, La_2O_3, LSCO, $SrCO_3$ and $La(OH)_3$. An example is given in Figure 6.8 for powder from LSCO, $x = 0.07$, after the second calcination. More examples are given in Appendix A.1. It was found that the sample contained 93% LSCO and 7% La_2O_3, and more CuO was therefore added to the sample and the calcination process was repeated. It is clear from Figure 6.8 that some of the larger LSCO peaks are a bit off, some in intensity and some in position. This could be an indication that the sample does not hold a doping value of exactly $x = 0.07$ as the diffraction profile is very sensitive to doping concentration, especially around 30-33° [34]. The doping concentration will have to be investigated further. It is possible to fit the data to doping concentration, but it would require powder diffraction data with much higher accuracy and in smaller steps. And perhaps more importantly, it would require that a piece of the single crystal LSCO was destroyed and powderized – it has therefore not been done.

The disintegrated sample of $x = 0.03$ (Fig. 6.5) was also studied with powder diffraction analysis. From Rietveld refinement (Fig. 6.9), it was found that the sample contained 45 mol% LSCO and 55 mol% $La(OH)_3$. As some of the peaks are off in intensity, the exact amounts should probably not be trusted. But it is a good indication of what has happened to the sample; CuO has disappeared, leaving unreacted La_2O_3, which has then eventually formed the hydroxide.

6.5 Improvements

While working on growing single crystal LSCO, several improvements have been implemented in the process, a few of them are included here.

The mirrors were moving upwards, securing a growth rate of 1 mm/h, but it was found that it was necessary to move the feed rod upwards as well. Otherwise, the molten zone would become too large with the possibility of loosing a droplet. The feed rod was moved upwards at a rate of 0.05 mm/h.

In other studies [23, 47, 52], the single crystals are grown under oxygen pressure to avoid the evaporation of CuO. Unfortunately, this was not possible during this project. As can

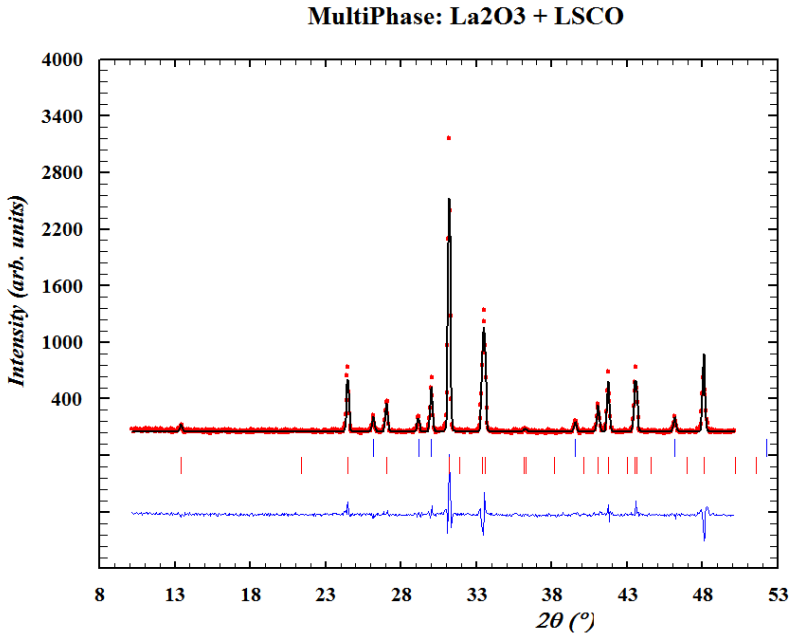

Figure 6.8: Rietveld refinement of powder diffraction data from LSCO, $x = 0.07$. Red points are data points, black line is the fit and the blue line below is the difference between fit and data. The bars below the data are structural peaks allowed for the different compounds. Upper blue: La_2O_3 and lower red: LSCO.

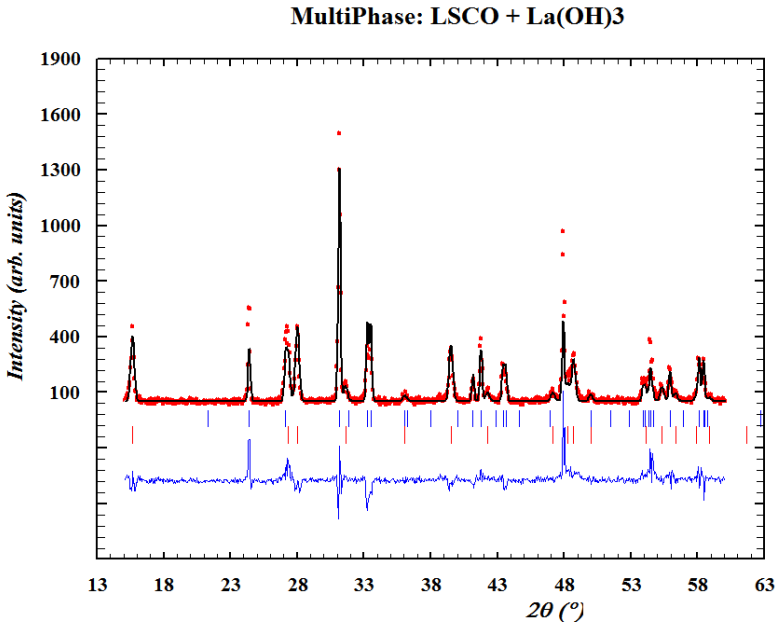

Figure 6.9: Rietveld refinement of powder diffraction data of the disintegrated crystal from Figure 6.5, $x = 0.03$. Red points are data points, black line is the fit and the blue line below is the difference between fit and data. The bars below the data are structural peaks allowed for the different compounds. Upper blue: LSCO and lower red: $La(OH)_3$.

be seen in Figure 6.5, one of the first crystals that we grew disintegrated after a few days. With analysis of powder diffraction data (Fig. 6.9) and because of visible white powder, it was learned that the sample contained $La(OH)_3$ as was reported in [34]. Therefore an extra 3 mol% CuO was added to the LSCO powders, which were then calcined again, before a feed and seed rod were pressed; this was also done by Shen et al. [47]. La_2O_3 and $SrCO_3$ will act as the limiting reagents, but the presence of excess CuO should help keep a stable molten zone without too much loss of oxygen. The results are seen in Figure 6.6.

The powders were mixed in a glovebox, where they were also put in a sealed low density polyethylene flask and then put in a powder shaker for a few days to ensure that the powders had been properly mixed before calcination. Other methods have been described in order to ensure a well-mixed homogenous powder before starting calcination that does not just involve shaking. The sol-gel method is described by Shen et al. [47] and is a long and tedious process that will take weeks to complete. In this process, the powders are first dissolved into nitric acid then made into a gel, which is finally heated without burning until it becomes a fine powder, ready for calcination.

Unfortunately, time did not allow for trying this process. Instead, the less time consuming method where the powders were mixed in ethanol, used by Tanaka et al. [52] and Napoletano et al. [34], was tried. A batch of LSCO powder, $x = 0.02$, was mixed in ethanol 99.9%, the result can be seen in Figure 6.10. From FullProf, it was found that the sample contained 3.3 mol% CuO and 96.7 mol% LSCO after one calcination which is very close to the 3 mol% excess CuO that was aimed for. Also, the powder seemed finer and much more homogenous and it was easier to pack it in the silicone tube before pressing the rod, which resulted in what seemed to be a better rod. Since at this point we had already grown single crystals

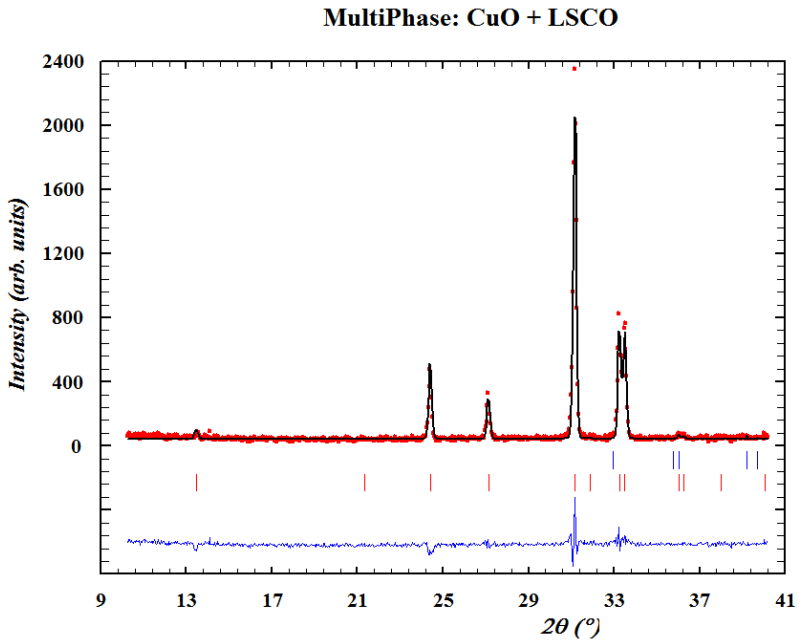

Figure 6.10: Rietveld refinement of powder diffraction data from LSCO powder mixed in ethanol, $x = 0.02$. Red points are data points, black line is the fit and the blue line below is the difference between fit and data. The bars below the data are structural peaks allowed for the different compounds. Upper blue: CuO and lower red: LSCO.

for $x = 0.04$, $x = 0.05$, and $x = 0.06$ and were in the calcination or sintering process of $x = 0.03$, mixing of powders in ethanol was only done for $x = 0.02$ and $x = 0.07$.

6.6 Characterization using Laue back-scattering

Characterization of grown LSCO crystals with $x = 0.04, 0.05, 0.06, 0.07$ has been done using the back-scattering Laue technique as explained in Section 5.1.2. An example of one of the crystals, $x = 0.05$, is shown in Figure 6.11. The Laue pattern is identical on all three Laue pictures taken along the growth direction of the crystal which suggests that it is indeed a single crystal.

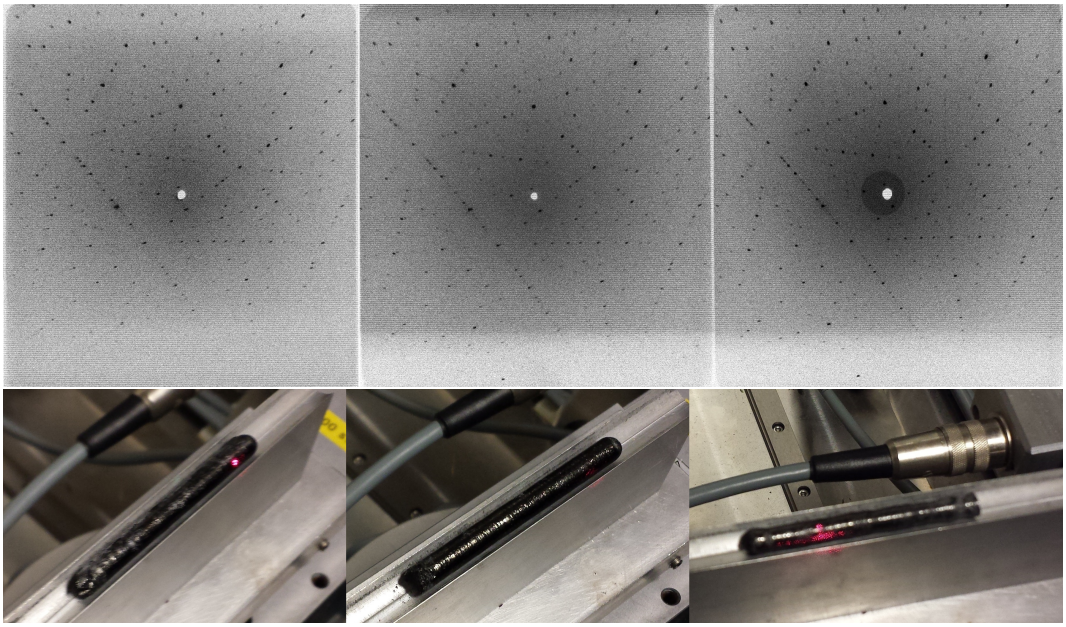

Figure 6.11: Top: Three Laue back-scattering pictures from LSCO, $x = 0.05$, taken along the direction of growth. Below: The pictures illustrate where on the crystal, the Laue pictures were taken.

Further characterization was done in the program OrientExpress V3.4 [27], where the lattice parameters, dimensions of the image plate, and the distance from the image plate to the crystal are given as inputs. This allows OrientExpress to analyze the pattern and identify in what direction the crystal is oriented. For this purpose, OrientExpress is also used to make preliminary check in order to determine whether the crystal grown is indeed a single LSCO crystal. Figure 6.12 shows Laue pattern for the $x = 0.05$ crystal (left) and the $x = 0.07$ crystal (right).

In Figure 6.13, Laue spots for the $x = 0.04$ and $x = 0.07$ crystals of high symmetry have been identified in OrientExpress and it shows how well the simulated (red) Laue spots fit with the measured Laue spots. The c-axis is found to be the axis closest to the vertical axis in both crystals. This is close to being perpendicular to the direction of growth.

For the $x = 0.05$ crystal in Figure 6.14, the c-axis is also found vertical in the picture. Clear signs of twinning are found in the $x = 0.05$ crystal (Fig. 6.14).

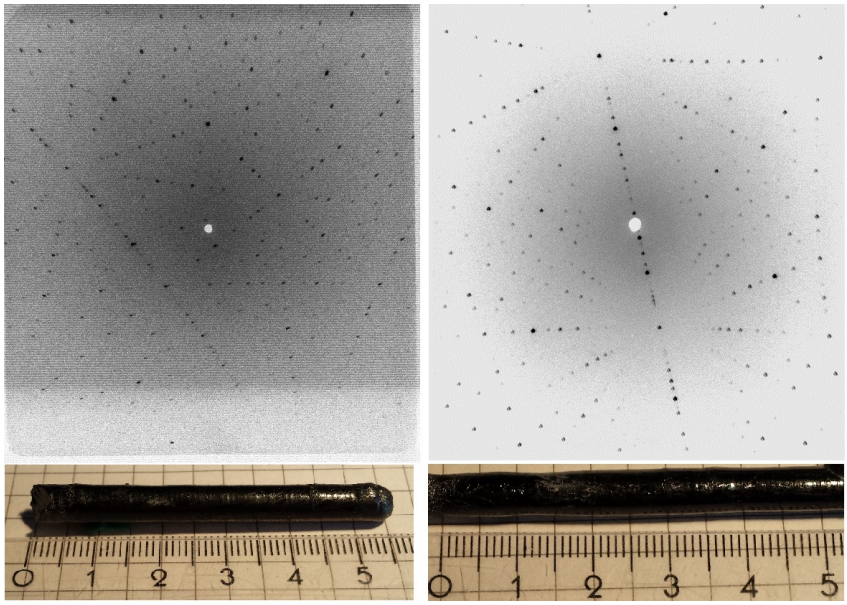

Figure 6.12: Laue back-scattering pictures from LSCO, $x = 0.05$ and $x = 0.07$.

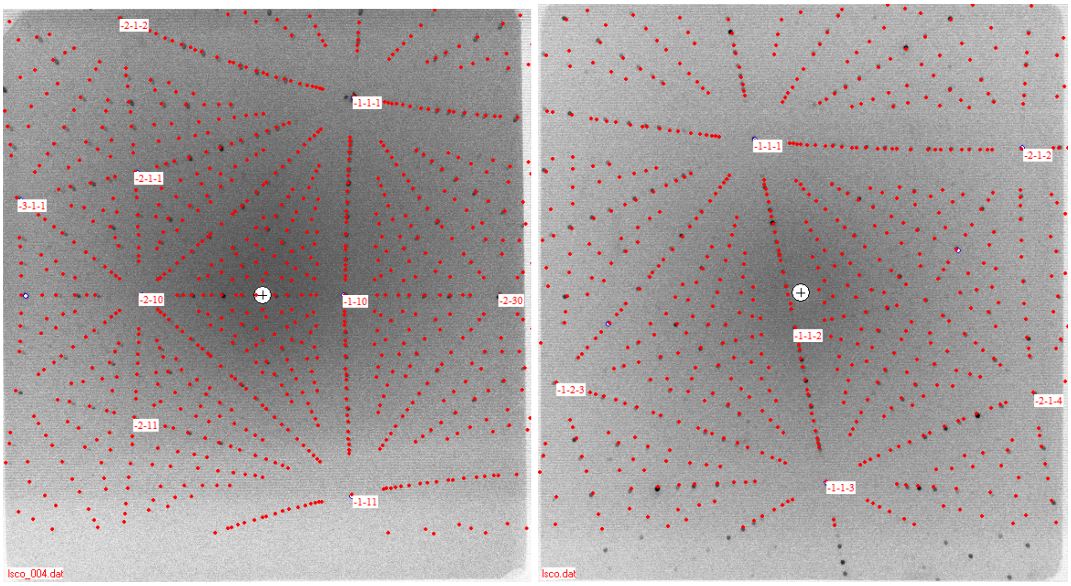

Figure 6.13: Laue back-scattering from $x = 0.04$ (left) and $x = 0.07$ (right) analyzed using OrientExpress. The c-axis is identified as the axes closest to vertical in the two pictures.

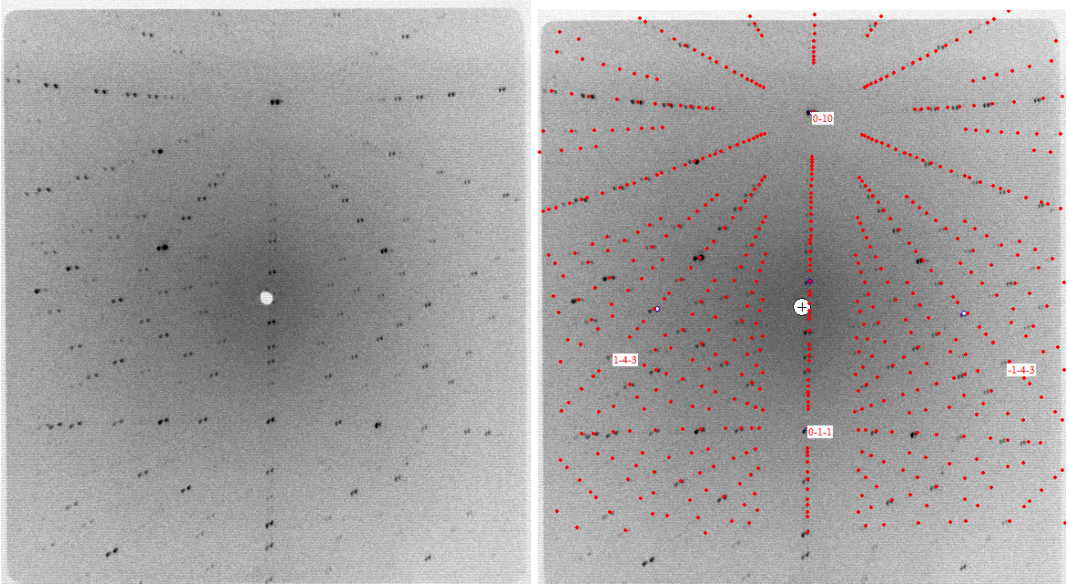

Figure 6.14: Clear signs of twinning is seen in the $x = 0.05$ crystal along the c-axis, which is the vertical axis in the picture (left). Identified high symmetry Laue spots are shown (right) in the same Laue picture as the one to the left.

Sr content	Status	Mass of crystal [g]
$x = 0.02$	Crystal was grown, almost completely disintegrated	0.65
$x = 0.03$	Crystal was grown, but has disintegrated (Fig. 6.5)	–
$x = 0.04$	Single crystal grown (Fig. 6.13)	4.27
$x = 0.05$	Single crystal grown, twinning (Fig. 6.14)	8.34
$x = 0.06$	Single crystal grown (Fig. A.8)	2.33
$x = 0.07$	Single crystal grown (Fig. 6.13)	9.23

Table 6.3: Status on LSCO crystal growth as of 1 June 2014.

6.7 Discussion

The status of the LSCO single crystal growth project as of 1 June 2014 is shown in Table 6.3. From the analysis of Laue reflections from the LSCO crystals grown, it is clear that crystal growing has to some extend been successful, even though it has been a long and difficult process. An example of the complexity is revealed from $x = 0.02$; having the best powder composition to press feed and seed rods from, is not nearly enough. Almost all of the $x = 0.02$ crystal disintegrated and powder diffraction analysis showed a very high content of lanthanum hydroxide. As higher power and more heat was used in the mirror furnace for this sample, this is another indication that CuO will melt at high temperatures with a loss of oxygen, which means that unreacted lanthanum oxide will be present in the crystal-as-grown, and after a few days, the sample will have disintegrated as the oxide has reacted with moist in air as shown in Figure 6.5 for $x = 0.03$. This illustrates the carefulness with which the mirror furnace should be handled.

However, single crystals of doping values $x = 0.04 - 0.07$ in varying amounts were successfully grown and are ready for further analysis and characterization.

Further characterization of the crystals should be done with neutron scattering, which have much better penetrating abilities and can therefore check the crystals all the way through and not just the surface. Neutron scattering can also give the quality of the sample by estimating the mosaicity and checking for twinning using structural peaks. According to Reehuis et al. [40], the degree of twinning can be determined by the ratio of the intensities from the peaks: $I(h0l)/I(0kl)$, with h odd and l even.

The exact doping concentration of the sample should also be checked by measuring the exact phase transition temperature for the HTT to the LTO phase. It is also worth checking, the gradient of Sr doping along the crystal in the direction of growth as reported in Kojima et al. [23].

A recent proposal by our group for beam time at the Paul Scherrer Institute, suggests a study in field on the crystals grown as part of this project and one more that will have to be grown for $x = 0.08$. The proposed study serves to investigate the role of a strong applied magnetic field on incommensurate magnetic signals around doping concentrations at the onset of superconductivity. This may allow access into the region above H_{c2} where superconductivity is completely suppressed. The purpose of the experiment is to investigate the coupling between high-temperature superconductivity, applied field and the incommensurate magnetic order.

Finally, the LSCO single crystals should be superoxygenated in order to perform studies, which will further develop the work from Udby et al. [55] and Mohottala et al. [31] on co-doped $La_{2-x}Sr_xCuO_{4+\delta}$.

Chapter 7

Low energy spin fluctuations in superoxygenated LCO+O

The experiment presented in this chapter was performed at IN12 at ILL in May and July 2013 by Henrik Jacobsen, Pia Jensen, Linda Udby, and Kim Lefmann from the Niels Bohr Institute at the University of Copenhagen. This study was performed on single crystal $La_2CuO_{4+\delta}$ (LCO+O). The aim of the experiments was to study the incommensurate antiferromagnetic (IC AFM) order and excitations using neutron scattering, as excitations of the IC AFM order seem to be related to high-temperature superconductivity. This has previously been studied for $La_{2-x}Sr_xCuO_4$ (LSCO) (e.g. [1, 22, 24, 42]), where a consequence of the IC AFM order was the opening of a spin gap around the transition temperature as described in Section 3.5. The findings from this experiment should be compared with studies of spin gap in LSCO and future studies of the co-doped material $La_{2-x}Sr_xCuO_{4+\delta}$ (LSCO+O) in order to move a step closer to understanding the effect of oxygen intercalation and ordering in superconductors compared to doping with immobile strontium atoms.

It has not been established yet whether there is an actual spin gap in LCO+O, although spin fluctuations were observed by Wells et al. [57] around 2 meV in LCO+O, $\delta = 0.055$. Therefore, this experiment serves to establish whether there is a spin gap in LCO+O and potentially the size of it. The study of a spin gap could also help in understanding the role of superoxygenation on the magnetic phase because of the electronic phase separation in LCO+O and LSCO+O between the stripe-like IC AFM phase and the superconducting phase.

The experiment was primarily conducted by studying inelastic signals from incommensurate IC AFM signals at low energy transfers in the range $0.3 - 7$ meV at two different temperatures, 2 K and 45 K.

7.1 Experimental setup

The experiment was conducted at ILL at the triple-axis instrument IN12 (Fig. 5.4), which is positioned on the cold neutron guide H144. At this instrument, neutrons are led from the moderator into the neutron guide, which will reflect neutrons along the guide walls. The neutron guide is made of supermirrors consisting of layers of Ni-Ti. The critical angle of the neutron guide relative to that of pure nickel is $\theta_{c,Ni} \approx 0.1°/\text{Å}$ and for the mirror: $\theta_{c,mirror} = m\theta_{c,Ni}$ for $m = 2$ along the guide. The coating is increased to $m = 3.2$ before the exit of the guide.

A velocity selector is placed in the guide 33 m before the monochromator. The velocity selector eliminates neutrons of energies other than those desired for the experiment. This is done in order to avoid second or higher order neutrons at the monochromator or analyzer. Higher order neutrons with wavelengths $\frac{\lambda}{2}$, $\frac{\lambda}{3}$, etc. reflected from the monochromator or analyzer can cause reflections at positions otherwise not allowed or inelastic scattering from unexpected positions. In LSCO and LCO+O, the (200) position is an allowed Bragg reflection with lattice spacing, d, whereas (100) with lattice spacing $2d$ is not. However, higher order neutrons can cause reflections from (100). For $\frac{\lambda}{2}$: $\frac{\lambda}{2} = 2d\sin\theta \Leftrightarrow \lambda = 2(2d)\sin\theta$, which will give a reflection at the nominal (100) position.

A monochromator was placed 1800 mm after the guide exit. The monochromator is a pyrolytic graphite (PG) crystal where the (002) reflection is used to select the incoming wavelength used in the experiment. The selection is done using the scattering angle θ: $|\mathbf{G}| = \sin(\theta)4\pi/\lambda$, where $|\mathbf{G}| = 1.8734$ Å^{-1}. The monochromator was vertically and horizontally focusing. The mosaicity of the monochromator was 35', which is a relatively large value in order not to lose too much intensity of the neutron beam.

The sample was placed 1850 mm after the monochromator. The distance from the sample to the analyzer was 700 mm. The analyzer was also a PG (002) crystal with horizontal and vertical focusing and a mosaicity of 35'. The detector was a cylindrical single tube He-3 detector. A monitor was placed between the sample and the monochromator. A monitor is an inefficient detector, which interacts with a small part of the neutron beam thereby determining the counting efficiency, which is then used for normalization purposes.

The collimators placed between monochromator-sample, sample-analyzer, and analyzer-detector were not used, but left open in order to maintain a high beam intensity.

During the first experiment, elastically scattered neutrons reaching the analyzer or higher order neutrons caused strange signals (Fig. 7.7). This proved to be a problem, and a Be-filter was inserted after the sample, before the analyzer in the second experiment. A Be-filter scatters neutrons above a threshold energy, 5.2 meV, thereby completely removing higher order neutrons from the beam.

7.2 Sample and alignment

The sample with a total mass of 15.494 g consisted of four cylindrical pieces of $La_2CuO_{4+\delta}$ single crystal (Fig. 7.1), which were originally one crystal. The LCO single crystal was grown in the same mirror furnace at DTU Risø as used for growing the LSCO crystals that were a part of this project (Chap. 6). Superoxygenation of the crystal was performed by the group of Barrett Wells at the University of Connecticut. A susceptibility curve of the LCO+O sample was measured at DTU Risø, and it showed that the onset of a change in the susceptibility curve was at 42 K and halfway down the susceptibility curve was at 40.5 K, which gives a critical temperature of 40.5±1.5 K.

Crystal	A11	A2	B2	B3	Total
Mass [g]	3.555	3.835	3.831	4.273	15.494

Table 7.1: The mass of the four single crystal pieces in Figure 7.1 and total sample mass.

A TGA analysis of a small sample piece has been done more than once in order to determine the excess oxygen content. Unfortunately, the results were not consistent and since a small part of the crystal has to be destroyed for each analysis, further characterization is therefore postponed until the experiments in-field have been conducted as well. But the

TGA analysis and the critical temperature of the sample suggest that the sample is in stage four with $\delta \approx 0.1$ (Fig. 4.2).

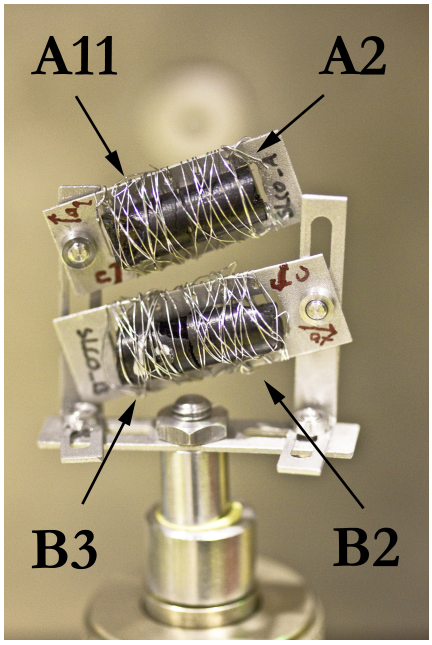

Figure 7.1: Photo of the co-alignment of the four pieces of single crystal used in the experiment at ILL. The direction of the c-axis and the tetragonal a-axis is labelled on each of the two parts of the aluminium sample holder.

The four co-aligned crystals in the sample holder can be seen in Figure 7.1. The four crystal pieces were mounted two and two on an aluminium holder attached to two aluminium plates fastened by aluminium. Al was used as this is a very poor absorber and scatterer of neutrons and will therefore appear transparent. The glued parts of the sample holder were for the second experiment painted with the strong neutron absorber gadolinium oxide in order to reduce background. Each crystal was first aligned using the c-axis and the four crystal pieces were then co-aligned using the tetragonal a-axis. The orthorhombic a-axis was later found at an angle 45° to the tetragonal a-axis. The co-alignment was performed at the neutron Laue diffractometer OrientExpress at ILL. Laue pictures along the tetragonal a-axis are shown in Figure 7.2.

The sample was held in an orange cryostat, 72ILH49, during the experiment. The sample was cooled from room temperature to 2 K at a rate of 1 K/min to allow the excess oxygen in the sample to order. Previous observations [28] showed that the superstructure and the magnetic signal of a LCO+O sample in stage four or six will change upon quenching from higher temperatures. There seems to be some uncertainty about how low temperatures the excess oxygen will continue to be mobile at; Lee et al. [28] estimated 210 K, 200 K was suggested by Wells et al. [57], but recent studies on LSCO+O [14] indicate that disorder caused by the mobility of oxygen can take place all the way down to 120 K. For safety, cooling on oxygen doped samples should be done at a rate of 1 K/min down to at least 100 K. Cooling of the sample during the two experiments was performed several times and was throughout both experiments kept at a rate of 1 K/min.

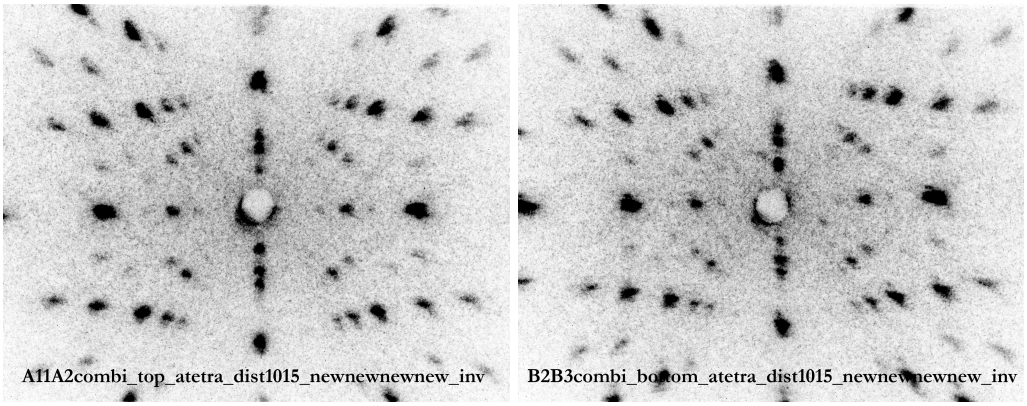

Figure 7.2: Laue pictures along the tetragonal a-axis for the A11 and A2 crystal pieces (left) and the B2 and B3 crystal pieces (right) as labelled in Figure 7.1.

7.3 Energy scans

The energy resolution of the instrument was investigated by performing energy scans over a Bragg peak of the sample and an incoherent signal in order to obtain the Bragg energy resolution and incoherent energy resolution, respectively. In Figure 7.3 (left), the Bragg resolution was found by measuring over the Bragg peak at (200) in reciprocal space for $k_f = 1.5$ Å^{-1} and the full width half maximum (FWHM) of the Gaussian fit to the data was found to be 0.1887±0.0005 meV. This value is slightly higher than the value of the instrument resolution given by the instrument responsible, which was 0.175 meV for $k_f = 1.5$ Å^{-1}.

The energy resolution was determined by performing an energy scan of the sample at a point in reciprocal space (0.7 0.2 0) for $k_f = 1.2$ Å^{-1} (Fig. 7.3, right), away from any ordering position. The FWHM of a Gaussian fit to the incoherent scattering of the sample was found to be 0.077 ± 0.002 meV, which is close to the given value of 0.074 meV at this value of k_f.

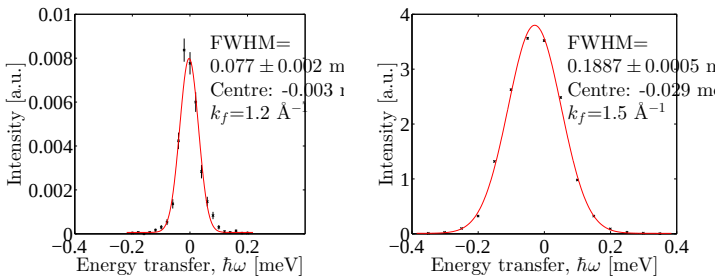

Figure 7.3: Energy resolutions from the first experiment fitted to Gaussian distributions. Left: Energy resolution for $k_f = 1.2$ Å^{-1} measured at (0.7 0.2 0). Right: Bragg energy resolution for $k_f = 1.5$ Å^{-1} measured at (200).

In the second part of the experiment, the energy resolution was measured again at (0.7 0.2 0) for k_f values of 1.1 Å^{-1}, 1.2 Å^{-1} and 1.5 Å^{-1}, i.e. only an incoherent signal was measured. Gaussian fits to the data can be seen in Figure 7.4 along with the FWHM and the position of the centre of the peak.

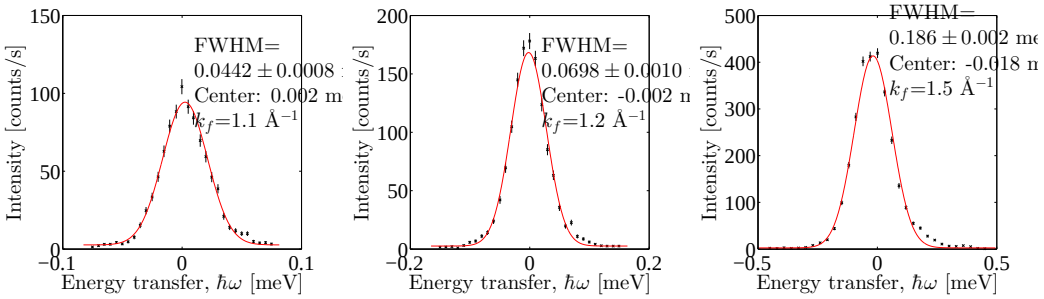

Figure 7.4: Energy resolutions from the second experiment measured at (0.7 0.2 0) fitted to Gaussian distributions. Left: Energy resolution for $k_f = 1.1$ Å^{-1}. Middle: Energy resolution for $k_f = 1.2$ Å^{-1}. Right: Energy resolution for $k_f = 1.5$ Å^{-1}.

A grid scan over the (200) Bragg peak in the second experiment clearly shows sign of twinning or misalignment of the sample pieces (Fig. 7.5).

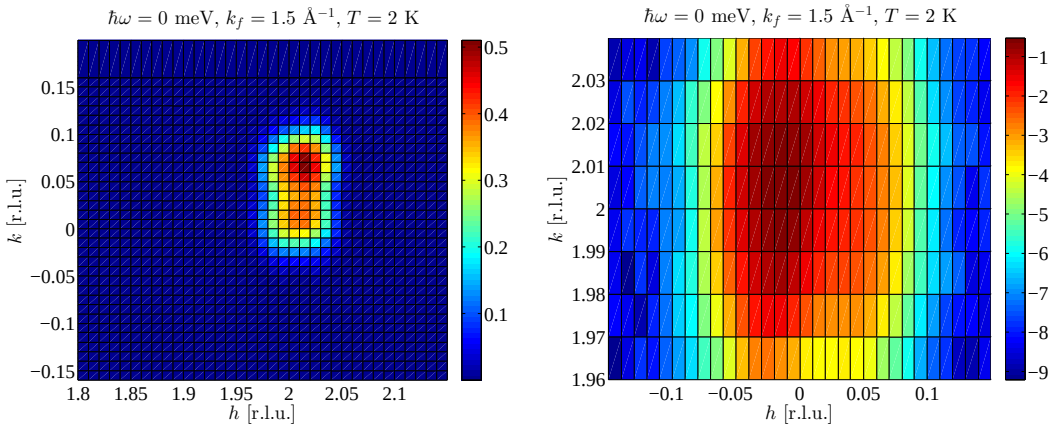

Figure 7.5: Left: Grid scan over the (200) Bragg peak at $k_f = 1.5$ Å^{-1}, shows sign of twinning. Right: As much of a grid scan over the (020) Bragg peak at $k_f = 1.5$ Å^{-1}, as time allowed to do.

One way of estimating the energy resolution is the FWHM of a Bragg peak close to where the scanning will take place. This is only an approximation since the resolution is a function of the scattering vector, and therefore only true if measuring is performed close to the actual Bragg peak. It is possible to calculate the exact instrument resolution in the program ResLib [60] using information on the different components in the experimental setup and sample mosaicity for a particular position in reciprocal space and energy transfer. Unfortunately, this was not possible to do for the collected data from these two experiments with the time given.

7.4 Elastic scan of IC peak

An elastic grid scan was performed over the IC peak during the second experiment at $(1-\delta, -\delta, 0)$ with $\delta = \frac{1}{8}$. An elastic signal at the IC AFM peak position $\delta = \frac{1}{8}$ is a clear sign of

the IC AFM order suggested by the stripe model (Fig. 3.5).

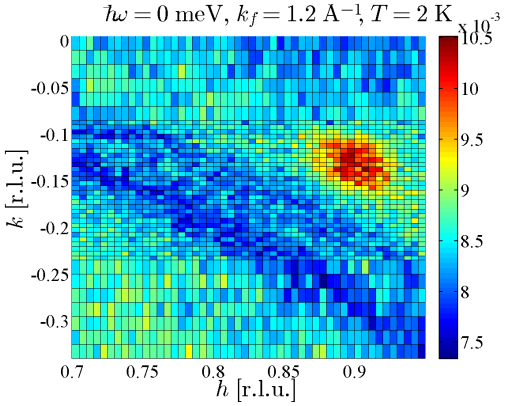

Figure 7.6: The IC magnetic structure signal for $k_f = 1.2$ Å^{-1} at 2 K.

If charged stripes were observed for LSCO with elastic neutron scattering, the signal would appear at $\varepsilon = 2\delta$, i.e. at (0.75 -0.25 0). For low values of q, there was an increase in scattering events – it is not known where this signal comes from.

7.5 Inelastic scans of IC peaks

The bulk part of both experiments was the inelastic scans of the incommensurate peaks. The inelastic scans were performed along k over the IC peaks $(0.875, k, 0)$ for the first and second experiment, referred to as 'exp no. 1' and 'exp no. 2', respectively, in the scans presented in Figure 7.7 and 7.8. During the second experiment, several scans were also performed in k over the IC peaks around $(1.125, k, 0)$, these are referred to as 'exp no. 3'. The scans were performed at $k_f = 1.1, 1.2, 1.5$ Å^{-1} and energy transfer in the range $\hbar\omega$ =0.3-10 meV at 2 K and 45 K.

As previously mentioned, a Be-filter was not used in the first experiment. This resulted in some very strange signals around some of the IC peaks. Examples of data with spurious signals are given in Figure 7.7. A filter was used in the second experiment, and the strange signals disappeared as can be seen in the lower right plot in Figure 7.8. A Gaussian have been fitted to the spurious signals in the data from the first experiment and then included in the Sato-Maki fits (Sec. 7.5.1) to the data.

Examples of raw data are given in Figure 7.8 for different values of k_f, T, and $\hbar\omega$. The intensity of the measured data was normalized to the monitor count in order to later be able to compare data. The efficiency of the monitor is proportional to $1/k_i$ [48]. By counting at constant monitor and keeping k_f fixed, the fraction k_f/k_i is constant. The conversion from measured intensity to $S(\mathbf{q}, \omega)$ is given by:

$$\frac{d\sigma}{d\Omega dE_f} \propto \frac{k_f}{k_i} S(\mathbf{q}, \omega), \tag{7.1}$$

and it is therefore necessary to normalize the data for different values of k_f. The intensity measured for the three different values of k_f was normalized at $h\omega = 1.5$ meV and $T = 2$ K. Two examples used for normalizing intensities for different k_f are given in the two upper plots in Figure 7.8.

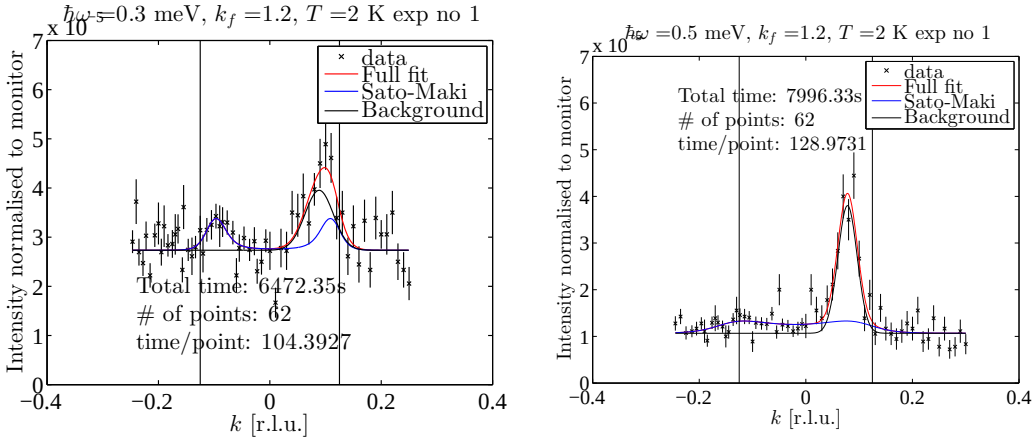

Figure 7.7: Two examples of spurious signals near $k = 0.08$ r.l.u. for $k_f = 1.2$ Å^{-1} at 2 K. Left: for $\hbar\omega = 0.3$ meV. Notice the large background. Right: for $\hbar\omega = 0.5$ meV. Vertical lines are shown at $k = \pm 0.125$ r.l.u.

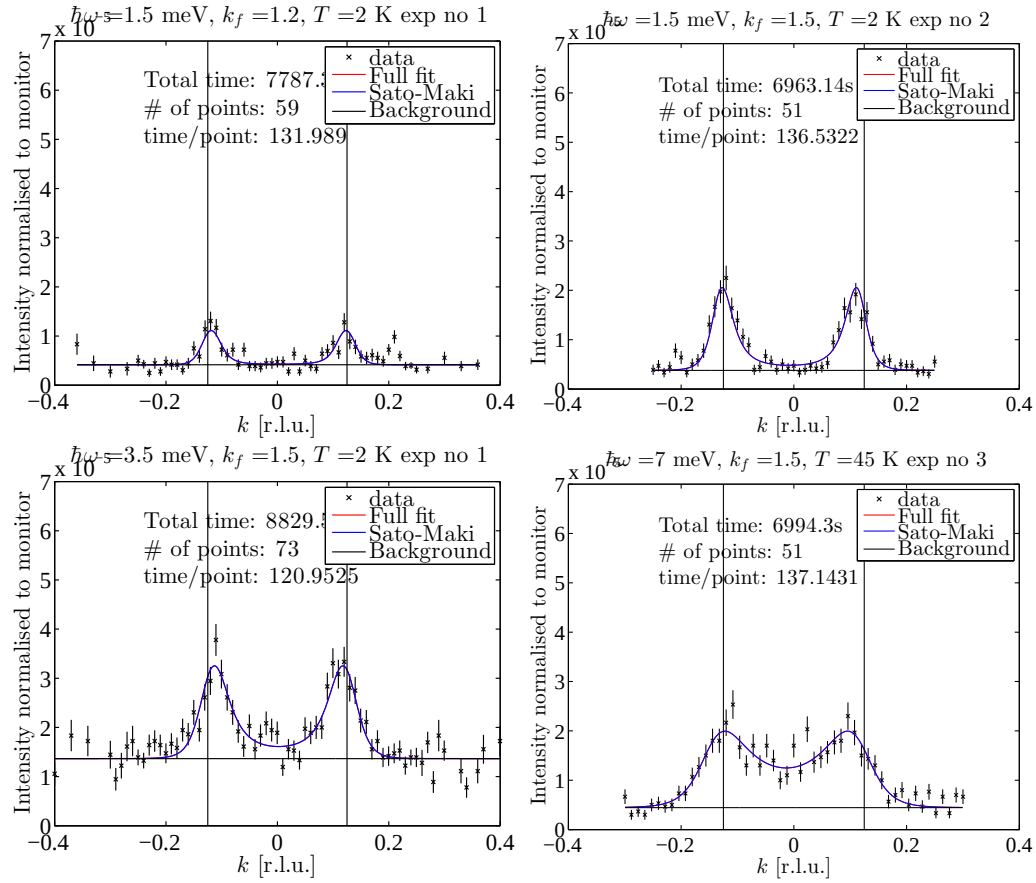

Figure 7.8: Examples of raw data fitted with the Sato-Maki function for different values of the outgoing wavevector, k_f, temperature, T, and energy transfer, $\hbar\omega$. Vertical lines are shown at $k = \pm 0.125$ r.l.u.

Parameter	
p(1)	$[n(\omega)+1]\chi_P^{''}(\omega,T)$
p(2)	$\kappa(\omega,T)$
p(3)	Flat background
p(4)	δ
p(5)	Peak offset
p(6-8)	Gaussian amplitude, width and position for spurious signals
p(9)	Gaussian resolution, σ

Table 7.2: Parameters used for fitting data from inelastic scattering using Spec1d and the Sato-Maki function.

7.5.1 Sato-Maki fits

In some of the previous studies of spin gap in LSCO for $x = 0.163$ by Lake et al. [24] and $x = 0.14$ by Aeppli et al. [1], the data from IC peak scans were fitted using the Sato-Maki function. The function was originally introduced by H. Sato and K. Maki in 1974 [43] as a way of fitting incommensurate magnetic signals. The function itself is out of the scope of this thesis, and instead the procedure outlined in [1] is followed. In Aeppli et al. [1], the data is fitted to the convolution of the instrumental resolution and the expression:

$$S(\mathbf{Q},\omega) = \frac{[n(\omega,T)+1]\chi_P^{''}(\omega,T)\kappa^4(\omega,T)}{[\kappa^2(\omega,T)+R(\mathbf{Q})]^2}, \tag{7.2}$$

where $n(\omega,T)$ is the Bose factor and $[n(\omega,T)+1] = (1-e^{\hbar\omega/k_BT})^{-1}$, which is a measure of the probability of an inelastic scattering event taking place at a certain temperature. κ is a measure of the width of the peaks and $\chi_P^{''}$ is the peak susceptibility. $R(\mathbf{Q})$ is a function with the symmetry of the reciprocal lattice, which has dimensions $|\mathbf{Q}|^2$ and describes the magnetic incommensurate excitations. In tetragonal notation, the function is given by [1]:

$$R(\mathbf{Q}) = \frac{[(q_x-q_y)^2-(\pi\delta)^2]^2+[(q_x+q_y)^2-(\pi\delta)^2]^2}{2(2a_0\pi\delta)^2}. \tag{7.3}$$

At the peak position, $R = 0$, Equation 7.2 reduces to the equation:

$$S(\mathbf{q},\omega) = [n(\omega)+1]\chi_P^{''}(\omega,T). \tag{7.4}$$

The fitting was done in the program Spec1d [30] in MatLab, where the Sato-Maki function was implemented with $R(\mathbf{Q})$ converted into orthorhombic notation. The fits to experimental data are then done using the parameters in Table 7.2.

The position, δ, of the Sato-Maki fits to the experimental data are presented in Figure 7.9. The peaks are positioned close to $\delta = \frac{1}{8}$ with a few exceptions, e.g. the peak at $\hbar\omega = 0.5$ meV, 2 K, and at $k_f = 1.2$ Å^{-1}, which is also shown in Figure 7.7. The amplitudes of the Sato-Maki fits are used for studying a potential spin gap for LCO+O and for comparison with previous data of spin gap in LSCO.

7.5.2 Sato-Maki amplitudes

The Sato-Maki amplitudes are presented in Figure 7.10 and in Figure 7.11. In the latter, only the Sato-Maki amplitudes with the smallest error bars are shown.

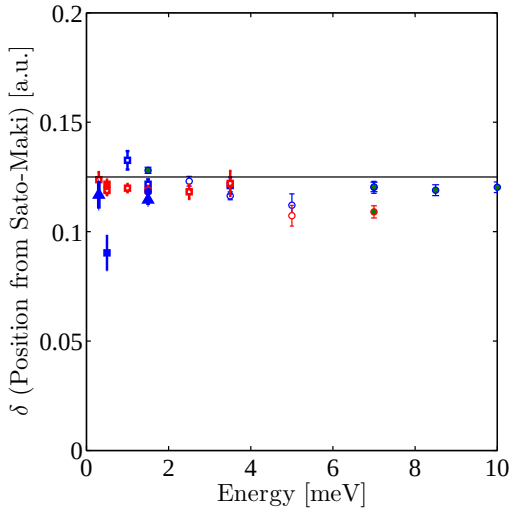

Figure 7.9: The position of the Sato-Maki fits some of which are shown in Figure 7.8. Triangles: $k_f = 1.1$ Å^{-1}. Squares: $k_f = 1.2$ Å^{-1}. Circles: $k_f = 1.5$ Å^{-1}. Blue is 2 K, red is 45 K. Unfilled face: exp no 1. Filled face: exp no 2. Green face: exp no 3. The horizontal line is $\delta = 0.125$.

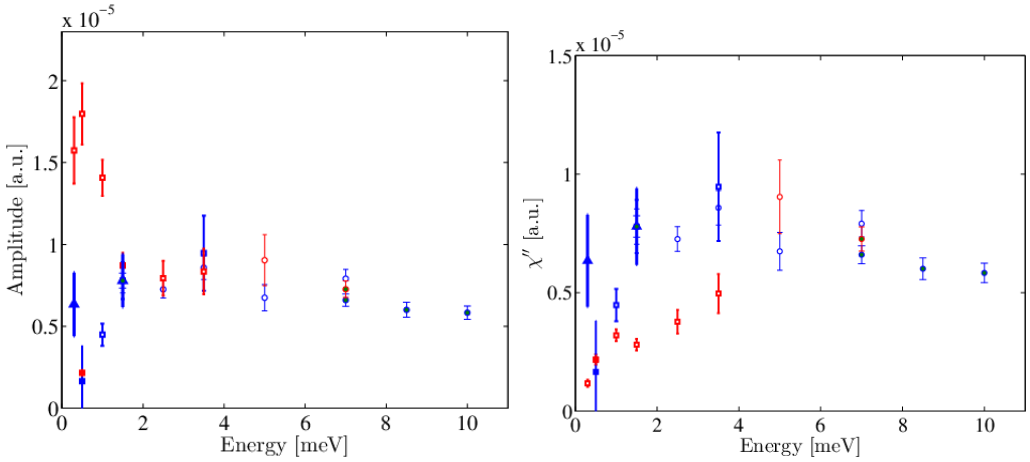

Figure 7.10: The Sato-Maki amplitudes of the fits to experimental data. Left: Not divided by the Bose factor. Right: Divided by the Bose factor to yield χ''. Triangles: $k_f = 1.1$ Å^{-1}. Squares: $k_f = 1.2$ Å^{-1}. Circles: $k_f = 1.5$ Å^{-1}. Red is 45 K, blue is 2 K. Low T data at $k_f = 1.5$ Å^{-1} have been scaled at $\hbar\omega = 1.5$ meV to match low T data at $k_f = 1.2$ Å^{-1}. Unfilled face: exp no 1. Filled face: exp no 2. Green face: exp no 3.

There is a clear difference between the two different temperatures of the Sato-Maki fit amplitudes in Figure 7.11. In the superconducting state at 2 K, there is a much stronger magnetic response for low energies below 5 meV compared with the normal state amplitudes at 45 K. There is a rather large signal at 2 K for 0.3 meV. This and the amplitudes as such will be discussed further in Section 7.7.

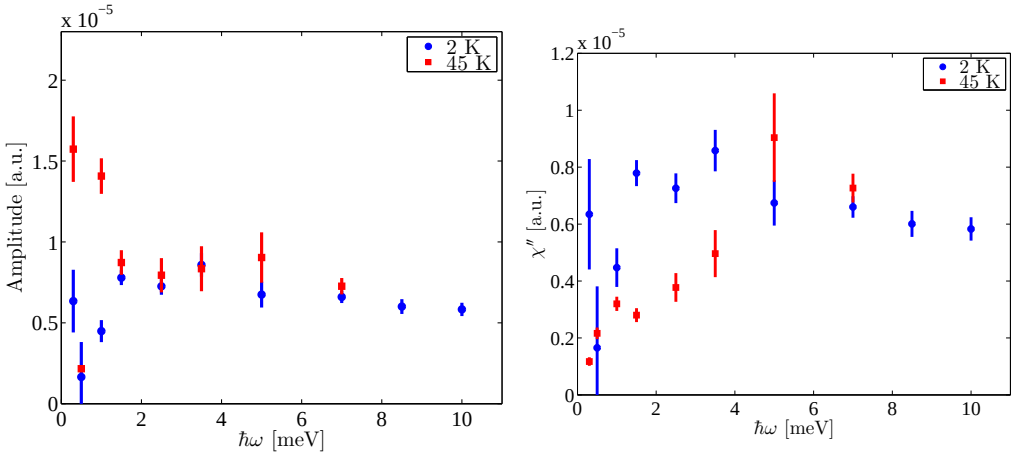

Figure 7.11: Only the Sato-Maki amplitudes from Figure 7.10 with smallest error bars for each energy are shown. Blue: 2 K, red: 45 K.

7.6 Inelastic temperature scans

During the first experiment, three-point scans over the (0.875 −0.125 0) IC AFM signal were performed while cooling the sample. This was done by measuring at the IC AFM position and at a point on either side of the signal as background. The two points away from the IC position were done as a measurement of background. This gives a rough estimate of the peak amplitude.

Three-point scans were done for energy transfer $\hbar\omega = 0.3$ meV and $\hbar\omega = 1.5$ meV for $k_f = 1.2$ Å^{-1}. They are represented in Figure 7.12. As was also illustrated in Figure 7.10 (right), the temperature dependence on the peak amplitude is higher for lower energy transfer than for higher energy transfer.

7.7 Discussion

A static magnetic signal was mapped out around $(1-\delta,-\delta, 0)$ with $\delta = \frac{1}{8}$ by elastic neutron scattering, proving the magnetic stripe order (Fig. 7.6).

Temperature scans were performed while cooling the sample. They give a rough estimate of the change in inelastic response with temperature for two different excitation energies (Fig. 7.12). The change in inelastic response was found to be larger for the low energy excitation below the critical temperature than for higher energy excitations.

The inelastic and magnetic response at different values of energy transfer and temperature from the experiment were presented in Figure 7.11. It seems certain from this study that there is no actual spin gap in the superconducting phase of LCO+O. Of the different

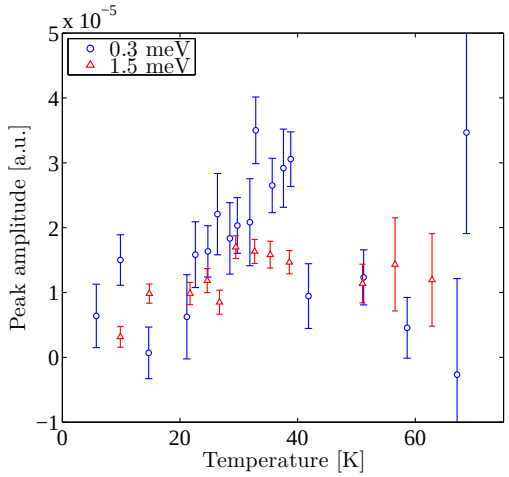

Figure 7.12: Three-point scans upon cooling for $\hbar\omega = 0.3$ meV and $\hbar\omega = 1.5$ meV for $k_f = 1.2$ Å^{-1}. The error bars are given by the standard deviation of the three points.

previous studies outlined in Section 3.5, the measured data seems to be similar to the study by Rømer et al. [42] on a LSCO, $x = 0.12$, sample. Both in the superconducting state and the normal state, the data agree well, except for the data point at $\hbar\omega = 0.3$ meV at 2 K. Rømer et al. did not measure for this low excitation energy. The 0.3 meV signal could be a tail from a magnetic Bragg peak in the IC AFM stripe order, although given the energy resolutions in Figure 7.3 and 7.4 this does not seem likely. It is noticeably that the difference in intensity between the signal at 0.3 meV from the normal phase and the superconducting phase is so large. A suggestion for the origin of the signal is that it is from movement or diffusion of magnetic stripe order throughout the sample. This would result in a Lorentz distribution around zero, but further study is needed in order to establish whether there is a true inelastic signal or if it is a tail from a Bragg peak.

A way of studying the origin of the signal is by μSR which has a time window much longer than that of neutrons. For μSR it can be up to microseconds where for neutron scattering it is in the order of nanoseconds. Such a study takes the same approach as was done for obtaining the data from the magnetic phase diagram in Figure 3.4 by Julien [18], where the static magnetic signal in LSCO, $x = 0.12$, was studied.

The similarities in low energy spin fluctuation between LCO+O studied here, and LCO [37] and LSCO, $x = 0.12$ [42], suggest that there is a dominating magnetic phase, which is not suppressed by superconductivity as observed for optimally doped LSCO. Instead of an actual spin gap in the superconducting phase of LCO+O, there appears to be a partially suppressed anisotropic gap at ~ 1 meV, the same value as for LCO and LSCO, $x = 0.12$.

Further studies should be performed on the LCO+O sample in order to investigate if there is indeed a strong signal for very low excitation energies in the superconducting phase. A way of studying it could be with μSR. The sample should also be studied in field in order to compare with previous studies and in order to hopefully move a step closer to understanding the complex mechanisms responsible for superconductivity in the cuprates.

Chapter 8

Conclusion

This thesis consisted of two experimental parts, crystal growth of $La_{2-x}Sr_xCuO_4$ and the neutron scattering experiment on low energy spin fluctuations in superoxygenated $La_2CuO_{4+\delta}$.

Four crystals in the doping range $x = 0.04 - 0.07$ have been grown and x-ray Laue suggests that they are indeed single crystals. The crystals should be characterized further using neutron scattering to determine that they are indeed single crystals and to determine the quality of the crystals.

These crystals and more to come will be part of further studies with inelastic neutron scattering both in applied field and without applied field. Afterwards they should be superoxygenated to the co-doped compound $La_{2-x}Sr_xCuO_{4+\delta}$ and similar studies should be performed. These studies should investigate low energy spin fluctuations in order to move closer to understanding the complex mechanisms behind high-temperature superconductivity, which seems to be related to magnetic order in the materials.

Low energy spin fluctuations were studied in superoxygenated $La_2CuO_{4+\delta}$ at the neutron scattering instrument IN12 at ILL in May and July 2013. Inelastic neutron scattering experiments were performed on the sample at different temperatures and for different excitation energies. An actual energy gap as that observed for optimally doped $La_{2-x}Sr_xCuO_4$, $x \approx 0.16$, was not found. Instead the spin fluctuations observed in the $La_2CuO_{4+\delta}$ sample seem similar to the anisotropy gap observed in $La_{2-x}Sr_xCuO_4$, $x \approx 0.12$, where there is a strong magnetic phase and in the antiferromagnetic mother compound La_2CuO_4.

Further studies on the superoxygenated sample $La_2CuO_{4+\delta}$ should be performed in order to study the relatively strong signal at very low excitation energies in the superconducting phase and to study the low energy spin fluctuations in an applied field.

Appendix A

Crystal growth

A.1 Powder diffraction

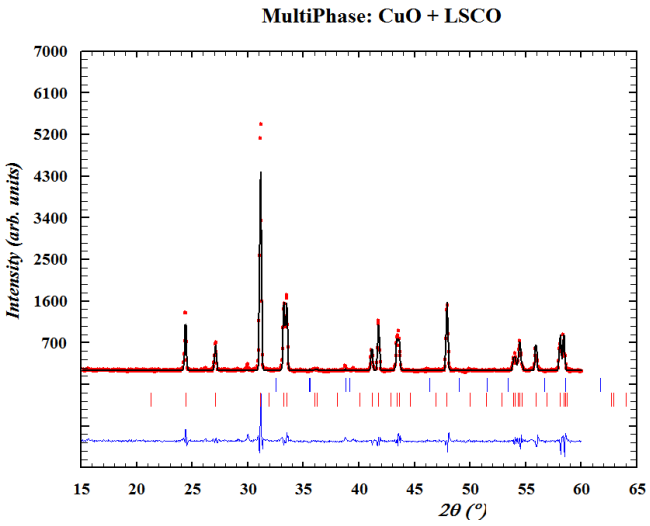

Figure A.1: Rietveld refinement of powder diffraction data from LSCO, $x = 0.03$. Red points are data points, black line is the fit and the blue line below is the difference between fit and data. The bars below the data are structural peaks allowed for the different compounds. Upper blue: CuO (5 mol%) and lower red: LSCO (95 mol%).

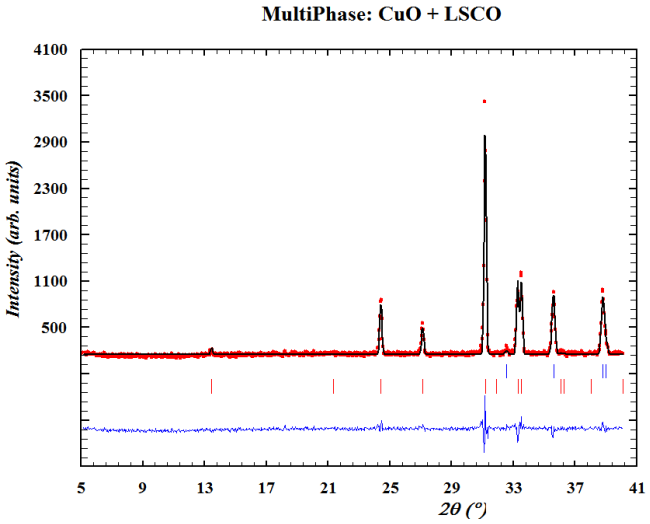

Figure A.2: Rietveld refinement of powder diffraction data from LSCO, $x = 0.04$ solvent. Red points are data points, black line is the fit and the blue line below is the difference between fit and data. The bars below the data are structural peaks allowed for the different compounds. Upper blue: CuO (78 mol%) and lower red: LSCO (22 mol%).

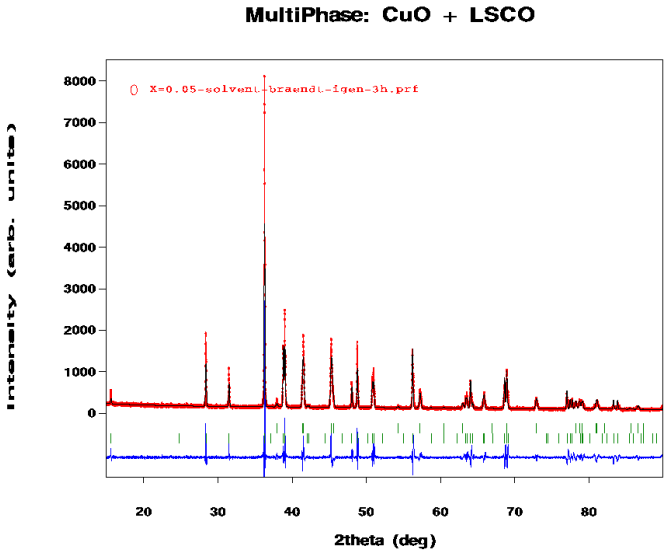

Figure A.3: Rietveld refinement of powder diffraction data from LSCO, $x = 0.05$. Red points are data points, black line is the fit and the blue line below is the difference between fit and data. The bars below the data are structural peaks allowed for the different compounds. Upper blue: CuO and lower red: LSCO.

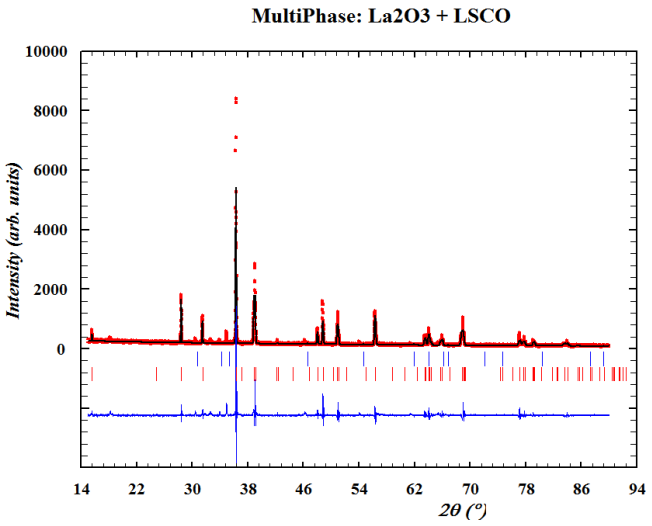

Figure A.4: Rietveld refinement of powder diffraction data from LSCO, $x = 0.06$. Red points are data points, black line is the fit and the blue line below is the difference between fit and data. The bars below the data are structural peaks allowed for the different compounds. Upper blue: La_2O_3 (0.5 mol%)and lower red: LSCO (95.5 mol%).

Figure A.5: Disintegrated $x = 0.02$ LSCO sample. Powder diffraction was performed on the powder (Fig. A.6 and A.7).

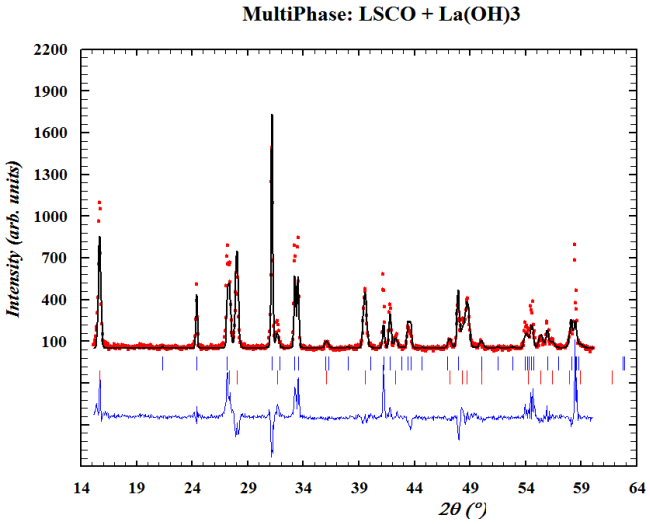

Figure A.6: Rietveld refinement of powder diffraction data from disintegrated LSCO sample, $x = 0.02$, marked '1' in Figure A.5. Red points are data points, black line is the fit and the blue line below is the difference between fit and data. The bars below the data are structural peaks allowed for the different compounds. Upper blue: LSCO (36 mol%)and lower red: $La(OH)_3$ (64 mol%).

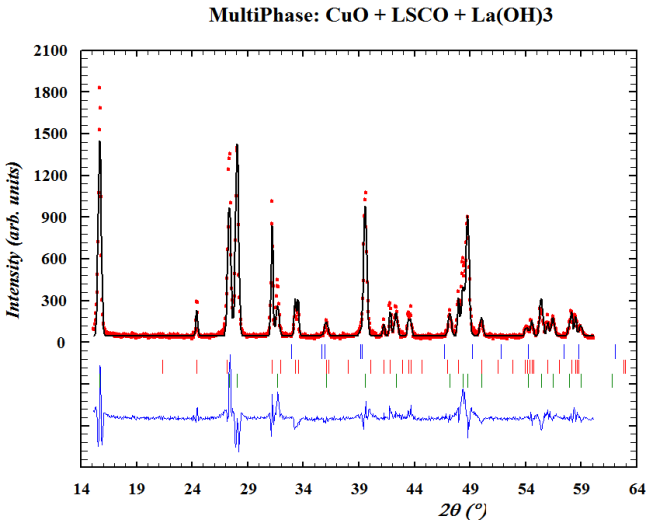

Figure A.7: Rietveld refinement of powder diffraction data from disintegrated LSCO sample, $x = 0.02$, marked '2' in Figure A.5. Red points are data points, black line is the fit and the blue line below is the difference between fit and data. The bars below the data are structural peaks allowed for the different compounds. Upper blue: CuO (7 mol%), middle red: LSCO (12 mol%), and lower green: $La(OH)_3$ (81 mol%).

A.2 Laue

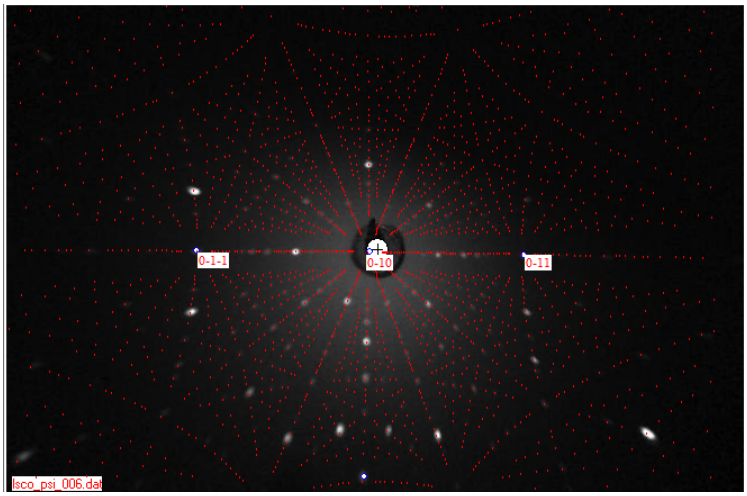

Figure A.8: Laue picture for $x = 0.06$ analyzed using OrientExpress. The c-axis is horizontal in the picture and the b-axis points directly into the Laue camera.

Appendix B

Low energy spin fluctuations in LCO+O

The inelastic scans done over the two (0.875,±0.125,0) peaks for experiment 1 and 2. During experiment 2, scans were also performed over (1.125, ±0.125, 0) referred to as experiment 3. All these scans were done along k. They were done for varying final wavevector, k_f, temperature, T, and energy transfer, $\hbar\omega$.

During the first experiment, at $T = 2$ K, the scans were performed for several energy transfers at both $k_f = 1.2$ Å^{-1} and $k_f = 1.5$ Å^{-1}. The $k_f = 1.2$ Å^{-1} scans are shown in Figure B.1, while the $k_f = 1.5$ Å^{-1} scans are shown in Figure B.3. At T =45 K, the measurements were done with $k_f = 1.2$ Å^{-1}, as shown in Figure B.2, and a single energy energy transfer for $k_f = 1.5$ Å^{-1}, shown in Figure B.4.

In the second experiment, scans were performed with $k_f = 1.1$ Å^{-1} at $T = 2$ K and $T = 45$ K shown in Figure B.5. At $T = 2$ K, more scans were carried out for $k_f = 1.2$ Å^{-1} and $k_f = 1.5$ Å^{-1}, they are presented in Figure B.6, and finally, in Figure B.7, the data from what is referred to as experiment 3 is represented.

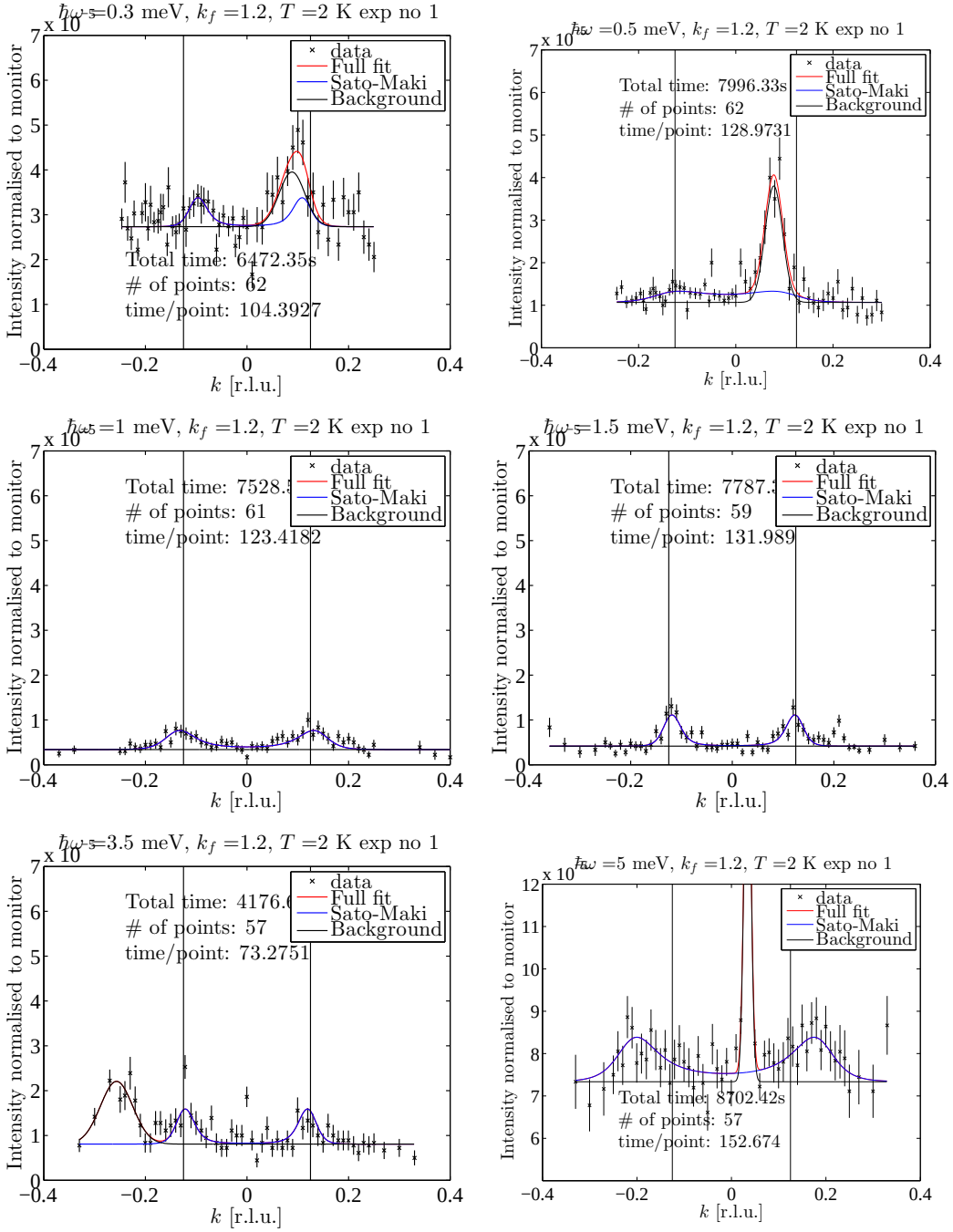

Figure B.1: Scans over the two (0.875,±0.125,0) peaks at $T = 2$ K for $k_f = 1.2$ Å^{-1}, at different energy transfers $\hbar\omega$.

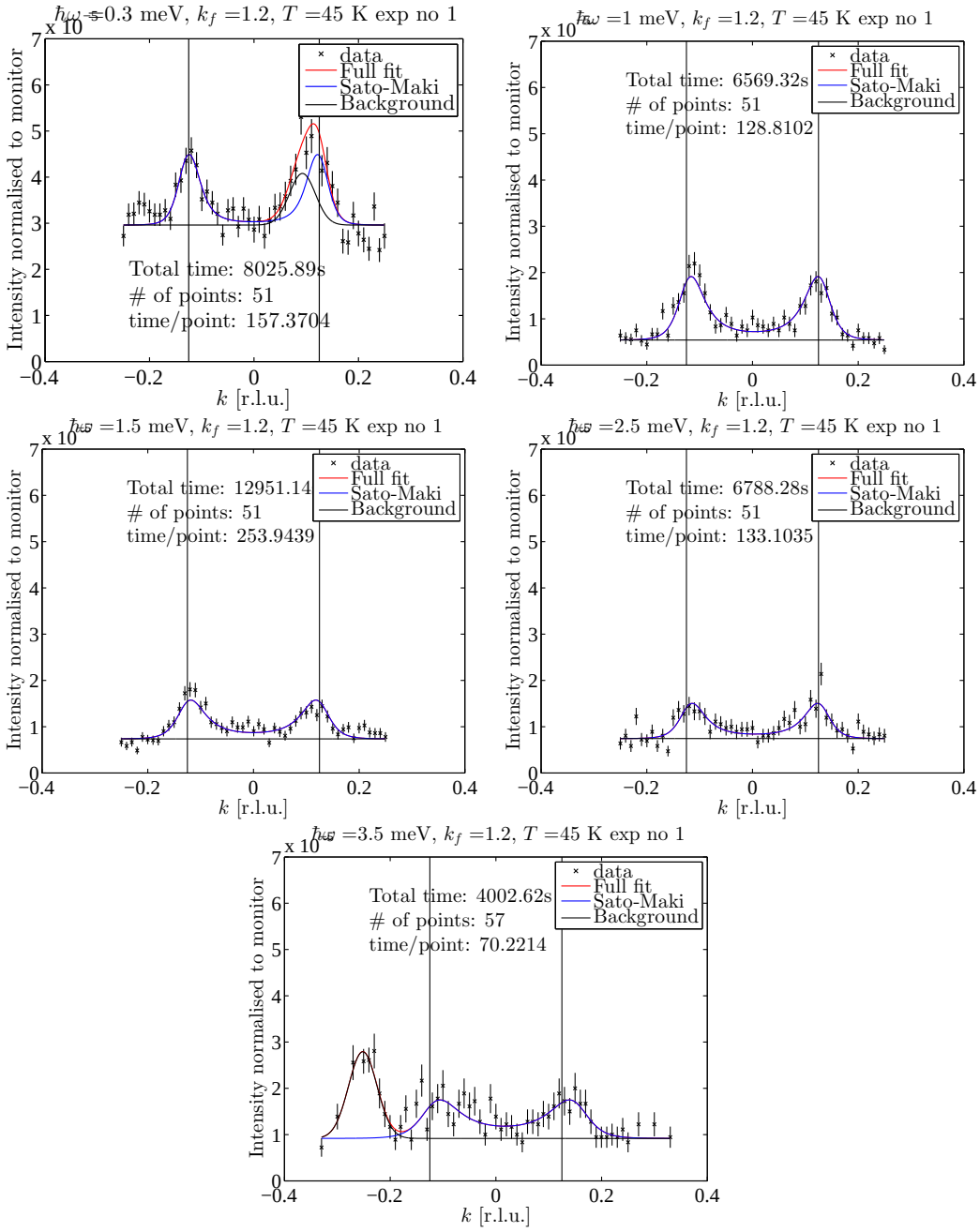

Figure B.2: Scans over the two (0.875,±0.125,0) peaks for $k_f = 1.2$ Å^{-1} at $T = 45$ K.

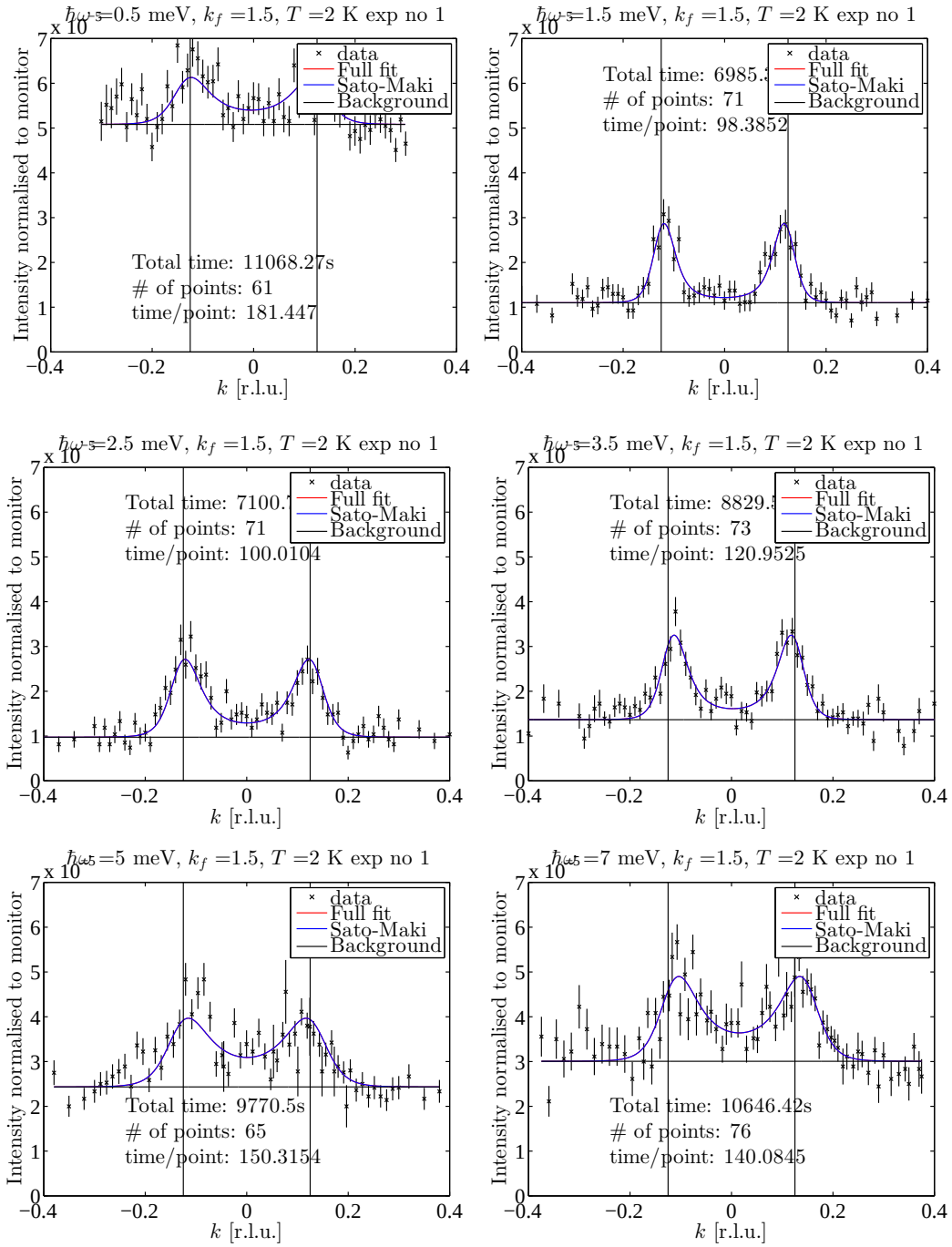

Figure B.3: Scans over the two (0.875,±0.125,0) peaks at T = 2 K for k_f = 1.5 Å^{-1}, at different energy transfers $\hbar\omega$.

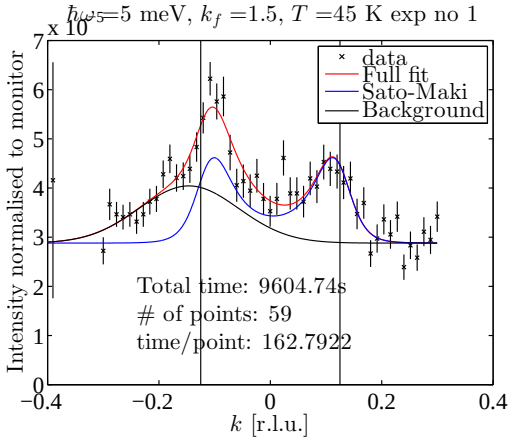

Figure B.4: Scan over the two (0.875,±0.125,0) peaks at $T = 45$ K for $k_f = 1.5$ Å^{-1}, at the only measured energy transfer of $\hbar\omega = 5.0$ meV during the first experiment.

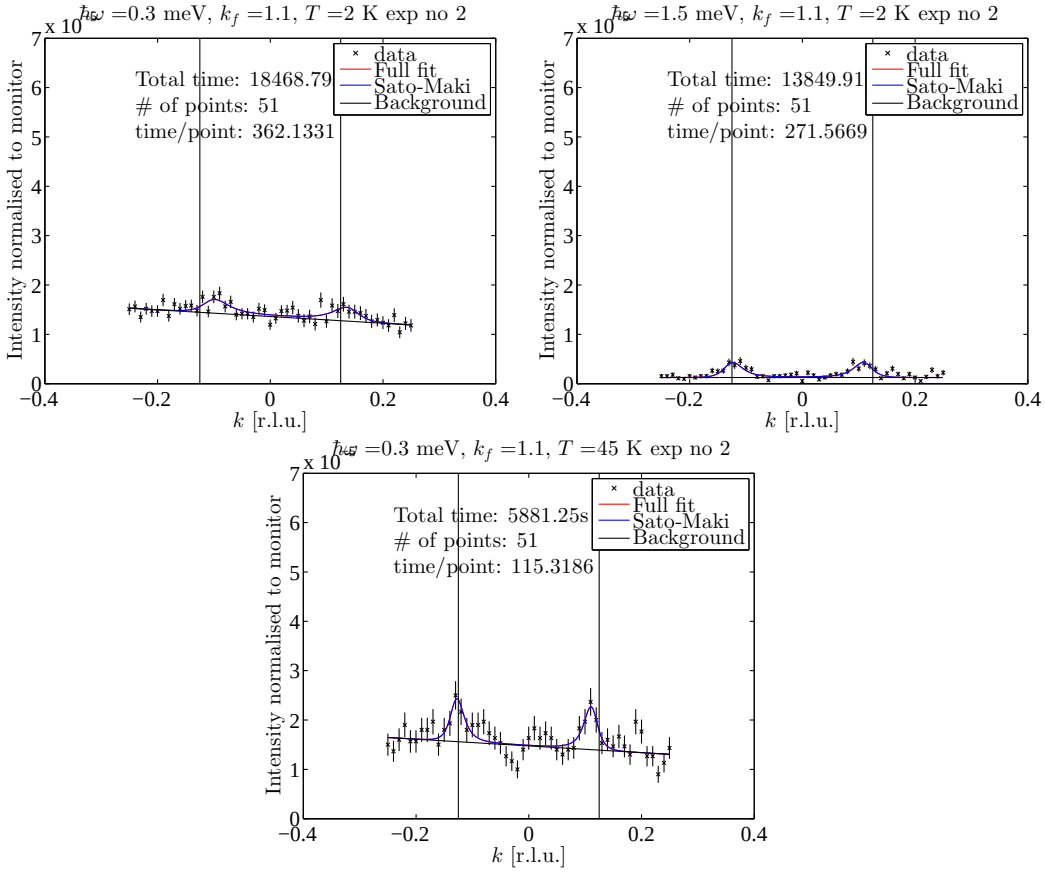

Figure B.5: From the second experiment. Scan over the two (0.875,±0.125,0) peaks for $k_f = 1.1$ Å^{-1}.

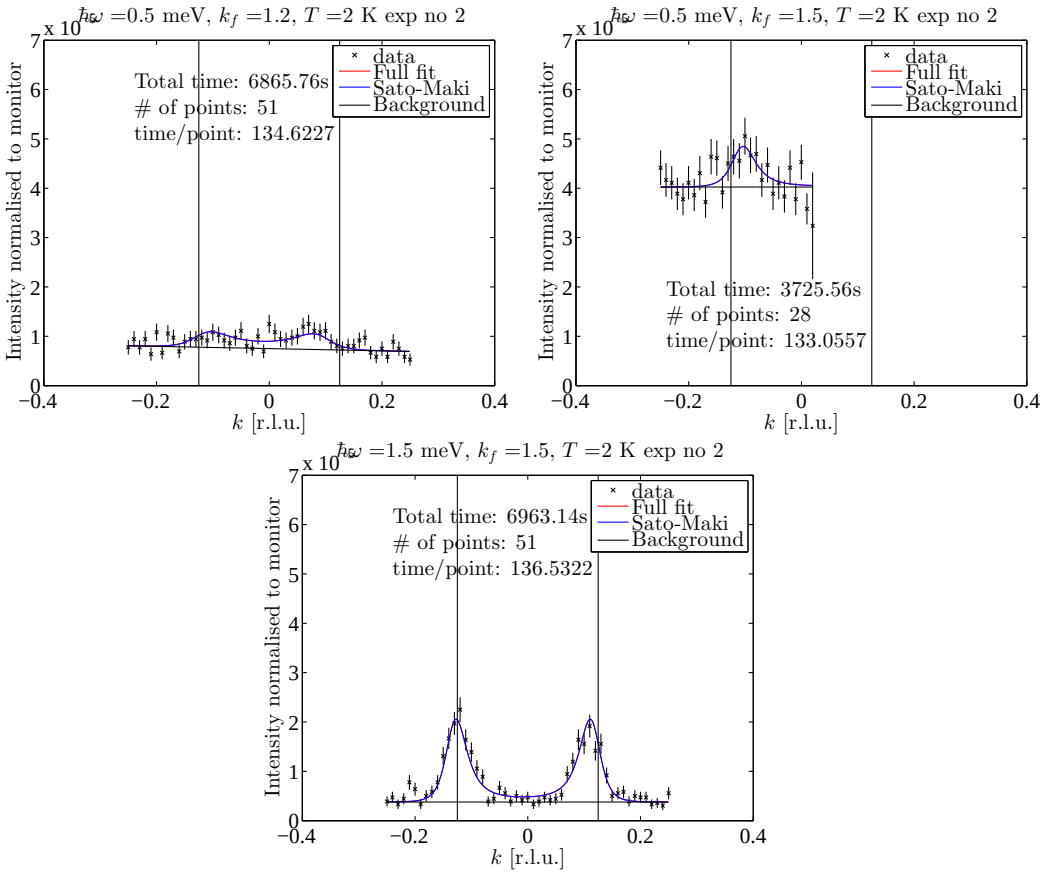

Figure B.6: From the second experiment. Scan over the two (0.875,±0.125,0) peaks.

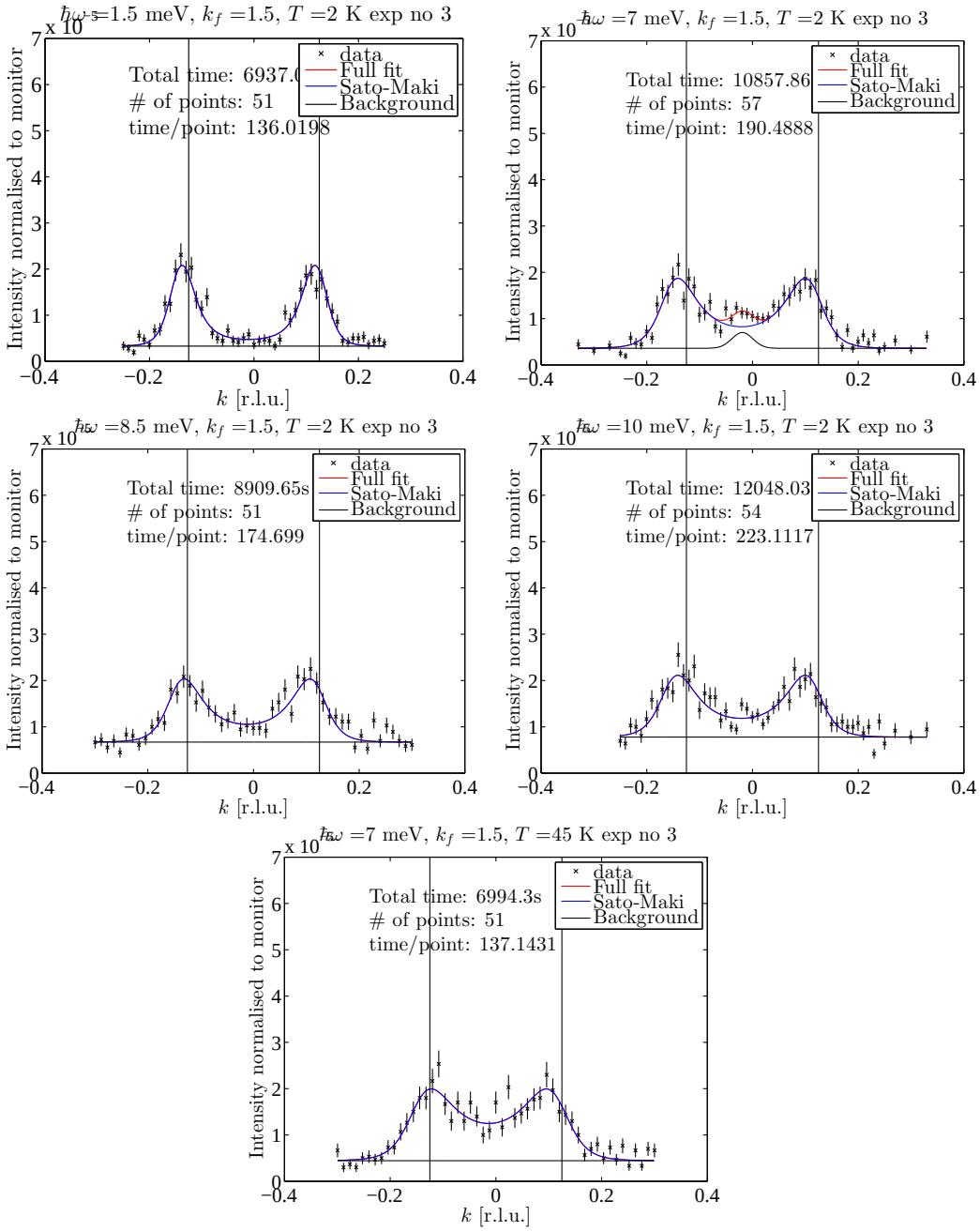

Figure B.7: From the second experiment – referred to as the third experiment: Scan over the two (1.125,±0.125,0) peaks for $k_f = 1.2$ Å^{-1}.

Bibliography

[1] G. Aeppli, T.E. Mason, S.M. Hayden, H.A. Mook, and J. Kulda. Nearly singular magnetic fluctuations in the normal state of a high-T_c cuprate superconductor. *Science*, 278(5342):1432–1435, 1997.

[2] J. Als-Nielsen and D. McMorrow. *Elements of Modern X-ray Physics*. Wiley, 2nd edition, 2011.

[3] E.H. Appelman, L.R. Morss, A.M. Kini, U. Geiser, A. Umezawa, G.W. Crabtree, and K. D. Carlson. Oxygen content of superconducting perovskites, $La_{2-x}Sr_xCuO_y$ and $YBa_2Cu_3O_y$. *Inorganic Chemistry*, 26(20):3237–3239, 1987.

[4] P. Barnes, S. Jacques, and M. Vicker. Powder diffraction. `http://pd.chem.ucl.ac.uk/pdnn/diff2/kinemat2.htm`, Last accessed May 2014.

[5] S. Blundell. *Magnetism in Condensed Matter*. Oxford University Press, 2001.

[6] M. Braden, G. Heger, P. Schweiss, Z. Fisk, K. Gamayunov, I. Tanaka, and H. Kojima. Characterization and structural analysis of twinned $La_{2-x}Sr_xCuO_{4\pm\delta}$ crystals by neutron scattering. *Physica C*, 191:455–468, 1992.

[7] G.W. Brindley. The effect of grain or particle size on x-ray reflections from mixed powders and alloys, considered in relation to the quantitative determination of crystalline substances by x-ray methods. *Philosophical Magazine*, 36(256):347–369, 1945.

[8] M. Buchanan. Mind the pseudogap. *Nature*, 409:8–11, 2001.

[9] J. Chang. *Magnetic and electronic properties of the high-temperature superconductor* $La_{2-x}Sr_xCuO_4$. PhD thesis, Laboratorium für Neutronen-streuung, ETHZ, 2008.

[10] J. Chang, N.B. Christensen, Ch. Niedermayer, K. Lefmann, H.M. Rønnow, D.F. McMorrow, A. Schneidewind, P. Link, A. Hiess, M. Boehm, R. Mottl, S. Pailhés, N. Momono, M. Oda, M. Ido, and J. Mesot. Magnetic-field induced soft-mode quantum phase transition in the high-temperature superconductor $La_{1.855}Sr_{0.145}CuO_4$: An inelastic neutron-scattering study. *Physical Review Letters*, 102:177006.

[11] F.C. Chou, D.C. Johnston, S-W. Cheong, and P.C. Canfield. Preparation, magnetization and electrical resistivity of electrochemically oxidized $La_2CuO_{4+\delta}$ single crystals. *Physica C: Superconductivity*, 216:66–76, 1993.

[12] N. B. Christensen, J. Chang, J. Larsen, M. Fujita, M. Oda, M. Ido, N. Momono, E. M. Forgan, A. T. Holmes, J. Mesot, M. Huecker, and M.v. Zimmermann. Bulk charge stripe order competing with superconductivity in $La_{2-x}Sr_xCuO_4$ ($x = 0.12$). Submitted to Physical Review Letters, 11 April 2014.

[13] Max-Planck-Institut Crystal Growth Group. Traveling solvent floating zone growth technique. `http://www2.fkf.mpg.de/crystal/d1-tsfz.pdf`, Last accessed May 2014.

[14] Udby et al. Work in preparation, 2014.

[15] M. Fujita, K. Yamada, H. Hiraka, P. M. Gehring, S. H. Lee, S. Wakimoto, and G. Shirane. Static magnetic correlations near the insulating-superconducting phase boundary in $La_{2-x}Sr_xCuO_4$. *Physical Review B*, 65:064505, 2002.

[16] J.-C. Grenier, N. Lagueyte, A. Wattiaux, J-P. Doumerc, P. Dordor, J. Etourneau, M. Pouchard, J.B. Goodenough, and J.S. Zhou. Transport and magnetic properties of the superconducting $La_2CuO_{4+\delta}$ phases ($0 < \delta < 0.09$) prepared by electrochemical oxidation. *Physica C: Superconductivity*, 202:209–218, 1992.

[17] ILL. CRG - cold neutron three-axis spectrometer. `http://www.ill.eu/instruments-support/instruments-groups/instruments/in12/`, Last accessed May 2014 May 2013.

[18] M.-H. Julien. Magnetic order and superconductivity in $La_{2-x}Sr_xCuO_4$: a review. *Physica B: Physics of Condensed Matter*, 329:693–696, 2003.

[19] FIZ Karlsruhe. Inorganic Crystal Structure Database. `https://www.fiz-karlsruhe.de/icsd_home.html`, Last accessed May 2014.

[20] S. Kimura and I. Shindo. Single crystal growth of YIG by the floating zone method. *Journal of Crystal Growth*, 41:192–198, 1977.

[21] C. Kittel. *Introduction to Solid State Physics*. Wiley, 8th edition, 2005.

[22] M. Kofu, S.-H. Lee, M. Fujita, H.-J. Kang, H. Eisaki, and K. Yamada. Hidden quantum spin-gap state in the static stripe phase of high-temperature $La_{2-x}Sr_xCuO_4$. *Physical Review Letters*, 102:047001, 2009.

[23] H. Kojima, J. Yamamoto, Y. Mori, M.K.R. Khan, H. Tanabe, and I. Tanaka. Single crystal growth of superconducting $La_{2-x}M_xCuO_4$ (M = Ca, Sr, Ba) by the TSFZ method. *Physica C: Superconductivity and its Applications*, 293:14–19, 1997.

[24] B. Lake, G. Aeppli, K.N. Clausen, D.F. McMorrow, K. Lefmann, N.E. Hussey, N. Mangkorntong, M. Nohara, H. Takagi, T.E. Mason, and A. Schröder. Spins in the vortices of a high-temperature superconductor. *Science*, 291(5509):1759–1762, 2001.

[25] B. Lake, K. Lefmann, N.B. Christensen, G. Aeppli, D.F. McMorrow, H.M. Rønnow, P. Vorderwisch, P. Smeibidl, N. Mangkorntong, T. Sasagawa, M. Nohara, and H. Takagi. Three-dimensionality of field-induced magnetism in a high-temperature superconductor. *Nature Materials*, 4:658–662, 2005.

[26] B. Lake, H.M. Rønnow, N.B. Christensen, G. Aeppli, K. Lefmann, D.F. McMorrow, P. Vorderwisch, P. Smeibidl, N. Mangkorntong, T. Sasagawa, M. Nohara, H. Takagi, and T.E. Mason. Antiferromagnetic order induced by an applied magnetic field in a high-temperature superconductor. *Nature*, 415:299–302, 2002.

[27] J. Laugier and B. Bochu. Orientexpress v3.4.

[28] Y.S. Lee, F.C. Chou, A. Tewary, M.A. Kastner, S.H. Lee, and R.J. Birgenau. Neutron scattering study of the effects of dopant disorder on the superconductivity and magnetic order in stage-4 La_2CuO_{4+y}. *Physical Review B*, 69:020502.

[29] K. Lefmann. Neutron Scattering: Theory, Instrumentation, and Simulation. Lecture notes from the course Neutron Scattering at the University of Copenhagen, autumn 2013.

[30] D. McMorrow and H. Rønnow. Spec1d - version 2.0. `http://www.ill.eu/html/instruments-support/computing-for-science/cs-software/all-software/matlab-ill/spec1d/`, 2001. Last accessed May 2014.

[31] H.E. Mohottala, B.O. Wells, J.I. Budnick, W.A. Hines, C. Niedermayer, L. Udby, C. Bernhard, A. Moodenbaugh, and F.-C. Chou. Phase separation in superoxygenated $La_{2-x}Sr_xCuO_{4+y}$. *Nature Materials*, 5:377–382, 2006.

[32] K. A. Müller and J. G. Bednorz. Perovskite-type oxides – the new approach to high-T_c superconductivity. `http://www.nobelprize.org/nobel_prizes/physics/laureates/1987/bednorz-muller-lecture.pdf`, December 1987, Last accessed May 2014.

[33] Ltd. MultiWire Laboratories. `http://multiwire.com/index.shtml`, Last accessed May 2014.

[34] M. Napoletano, J.M. Gallardo Amores, E. Magnone, G. Busca, and M. Ferretti. Skeletal infrared spectra and structural properties of $La_{2-x}Sr_xCuO_4$ and $La_{2-x}Ba_xCuO_4$ cuprate powders in the $0 \leq x \leq 0.125$ region. *Physica C: Superconductivity and its Applications*, 319:229–237, 1999.

[35] K. Oka and H. Unoki. Phase diagram of the La_2O_3-CuO and crystal growth of $(LaBa)_2CuO_4$. *Japanese Journal of Applied Physics*, 26(10):1590–1592, 1987.

[36] H. K. Onnes. Investigations into the properties of substances at low temperatures, which have led, amongst other things, to the preparation of liquid helium. `http://www.nobelprize.org/nobel_prizes/physics/laureates/1913/onnes-lecture.pdf`, December 1913, Last accessed May 2014.

[37] C. J. Peters, R. J. Birgeneau, M.A. Kastner, H. Yoshizawa, Y. Endoh, J. Tranquada, G. Shirane, Y. Hidaka, M. Oda, M. Suzuki, and T. Murakami. Two-dimensional zone-center spin-wave excitations in La_2CuO_4. *Physical Review B*, 37(16):9761–9764, 1988.

[38] P. Philips. Review: Mottness collapse and t-linear resistivity in cuprate superconductors. *Philosophical Transactions of the Royal Society: A*, 369:1574–1598, 2011.

[39] P.G. Radaelli, J.D. Jorgensen, A.J. Schultz, B.A. Hunter, J.L. Wagner, F.C. Chou, and D.C. Johnston. Structure of the superconducting $La_2CuO_{4+\delta}$ phases ($\delta \approx 0.08, 0.12$) prepared by electrochemical oxidation. *Physical Review B*, 48(1):499–510, 1993.

[40] M. Reehuis, C. Ulrich, K. Prokes, A. Gozar, G. Blumberg, S. Komiya, Y. Ando, P. Pattison, and B. Keimer. Crystal structure and high-field magnetism of La_2CuO_4. *Physical Review B*, 73:144513, 2006.

[41] J. Rodríguez-Carvajal. An introduction to the program FullProf 2000. Laboratoire Léon Brillouin, CEA-CNRS, July 2001.

[42] A.T. Rømer, J. Chang, N.B. Christensen, B.M. Andersen, K. Lefmann, L. Mähler, J. Gaviliano, R. Gilardi, Ch. Niedermayer, H.M. Rønnow, A. Schneidewind, P. Link, M. Oda, M. Ido, N. Momono, and J. Mesot. Glassy low-energy spin fluctuations and anisotropy in $La_{1.88}Sr_{0.12}CuO_4$. *Physical Review B*, 87(14):144513, 2013.

[43] H. Sato and K. Maki. Theory of inelastic neutron scattering from Cr and its alloys near the Néel tempereature. *International Journal of Magnetism*, 6:183–209, 1974.

[44] A. Schilling, M. Cantoni, J.D. Guo, and H.R. Ott. Superconductivity above 130 K in the Hg-Ba-Ca-Cu-O system. *Nature*, 363:56–58, 1993.

[45] J.E. Schirber, B. Morosin, R.M. Merril, P.F. Hlava, E.L. Venturini, J.F. Kwak, P.J. Nigrey, R.J. Baughman, and D.S. Ginley. Stoichiometry of bulk superconducting $La_2Sr_xCuO_{4+y}$: A superconducting superoxide? *Physica C*, 152:121–123, 1988.

[46] K. Sekizawa, Y. Takano, H. Takigami, S. Tasaki, and T. Inaba. Superconductivity in the La-Cu-O system. *Japanese Journal of Applied Physics*, 26(5):L840–L841, 1987.

[47] X.-L. Shen, Z.-C. Li, C.-X. Shen, W. Lu, X.-L. Dong, F. Zhou, and Z.-X. Zhao. Floating-zone growth and property characterizations of high-quality $La_{2-x}Sr_xCuO_4$ superconductor crystals. *Chinese Physics B*, 18:2893–2896, 2009.

[48] G. Shirane, S.M. Shapiro, and J.M. Tranquada. *Neutron Scattering with a Triple-Axis Spectrometer – Basic Techniques*. Cambridge University Press, 2002.

[49] J. Sólyom. *Fundementals of the Physics of Solids*, volume II, chapter 26, pages 449–515. Springer, 2009.

[50] J. Sólyom. *Fundementals of the Physics of Solids*, volume III, chapter 34, pages 393–471. Springer, 2010.

[51] M. Suzuki and M. Hikita. Resistive transition, magnetoresistance, and anisotropy in $La_{2-x}Sr_xCuO_4$ single-crystal thin films. *Physical Review B*, 48:249–261, 1991.

[52] I. Tanaka, K. Yamane, and H. Kojima. Single crystal growth of superconducting $La_{2-x}Sr_xCuO_4$ by the TSFZ method. *Journal of Crystal Growth*, 96:711–715, 1989.

[53] P. Thompson, D.E. Cox, and J.B. Hastings. Rietveld refinement of Debye-Scherrer synchrotron x-ray data from Al_2O_3. *Journal of Applied Crystallography*, 20:79–82, 1987.

[54] J. M. Tranquada, B. J. Sternlieb, J. D. Axe, Y. Nakamura, and S. Uchida. Evidence for stripe correlations of spins and holes in copper oxide superconductors. *Nature*, 375:561–563, 1995.

[55] L. Udby, J. Larsen, N.B. Christensen, M. Boehm, Ch. Niedermayer, H.E. Mohottala, T.B.S. Jensen, R. Toft-Petersen, F.C. Chou, N.H. Andersen, K. Lefmann, and B.O. Wells. Measurements of unique magnetic and superconducting phases in oxygen-doped high-tempereature superconductors $La_{2-x}Sr_xCuO_{4+y}$. *Physical Review Letters*, 111:227001, 2013.

[56] A. Vickery, L. Udby, N. Violini, J. Voigt, P.P. Deen, and K. Lefmann. A Monte Carlo simulation of neutron instrument resolution funtions. *The Physical Society of Japan*, 82, 2013.

[57] B.O. Wells, Y.S. Lee, M.A. Kastner, R.J. Christianson, R.J. Birgeneau, K. Yamada, Y. Endoh, and G. Shirane. Incommensurate spin fluctuations in high-transition temperature superconductors. *Science*, 277(5329):1067–1071, 1997.

[58] M. K. Wu, J. R. Ashburn, C. J. Torng, P. H. Hor, R. L. Meng, L. Gao, Z. J. Huang, Y. Q. Wang, and C. W. Chu. Superconductivity at 93 K in a new mixed-phase Y-Ba-Cu-O compound system at ambient pressure. *Physical Review Letters*, 58:908–910, 1987.

[59] K. Yamada, C. H. Lee, K. Kurahashi, J. Wada, S. Wakimoto, S. Ueki, H. Kimura, Y. Endoh, S. Hosoya, G. Shirane, R. J. Birgeneau, M. Greven, M. A. Kastner, and Y. J. Kim. Doping dependence of the spatially modulated dynamical spin correlations and the superconducting-transition temperature in $La_{2-x}Sr_xCuO_4$. *Physical Review B*, 57:6165–6172, 1998.

[60] A. Zheludev. ResLib 3.4 - 3-axis resolution library for MatLab. *Neutron Scattering Sciences Division*, 2007.

[61] M.v. Zimmermann, A. Vigliante, T. Niemöller, N. Ichikawa, T. Frello, J. Madsen, P. Wochner, S. Uchida, N. H. Andersen, J. M. Tranquada, D. Gibbs, and J. R. Schneider. Hard–X-ray diffraction study of charge stripe order in $La_{1.48}Nd_{0.4}Sr_{0.12}CuO_4$. *Europhysics Letters*, 41:629–634, 1998.